

Recovery of the internal orbital structure of galaxies

G. van de Ven^{1,2,3*}†, P. T. de Zeeuw^{1,4}, R. C. E. van den Bosch¹

¹*Leiden Observatory, Leiden University, P.O. Box 9513, 2300 RA Leiden, The Netherlands*

²*Department of Astrophysical Sciences, Peyton Hall, Princeton, NJ 08544, USA*

³*Institute for Advanced Study, Einstein Drive, Princeton, NJ 08540, USA*

⁴*European Southern Observatory, D-85748 Garching bei München*

Accepted 0000 Month 00. Received 0000 Month 00; in original 0000 Month 00

ABSTRACT

We construct axisymmetric and triaxial galaxy models with a phase-space distribution function that depends on linear combinations of the three exact integrals of motion for a separable potential. These Abel models, first introduced by Dejonghe & Laurent and subsequently extended by Mathieu & Dejonghe, are the axisymmetric and triaxial generalisations of the well-known spherical Osipkov–Merritt models. We show that the density and higher order velocity moments, as well as the line-of-sight velocity distribution (LOSVD) of these models can be calculated efficiently and that they capture much of the rich internal dynamics of early-type galaxies. We build a triaxial and oblate axisymmetric galaxy model with projected kinematics that mimic the two-dimensional kinematic observations that are obtained with integral-field spectrographs such as SAURON. We fit the simulated observations with axisymmetric and triaxial dynamical models constructed with our numerical implementation of Schwarzschild’s orbit-superposition method. We find that Schwarzschild’s method is able to recover the internal dynamics and three-integral distribution function of realistic models of early-type galaxies.

Key words: stellar dynamics – celestial mechanics – galaxies: elliptical and lenticular, cD – galaxies: kinematics and dynamics – galaxies: structure

1 INTRODUCTION

The equilibrium state of a collisionless stellar system such as an elliptical or lenticular galaxy is completely described by its distribution function (DF) in the six-dimensional phase space of positions and velocities. The recovery of the DF from observations is difficult, as for galaxies other than our own, we can usually only measure the projected surface brightness and the line-of-sight velocity distribution (LOSVD) of the integrated light as a function of position on the plane of the sky. Moreover, we generally do not know the intrinsic shape of the galaxy, nor the viewing direction, or the contribution to the gravitational potential provided by a super massive central black hole and/or an extended halo of dark matter. By Jeans (1915) theorem, the DF is a function of the isolating integrals of motion admitted by the potential, but it is not evident how to take advantage of this property other than for the limiting case of spherical systems. Orbits in axisymmetric geometry have two exact integrals of motion, the energy E and the angular momentum component L_z parallel to the symmetry z -axis, but the third effective or non-classical integral I_3 obeyed by all regular orbits is generally not known in closed form. In stationary triaxial geometry E

is conserved, but regular orbits now have two additional effective integrals of motion, I_2 and I_3 , which are not known explicitly.

Schwarzschild (1979, 1982) devised a numerical method which sidesteps our ignorance about the non-classical integrals of motion. It allows for an arbitrary gravitational potential, which may include contributions from dark components, integrates the equations of motion for a representative library of orbits, computes the density distribution of each orbit, and then determines the orbital weights such that the combined orbital densities reproduce the density of the system. The best-fitting orbital weights represent the DF (cf. Vandervoort 1984). Pfenniger (1984) and Richstone & Tremaine (1984) included kinematic moments in this method, and Rix et al. (1997) showed how to include observed LOSVDs. A number of groups have developed independent numerical implementations of Schwarzschild’s method for axisymmetric geometry which fit the projected surface brightness and line-of-sight velocity distributions of early-type galaxies in detail (van der Marel et al. 1998; Cretton et al. 1999; Gebhardt et al. 2000, Valluri, Merritt & Emsellem 2004; Thomas et al. 2004; Cappellari et al. 2006). Applications include the determination of central black hole masses (see also van der Marel et al. 1997; Cretton & van den Bosch 1999; Verolme et al. 2002; Cappellari et al. 2002; Gebhardt et al. 2003; Copin, Cretton & Emsellem 2004), accurate global dynamical mass-to-light ratios (Cappellari et al. 2006), as well as dark matter profiles as a function of radius (Cretton, Rix & de Zeeuw

* Hubble Fellow

† E-mail: glenn@ias.edu

2000; Thomas et al. 2005), and recovery of the DF (Krajnović et al. 2005). Van de Ven et al. (2006) and van den Bosch et al. (2006) included proper motion measurements in order to model nearby globular clusters, and determine their distance, inclination as well as mass-to-light ratio as function of radius. Finally, Verolme et al. (2003) and the companion paper van den Bosch et al. (2007, hereafter vdB07) describe an extension to triaxial geometry that includes all line-of-sight kinematics.

Although Schwarzschild models have significantly increased our understanding of the dynamical structure and evolution of early-type galaxies, questions remain about the uniqueness and the accuracy with which they are able to recover the global parameters as well as the internal dynamics of these galaxies. Many tests have been done to establish how the axisymmetric code recovers known input models, but these generally have been limited to spherical geometry or to an input axisymmetric DF that is a function of E and L_z only (van der Marel et al. 1998; Cretton et al. 1999; Verolme & de Zeeuw 2002; Valluri et al. 2004; Cretton & Emsellem 2004; Thomas et al. 2004; Krajnović et al. 2005).

One could construct a numerical galaxy model with Schwarzschild’s method itself, compute the observables, and then use these as input for the code and determine how well it recovers the input model. This is useful, but does not provide a fully independent test of the software. An alternative is to consider the special family of models with gravitational potential of Stäckel form, for which all three integrals of motion are exact and known explicitly. These separable potentials have a core rather than a central cusp, so the corresponding models cannot include a central black hole, and are inadequate for describing galactic nuclei. However, they can be constructed for a large range of axis ratios (Statler 1987), and their observed kinematic properties are as rich as those seen in the main body of early-type galaxies (Statler 1991, 1994; Arnold, de Zeeuw & Hunter 1994).

A small number of analytic DFs have been constructed for triaxial separable models. The ‘thin-orbit’ models (Hunter & de Zeeuw 1992) have the maximum possible streaming motions, but their DF contains delta functions, and they are therefore not particularly useful for a test of general-purpose numerical machinery. Dejonghe & Laurent (1991, hereafter DL91) constructed separable triaxial models in which the DF depends on a single parameter $S = E + wI_2 + uI_3$, which is a linear combination of the three exact integrals E , I_2 and I_3 admitted by these potentials, and is quadratic in the velocity components. For a given radial density profile, the DF follows by simple inversion of an Abel integral equation. These so-called Abel models have no net mean streaming motions, and are the axisymmetric and triaxial generalisations of the well-known spherical Osipkov–Merritt models (Osipkov 1979; Merritt 1985), for which the observables can be calculated easily (Carollo, de Zeeuw & van der Marel 1995). Mathieu & Dejonghe (1999, hereafter MD99) generalised the results of DL91 by including two families of DF components with net internal mean motions around the long and the short axis, respectively, and compared the resulting models with observations of Centaurus A. Although the Abel character of the non-rotating components is no longer conserved, the expressions for the velocity moments in these more general models can still be evaluated in a straightforward way. When the entire DF depends on the same single variable S the famous ellipsoidal hypothesis (e.g., Eddington 1915; Chandrasekhar 1940) applies, so that self-consistency is only possible in the spherical case (Eddington 1916; Camm 1941). This does not hold for Abel models with a DF that is a sum of components for which the variable S has different values of the parameters w and u . Such multi-

component Abel models can provide (nearly) self-consistent models with a large variety of shapes and dynamics.

Here, we show that for Abel models, in addition to the velocity moments, the full LOSVD can be calculated in a simple way. Next, we construct axisymmetric and triaxial Abel models to test our numerical implementation of Schwarzschild’s method. We assume a convenient form for the gravitational potential, and construct the DF that reproduces a realistic surface brightness distribution. We compute the LOSVDs of the models and derive two-dimensional maps of the resulting kinematics. We show that, despite the simple form of the DF, these models display the large variety of features observed in early-type galaxies with integral-field spectrographs such as SAURON (Emsellem et al. 2004). By fitting axisymmetric and triaxial three-integral Schwarzschild models to the simulated observables we find that Schwarzschild’s method is able to recover the internal dynamics and three-integral DF of early-type galaxies. In this paper we fix the mass-to-light ratio and viewing direction to those of the Abel models, while in our companion paper vdB07 we investigate how well these global parameters can be determined by Schwarzschild’s method, along with a full description of our numerical implementation in triaxial geometry.

This paper is organised as follows. In Section 2 we summarise the properties of the triaxial Abel models of DL91 and MD99 and present the intrinsic velocity moments in a form which facilitates their numerical implementation. We describe the conversion to observables in Section 3, including the computation of the LOSVD. In Section 4 we construct a specific triaxial galaxy model and in Section 5 we fit the simulated observables with our triaxial Schwarzschild models to investigate how well the intrinsic moments and three-integral DF are recovered. In Section 6 we consider Abel models in the axisymmetric limit and construct a three-integral oblate galaxy model to test our axisymmetric implementation of Schwarzschild’s method. We summarise our conclusions in Section 7. In Appendix A, we describe the simpler Abel models for the elliptic disc, large distance and spherical limit, and link them to the classical Osipkov–Merritt solutions for spheres. Readers who are mainly interested in the tests of the Schwarzschild method may skip Sections 2 – 4 and 6.1 – 6.3.

2 TRIAXIAL ABEL MODELS

The triaxial Abel models introduced by DL91 have gravitational potentials of Stäckel form, for which the equations of motion separate in confocal ellipsoidal coordinates. We briefly describe these potentials, and refer for further details to de Zeeuw (1985a). We then make a specific choice for the DF, for which the velocity moments simplify.

2.1 Stäckel potentials

We define confocal ellipsoidal coordinates (λ, μ, ν) as the three roots for τ of

$$\frac{x^2}{\tau + \alpha} + \frac{y^2}{\tau + \beta} + \frac{z^2}{\tau + \gamma} = 1, \quad (2.1)$$

with (x, y, z) the usual Cartesian coordinates, and with constants α, β and γ such that $-\gamma \leq \nu \leq -\beta \leq \mu \leq -\alpha \leq \lambda$. From the inverse relations

$$x^2 = \frac{(\lambda + \alpha)(\mu + \alpha)(\nu + \alpha)}{(\alpha - \beta)(\alpha - \gamma)}, \quad (2.2)$$

and similarly for y^2 and z^2 by cyclic permutation of $\alpha \rightarrow \beta \rightarrow \gamma \rightarrow \alpha$, it follows that a combination (λ, μ, ν) generally corresponds to eight different points $(\pm x, \pm y, \pm z)$. In these coordinates, the Stäckel potentials have the following form (Weinacht 1924)

$$V_S(\lambda, \mu, \nu) = \frac{U(\lambda)}{(\lambda - \mu)(\lambda - \nu)} + \frac{U(\mu)}{(\mu - \nu)(\mu - \lambda)} + \frac{U(\nu)}{(\nu - \lambda)(\nu - \mu)}, \quad (2.3)$$

where $U(\tau)$ is an arbitrary smooth function ($\tau = \lambda, \mu, \nu$). The right-hand side of eq. (2.3) can be recognised as the second order divided difference of $U(\tau)$. Henceforth, we denote it with the customary expression $U[\lambda, \mu, \nu]$, which is symmetric in its arguments (see Hunter & de Zeeuw 1992, eqs 2.1–2.3, 2.13 and 2.14). Addition of a linear function of τ to $U(\tau)$ does not change V_S .

The density ρ_S that corresponds to V_S can be found from Poisson's equation

$$4\pi G \rho_S(\lambda, \mu, \nu) = \nabla^2 V_S(\lambda, \mu, \nu), \quad (2.4)$$

or alternatively by application of Kuzmin's (1973) formula (see de Zeeuw 1985b). This formula shows that, once we have chosen the confocal coordinate system and the density along the short axis, the mass model is fixed everywhere by the requirement of separability¹. For centrally concentrated mass models, V_S has the x -axis as long-axis and the z -axis as short-axis. In most cases this is also true for the associated density (de Zeeuw, Peletier & Franx 1986).

2.2 Orbital structure

The Hamilton-Jacobi equation separates in (λ, μ, ν) for the potentials (2.3), so that every orbit has three exact integrals of motion (cf. de Zeeuw & Lynden-Bell 1985)

$$\begin{aligned} E &= \frac{1}{2} (v_x^2 + v_y^2 + v_z^2) + U[\lambda, \mu, \nu], \\ I_2 &= \frac{1}{2} T L_y^2 + \frac{1}{2} L_z^2 + \frac{1}{2} (\alpha - \beta) v_x^2 \\ &\quad + (\alpha - \beta) x^2 U[\lambda, \mu, \nu, -\alpha], \\ I_3 &= \frac{1}{2} L_x^2 + \frac{1}{2} (1 - T) L_y^2 + \frac{1}{2} (\gamma - \beta) v_z^2 \\ &\quad + (\gamma - \beta) z^2 U[\lambda, \mu, \nu, -\gamma], \end{aligned} \quad (2.5)$$

where v_x, v_y and v_z are the velocity components in the Cartesian coordinate system, and $L_x = yv_z - zv_y$, the component of the angular momentum vector parallel to the x -axis. The other two components, L_y and L_z , follow by cyclic permutation of $x \rightarrow y \rightarrow z \rightarrow x$ and $v_x \rightarrow v_y \rightarrow v_z \rightarrow v_x$. Furthermore, T is a triaxiality parameter defined as

$$T = (\beta - \alpha)/(\gamma - \alpha), \quad (2.6)$$

and $U[\lambda, \mu, \nu, \sigma]$ is the third-order divided difference of $U(\tau)$. All models for which $U'''(\tau) > 0$ have a similar orbital structure and support four families of regular orbits: boxes with no net rotation, inner and outer long-axis tubes with net rotation around the x -axis, and short-axis tubes with net rotation around the z -axis (Kuzmin 1973; de Zeeuw 1985a; Hunter & de Zeeuw 1992).

¹ A third method for the calculation of the density is to use $4\pi G \rho_S = H[\lambda, \lambda, \mu, \mu, \nu, \nu]$, where the fifth-order divided difference is of the function $H(\tau) = 4a(\tau)U'(\tau) - 2a'(\tau)U(\tau)$ with $a(\tau) = (\tau + \alpha)(\tau + \beta)(\tau + \gamma)$ and $U(\tau)$ defines the potential as in eq. (2.3). This result was obtained by Hunter in 1989 (priv. comm.) and by Mathieu & Dejonghe (1996). Similar expressions exist for the related families of potential-density pairs introduced in de Zeeuw & Pfenniger (1988).

According to Jeans (1915) theorem the phase-space distribution function (DF) is a function $f(E, I_2, I_3)$ of the isolating integrals of motion (cf. Lynden-Bell 1962; Binney 1982). The velocity moments of the DF are defined as

$$\mu_{lmn}(\lambda, \mu, \nu) = \iiint v_\lambda^l v_\mu^m v_\nu^n f(E, I_2, I_3) dv_\lambda dv_\mu dv_\nu, \quad (2.7)$$

where l, m and n are non-negative integers, and v_λ, v_μ and v_ν are the velocity components in the confocal ellipsoidal coordinate system. Many of the velocity moments vanish due to the symmetry of the orbits in these coordinates. The zeroth-order velocity moment is the mass density that corresponds to the DF

$$\rho_\star(\lambda, \mu, \nu) = \mu_{000}(\lambda, \mu, \nu). \quad (2.8)$$

In self-consistent models, ρ_\star must equal ρ_S given in eq. (2.4), the mass density that is related to the potential V_S by Poisson's equation.

2.3 Abel distribution function

Following DL91, we choose the DF to be a function of the three integrals of motion E, I_2 and I_3 as given in eq. (2.5) through one variable

$$f(E, I_2, I_3) = f(S), \quad \text{with} \quad S = -E + w I_2 + u I_3, \quad (2.9)$$

and w and u are two parameters². This choice for the DF is equivalent to the celebrated ellipsoidal hypothesis (e.g., Eddington 1915; Chandrasekhar 1940). Self-consistency is only possible in the spherical case (Eddington 1916; Camm 1941). On the other hand, these DFs can produce realistic (luminous) mass densities ρ_\star , which differ from the (total) mass density ρ_S , as in galaxies with dark matter (see also § 2.4 below when we combine DFs of the form [2.9] with different values for w and u .)

DL91 and MD99 divided the DF into three types of components. The non-rotating (NR) type is made of box orbits and tube orbits with both senses of rotation populated equally. The two rotating types, LR and SR, consist of tube orbits, and have net rotation around either the long axis or the short axis.

2.3.1 Velocity moments

Due to the choice (2.9) of the DF, the general expression (2.7) for the velocity moments can be simplified, as shown by DL91 for the non-rotating components and by MD99 for the rotating components. We recast their expressions into a different form to facilitate the numerical implementation. The resulting velocity moments are given by

$$\begin{aligned} \mu_{lmn}(\lambda, \mu, \nu) &= \sqrt{\frac{2^{l+m+n+3}}{H_{\mu\nu}^{l+1} H_{\nu\lambda}^{m+1} H_{\lambda\mu}^{n+1}}} \\ &\times \int_{S_{\min}}^{S_{\max}} T_{lmn} [S_{\text{top}}(\lambda, \mu, \nu) - S]^{(l+m+n+1)/2} f(S) dS, \end{aligned} \quad (2.10)$$

and set to zero at positions for which $S_{\max} \leq S_{\min}$. The terms $H_{\mu\nu}, H_{\nu\lambda}$ and $H_{\lambda\mu}$ in the square root in front of the integral are defined as

$$H_{\sigma\tau} = 1 + \frac{(\sigma + \alpha)(\tau + \alpha)}{\gamma - \alpha} w + \frac{(\sigma + \gamma)(\tau + \gamma)}{\alpha - \gamma} u, \quad (2.11)$$

² In contrast with DL91 and MD99, we choose $V_S \leq 0$ and $E \leq 0$, consistent with e.g. de Zeeuw (1985a).

[t]

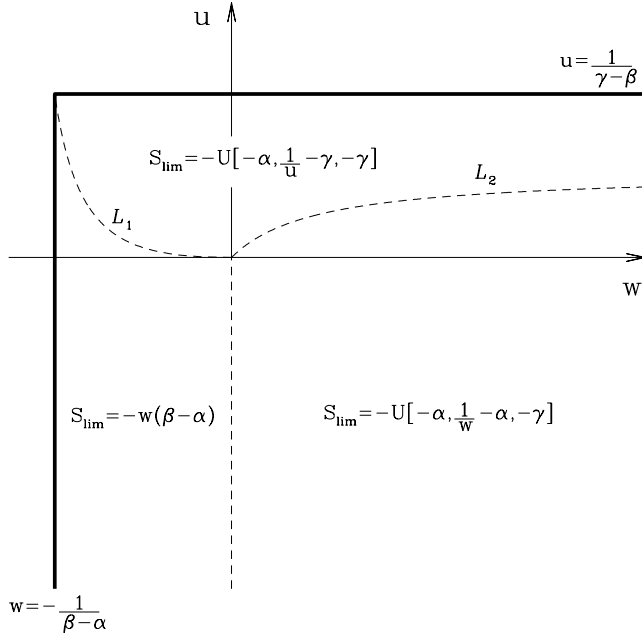


Figure 1. The limiting value S_{lim} of the variable $S = -E + w I_2 + u I_3$ as function of the parameters w and u . The physical region is bounded by the relations (2.12), indicated by the thick solid lines. The dashed curves divide this region into three parts, each with a different expression for S_{lim} . The relations for the separatrices L_1 and L_2 are given in eq. (2.13).

with $\sigma, \tau = \lambda, \mu, \nu$. Orbits are confined to the region of space for which all three terms are non-negative. In general, this condition will not be satisfied for all points, so that the Abel components have finite extent. From the requirement that at least the origin $(\lambda, \mu, \nu) = (-\alpha, -\beta, -\gamma)$ should be included, we find the following limits on w and u

$$w \geq -\frac{1}{\beta - \alpha} \quad \text{and} \quad u \leq \frac{1}{\gamma - \beta}. \quad (2.12)$$

The factor T_{lmn} in the integrand as well as the upper limit S_{max} of the integral are different for each of the three Abel component types NR, LR and SR, and are discussed in §§ 2.3.2–2.3.4 below. The lower limit of the integral S_{min} has to be at least as large as the smallest value possible for the variable S . This limiting value S_{lim} depends on the choice of the DF parameters w and u in (2.9), as is shown in Fig. 1 (cf. Fig. 7 of DL91). The boundaries follow from (2.12) and the separatrices L_1 and L_2 are given by

$$\begin{aligned} L_1 : \quad w &= \frac{U[-\alpha, \frac{1}{u} - \gamma, -\gamma]}{(\beta - \alpha)} \\ L_2 : \quad w &= \frac{u}{1 - (\gamma - \alpha)u}. \end{aligned} \quad (2.13)$$

At a given position (λ, μ, ν) , orbits with different values of the integrals of motion E , I_2 and I_3 , and hence different values of S , can contribute to the integral (2.10). The restriction to bound orbits ($E \leq 0$) together with the requirement that v_λ^2 , v_μ^2 and v_ν^2 all three have to be non-negative determines the part of the integral space that is accessible by orbits that go through (λ, μ, ν) . An example of the resulting tetrahedron in the (E, I_2, I_3) -space is shown in Fig. 2 (cf. Fig. 1 of MD99). The largest possible value of S is

[t]

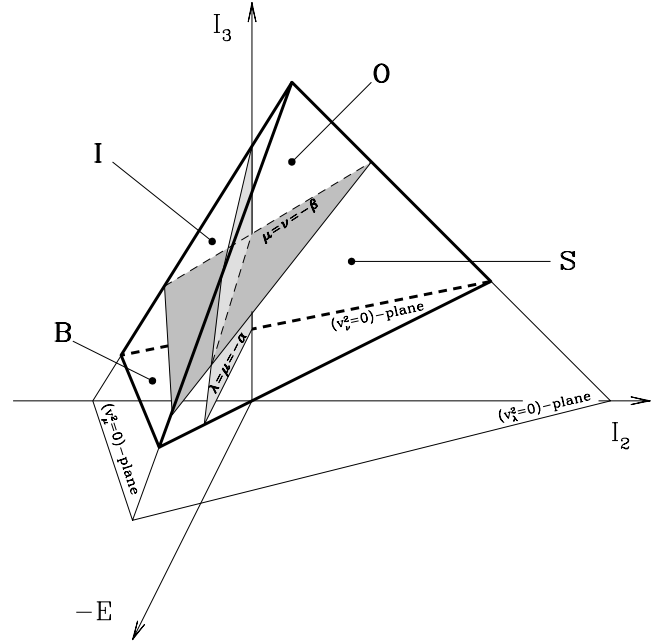


Figure 2. The tetrahedron shows all accessible points in integral space (E, I_2, I_3) for a given position (λ, μ, ν) . The tetrahedron is bounded by the planes for which $v_\lambda^2 = 0$, $v_\mu^2 = 0$, $v_\nu^2 = 0$ and $E = 0$, respectively. The two shaded planes, which are given by $v_\lambda^2 = v_\mu^2 = 0$ at $\lambda = \mu = -\alpha$ and $v_\mu^2 = v_\nu^2 = 0$ at $\mu = \nu = -\beta$, divide the tetrahedron into the parts corresponding to the four general orbit families in a triaxial separable potential: box (B) orbits, inner (I) and outer (O) long-axis tube orbits and short-axis (S) tube orbits.

given by the top of this tetrahedron

$$\begin{aligned} S_{\text{top}}(\lambda, \mu, \nu) &= -U[\lambda, \mu, \nu] \\ &\quad -w \frac{(\lambda + \alpha)(\mu + \alpha)(\nu + \alpha)}{\gamma - \alpha} U[\lambda, \mu, \nu, -\alpha] \\ &\quad -u \frac{(\lambda + \gamma)(\mu + \gamma)(\nu + \gamma)}{\alpha - \gamma} U[\lambda, \mu, \nu, -\gamma], \end{aligned} \quad (2.14)$$

which is thus a function of the position (λ, μ, ν) . At the origin $S_{\text{top}}(-\alpha, -\beta, -\gamma) = U[-\alpha, -\beta, -\gamma]$, which is the central value of the potential V_S . In what follows, we normalise V_S by setting $U[-\alpha, -\beta, -\gamma] = -1$, so that $0 \leq S_{\text{top}} \leq 1$.

2.3.2 Non-rotating components (NR)

Since the non-rotating component type can exist everywhere in the accessible integral space (the tetrahedron in Fig. 2), we simply have that $S_{\text{max}} = S_{\text{top}}(\lambda, \mu, \nu)$. Spatially the NR components are thus bounded by the surface $S_{\text{top}}(\lambda, \mu, \nu) = S_{\text{min}}$.

The factor T_{lmn} follows from the cross section of the S -plane within the tetrahedron and can be written in compact form as

$$T_{lmn}^{\text{NR}} = B\left(\frac{l+1}{2}, \frac{m+1}{2}, \frac{n+1}{2}\right), \quad (2.15)$$

where B is the beta function of three variables³. Since T_{lmn}^{NR} is independent of S it can be taken out of the integral (cf. eq. [3.10] of

³ The beta function of k variables in terms of the complete gamma function Γ is defined as $B(\beta_1, \dots, \beta_k) = \Gamma(\beta_1) \cdots \Gamma(\beta_k) / \Gamma(\beta_1 + \dots + \beta_k)$.

DL91), which then becomes of Abel form. Unfortunately, the inversion of eq. (2.10) for any chosen moment $\mu_{lmn}(\lambda, \mu, \nu)$, including the case $l = m = n = 0$, is generally impossible, as the left-hand side is a function of three variables, while the DF depends on only one variable, S . The density ρ_* specified along any given curve will define a different $f(S)$. A case of particular interest is to choose the density along the short axis to be $\rho_*(0, 0, z) = \rho_S(0, 0, z)$. This defines a unique $f(S)$, and hence gives ρ_* everywhere. Kuzmin's formula applied to $\rho_S(0, 0, z)$ similarly defines the density ρ_S everywhere. For single Abel DF components these will not be the same, except in the spherical limit (see Appendix A3).

Since the orbits have no net rotation, the velocity moments μ_{lmn}^{NR} are only non-zero when l, m and n are all three even, and vanish in all other cases.

2.3.3 Long-axis rotating components (LR)

The long-axis rotating component type only exists in the part of the integral space that is accessible by the (inner and outer) long-axis tube orbits. Within the tetrahedron for all orbits this is the region for which $v_\nu^2 \geq 0$ at $\nu = -\beta$. It follows that $S_{\text{max}} = S_{\text{top}}(\lambda, \mu, -\beta) \leq S_{\text{top}}(\lambda, \mu, \nu)$.

The term T_{lmn} follows from the cross section of the S -plane within the tetrahedron and with the above boundary plane $v_\nu^2 = 0$ at $\nu = -\beta$. Without any further constraint this results in zero net rotation, because each orbit with positive rotation around the long axis with $v_\nu > 0$, is balanced by an orbit with opposite direction of rotation with $v_\nu < 0$. Therefore, we restrict to orbits with $v_\nu \geq 0$, resulting in maximum streaming around the long axis for each LR component. This reduces the accessible integral space, and thus also the term T_{lmn} , by a factor of two, so that the latter becomes

$$T_{lmn}^{\text{LR}} = \frac{2(-2)^{(l+m)/2} \sqrt{a_0^{l+1} b_0^{m+1}} \mathcal{M}_0^{\text{LR}}}{(s+1)(s-1) \dots (s+1-(l+m))}, \quad (2.16)$$

with $s = l + m + n$, the parameters a_0 and b_0 defined as

$$\begin{aligned} a_0 &= \frac{(\lambda + \beta) H_{\mu\nu} [S_{\text{top}}(\lambda, \mu, -\beta) - S]}{(\lambda - \nu) H_{\mu(-\beta)} [S_{\text{top}}(\lambda, \mu, \nu) - S]}, \\ b_0 &= \frac{(\mu + \beta) H_{\nu\lambda} [S_{\text{top}}(\lambda, \mu, -\beta) - S]}{(\mu - \nu) H_{(-\beta)\lambda} [S_{\text{top}}(\lambda, \mu, \nu) - S]}, \end{aligned} \quad (2.17)$$

which for $S \leq S_{\text{max}} = S_{\text{top}}(\lambda, \mu, -\beta)$ are non-negative, and

$$\mathcal{M}_0^{\text{LR}} = \begin{cases} \mathcal{M}(s, \frac{l}{2}, \frac{m}{2}; a_0, b_0, \frac{\pi}{2}), & a_0 \leq b_0, \\ \mathcal{M}(s, \frac{m}{2}, \frac{l}{2}; b_0, a_0, \frac{\pi}{2}), & a_0 > b_0. \end{cases} \quad (2.18)$$

The function $\mathcal{M}(s, i, j; a, b, \phi)$ is defined in Appendix B, where we evaluate it in terms of elementary functions (odd s) and elliptic integrals (even s).

The LR components have maximum streaming around the long axis, but the motion parallel to the intermediate axis and short axis cancels. As a result, the velocity moments μ_{lmn}^{LR} vanish when l or m are odd⁴. Multiplying μ_{lmn}^{LR} with $(-1)^n$ results in maximum streaming in the opposite direction. By choosing different weights for both senses of rotation, we can control the direction and the amount of long-axis streaming motion for each LR component.

2.3.4 Short-axis rotating components (SR)

The short-axis component type reaches the part of integral space accessible by the short-axis tube orbits. Within the tetrahedron for all orbits this is the region for which $v_\mu^2 \geq 0$ both at $\mu = -\beta$ and $\mu = -\alpha$ (Fig. 2). The latter requirement is equivalent to $I_2 \geq 0$. In this case, $S_{\text{max}} = S_{\text{top}}(\lambda, -\alpha, \nu) \leq S_{\text{top}}(\lambda, \mu, \nu)$.

The form of the term T_{lmn} depends on the cross section of the S -plane within the tetrahedron and with the above two boundary planes. In case each SR component has maximum streaming around the short axis ($v_\mu \geq 0$), it is given by

$$T_{lmn}^{\text{SR}} = \frac{2(-2)^{(l+n)/2} \sum_{i=1}^2 \sqrt{a_i^{l+1} c_i^{n+1}} \mathcal{M}_i^{\text{SR}}}{(s+1)(s-1) \dots (s+1-(l+n))}. \quad (2.19)$$

The parameters a_1 and c_1 follow from a_0 and b_0 defined in (2.17) by interchanging $\mu \leftrightarrow \nu$, and in turn a_2 and c_2 follow from a_1 and c_1 by interchanging $\alpha \leftrightarrow \beta$. For the terms $\mathcal{M}_i^{\text{SR}}$ we have two possibilities, I and II,

$$\mathcal{M}_I^{\text{SR}} = \begin{cases} \mathcal{M}(s, \frac{l}{2}, \frac{n}{2}; a_I, c_I, \theta_I), & a_I \leq c_I, \\ \mathcal{M}(s, \frac{n}{2}, \frac{l}{2}; c_I, a_I, \frac{\pi}{2}) \\ - \mathcal{M}(s, \frac{n}{2}, \frac{l}{2}; c_I, a_I, \frac{\pi}{2} - \theta_I), & a_I > c_I, \end{cases} \quad (2.20)$$

$$\mathcal{M}_{II}^{\text{SR}} = \begin{cases} \mathcal{M}(s, \frac{l}{2}, \frac{n}{2}; a_{II}, c_{II}, \frac{\pi}{2}) \\ - \mathcal{M}(s, \frac{l}{2}, \frac{n}{2}; a_{II}, c_{II}, \theta_{II}), & a_{II} \leq c_{II}, \\ \mathcal{M}(s, \frac{n}{2}, \frac{l}{2}; c_{II}, a_{II}, \frac{\pi}{2} - \theta_{II}), & a_{II} > c_{II}, \end{cases} \quad (2.21)$$

where \mathcal{M} is given in Appendix B, and θ_I and θ_{II} follow from

$$\tan^2 \theta_I = \frac{c_{II}(a_I - a_{II})}{a_{II}(c_{II} - c_I)}, \quad \tan^2 \theta_{II} = \frac{c_I(a_{II} - a_I)}{a_I(c_I - c_{II})}. \quad (2.22)$$

For the assignment of the labels I and II , we discriminate between four cases

$$\begin{aligned} a_1 \leq a_2, \quad c_1 \geq c_2 & : I \rightarrow 1, \quad II \rightarrow 2, \\ a_1 \geq a_2, \quad c_1 \leq c_2 & : I \rightarrow 2, \quad II \rightarrow 1, \\ a_1 \leq a_2, \quad c_1 \leq c_2 & : I \rightarrow 1, \quad \theta_I = \pi/2, \quad C_2^{\text{SR}} = 0, \\ a_1 \geq a_2, \quad c_1 \geq c_2 & : I \rightarrow 2, \quad \theta_I = \pi/2, \quad C_1^{\text{SR}} = 0. \end{aligned} \quad (2.23)$$

The SR components have maximum streaming around the short axis, so that the velocity moments μ_{lmn}^{SR} vanish when l or n are odd. Multiplying μ_{lmn}^{SR} with $(-1)^m$ results in SR components with maximum streaming around the short axis in the opposite direction.

2.4 Combination of multiple DF components

Until now, we have chosen the Abel DF to be a function of a single variable $S = -E + wI_2 + uI_3$, and we have separated it in three component types, NR, LR and SR, but we have not made any assumption about the form of the DF (apart from the obvious requirement that it has to be non-negative everywhere and that it decreases to zero at large radii). Following MD99, we choose the DF to be a linear combination of basis functions of the form

$$f_\delta(S) = \left(\frac{S - S_{\text{min}}}{1 - S_{\text{min}}} \right)^\delta, \quad (2.24)$$

which, like the velocity moments (2.10), are non-vanishing as long as $S_{\text{lim}} \leq S_{\text{min}} \leq S \leq S_{\text{max}} \leq S_{\text{top}} \leq 1$. The exponent δ is a (non-negative) constant.

Once the Stäckel potential (2.3) is known by defining the function $U(\tau)$, we can use the above relations (§ 2.3) together with the expressions in Appendix B, to compute for a given basis function

⁴ Since $l + m$ is even, the factor $(-2)^{(l+m)/2}$ in eq. (2.16) is always real.

$f_\delta(S)$ the velocity moments (2.10) for the NR, SR and LR components in an efficient way, where at most the integral over S has to be evaluated numerically. For the NR components this integral can even be evaluated explicitly, resulting in

$$\mu_{lmn,\delta}^{\text{NR}}(\lambda, \mu, \nu) = \sqrt{\frac{[2(S_{\text{max}} - S_{\text{min}})]^{l+m+n+3}}{H_{\mu\nu}^{l+1} H_{\nu\lambda}^{m+1} H_{\lambda\mu}^{n+1}}} \times \left(\frac{S_{\text{max}} - S_{\text{min}}}{1 - S_{\text{min}}} \right)^\delta B\left(\frac{l+1}{2}, \frac{m+1}{2}, \frac{n+1}{2}, \delta+1\right), \quad (2.25)$$

where $S_{\text{max}} = S_{\text{top}}(\lambda, \mu, \nu)$ (cf. eq. 2.14).

Each DF component and corresponding velocity moments thus depend on the choice of the DF parameters w , u and δ , the type of component, and for the rotating components (LR and SR), they also depend on the sense of rotation around the axis of symmetry. By summing a series of DF basis functions over w , u and δ , one might even expect to cover a large fraction of all physical DFs. Due to the different values of w and u , such a sum of DF components is no longer a function of the same, single variable S , so that the ellipsoidal hypothesis does not apply. Consequently, it becomes possible to construct (nearly) self-consistent dynamical models, with the (combined) luminous mass density ρ_* equal (or close) to the mass density ρ_S associated to the potential.

3 OBSERVABLES

We describe how the intrinsic velocity moments can be converted to projected velocity moments on the plane of the sky. Alternatively, these line-of-sight velocity moments follow as moments of the LOSVD, which we show can be calculated in a straightforward way for Abel models. Parameterising the LOSVD as a Gauss-Hermite series, we obtain the observable quantities: the surface brightness, the mean line-of-sight velocity V , velocity dispersion σ , and higher-order Gauss-Hermite moments h_3, h_4, \dots

3.1 From intrinsic to observer's coordinate system

In order to calculate line-of-sight velocity moments, we introduce a new Cartesian coordinate system (x'', y'', z'') , with x'' and y'' in the plane of the sky and the z'' -axis along the line-of-sight. Choosing the x'' -axis in the (x, y) -plane of the intrinsic coordinate system (cf. de Zeeuw & Franx 1989 and their Fig. 2), the transformation between both coordinate systems is known once two viewing angles, the polar angle ϑ and azimuthal angle φ , are specified. The intrinsic z -axis projects onto the y'' -axis, which for an axisymmetric galaxy model aligns with the short axis of the projected surface density Σ . However, for a triaxial galaxy model the y'' -axis in general lies at an angle ψ with respect to the short axis of Σ . This misalignment ψ can be expressed in terms of the viewing angles ϑ and φ and the triaxiality parameter T (defined in eq. 2.6) as follows (cf. eq. B9 of Franx 1988)

$$\tan 2\psi = -\frac{T \sin 2\varphi \cos \vartheta}{\sin^2 \vartheta - T (\cos^2 \varphi - \sin^2 \varphi \cos^2 \vartheta)} \quad (3.1)$$

with $\sin 2\psi \sin 2\varphi \cos \vartheta \leq 0$ and $-\pi/2 \leq \psi \leq \pi/2$. A rotation over ψ transforms the coordinate system (x'', y'', z'') to (x', y', z') , with the x' -axis and y' -axis aligned with respectively the major and minor axis of Σ , whereas $z' = z''$ is along the line-of-sight.

The expressions in § 2.3 involve the velocity components in

the confocal ellipsoidal coordinate system (λ, μ, ν) . The conversion to line-of-sight quantities can be done by four successive matrix transformations. First, we obtain the velocity components in the first octant of the intrinsic Cartesian coordinate system (x, y, z) via \mathbf{Q} , of which the first element is given by (cf. DL91)

$$Q_{11} = \text{sign}(\lambda + \alpha) \sqrt{\frac{(\mu + \alpha)(\nu + \alpha)(\lambda + \beta)(\lambda + \gamma)}{(\alpha - \beta)(\alpha - \gamma)(\lambda - \mu)(\lambda - \nu)}}, \quad (3.2)$$

and the other elements follow horizontally by cyclic permutation of $\lambda \rightarrow \mu \rightarrow \nu \rightarrow \lambda$ and vertically by cyclic permutation of $\alpha \rightarrow \beta \rightarrow \gamma \rightarrow \alpha$. The second matrix uses the symmetries of the orbits to compute the appropriate signs of the intrinsic Cartesian velocities in the other octants. The result depends on whether or not the orbit has a definite sense of rotation in one of the confocal coordinates. For the three types of Abel components this results in the following matrices

$$\begin{aligned} \text{NR} &: \mathbf{S} = \text{diag}[\text{sgn}(x), \text{sgn}(y), \text{sgn}(z)] \\ \text{LR} &: \mathbf{S} = \text{diag}[\text{sgn}(xyz), \text{sgn}(z), \text{sgn}(y)] \\ \text{SR} &: \mathbf{S} = \text{diag}[\text{sgn}(y), \text{sgn}(x), \text{sgn}(xyz)] \end{aligned} \quad (3.3)$$

Finally, the conversion from the intrinsic to the observer's Cartesian velocities involves the same projection and rotation as for the coordinates. We represent these two coordinate transformations respectively by the projection matrix

$$\mathbf{P} = \begin{pmatrix} -\sin \varphi & \cos \varphi & 0 \\ -\cos \vartheta \cos \varphi & -\cos \vartheta \sin \varphi & \sin \vartheta \\ \sin \vartheta \cos \varphi & \sin \vartheta \sin \varphi & \cos \vartheta \end{pmatrix}, \quad (3.4)$$

and the rotation matrix

$$\mathbf{R} = \begin{pmatrix} \cos \psi & -\sin \psi & 0 \\ \sin \psi & \cos \psi & 0 \\ 0 & 0 & 1 \end{pmatrix}. \quad (3.5)$$

In this way, we arrive at the following relation

$$\begin{pmatrix} v_{x'} \\ v_{y'} \\ v_{z'} \end{pmatrix} = \mathbf{M} \begin{pmatrix} v_\lambda \\ v_\mu \\ v_\nu \end{pmatrix}, \quad \text{with } \mathbf{M} \equiv \mathbf{RPSQ}, \quad (3.6)$$

where the full transformation matrix \mathbf{M} is thus a function of (λ, μ, ν) , the constants (α, β, γ) and the viewing angles $(\vartheta, \varphi, \psi)$.

3.2 Line-of-sight velocity moments

We can now write each velocity moment in the observer's Cartesian coordinate system (x', y', z') as a linear combination of the velocity moments in the confocal ellipsoidal coordinate system

$$\mu_{ijk}(x', y', z') = \sum_{l,m,n} c_{l,m,n}(s) \mu_{lmn}(\lambda, \mu, \nu), \quad (3.7)$$

with $s = i + j + k = l + m + n$. The coefficients $c_{l,m,n}(s)$ are products of elements of the transformation matrix \mathbf{M} in eq. (3.6). They can be obtained with the following recursive algorithm

$$c_{l,m,n}(s) = \begin{cases} c_{1,0,0}(s) c_{l-1,m,n}(s-1), & \text{if } l > 0, \\ c_{0,1,0}(s) c_{0,m-1,n}(s-1), & \text{if } m > 0, \\ c_{0,0,1}(s) c_{0,0,n-1}(s-1), & \text{if } n > 0, \end{cases} \quad (3.8)$$

with the first order expressions given by

$$c_{1,0,0}(s) = M_{e_s 1}, \quad c_{0,1,0}(s) = M_{e_s 2}, \quad c_{0,0,1}(s) = M_{e_s 3}, \quad (3.9)$$

and $c_{0,0,0} = 1$. The index e_s is the s th element of the vector $\mathbf{e} = [3, \dots, 3, 2, \dots, 2, 1, \dots, 1]$, where the number of integers 3 (#3) is equal to the value of the velocity moment index k , and similarly #2 = j and #1 = i .

The line-of-sight velocity moments now follow from (numerical) integration of μ_{00k} along the line-of-sight

$$\mu_k(x', y') = \int_{-\infty}^{\infty} \mu_{00k}(x', y', z') dz', \quad (3.10)$$

which are thus functions of position on the sky plane.

3.3 Line-of-sight velocity distribution

Using the definition of the intrinsic velocity moments of the DF (eq. 2.7) and rearranging the sequence of integration, we rewrite eq. (3.10) for the line-of-sight velocity moments as

$$\mu_k(x', y') = \int_{-\infty}^{\infty} v_{z'}^k \mathcal{L}(x', y', v_{z'}) dv_{z'}, \quad (3.11)$$

where we have introduced the LOSVD

$$\mathcal{L}(x', y', v_{z'}) = \iiint f(E, I_2, I_3) dv_{x'} dv_{y'} dz'. \quad (3.12)$$

Although the integral over z' in general can only be evaluated numerically, we show that for the choice (2.9) of the DF, the double integral over the velocities can be simplified significantly.

Our analysis generalises the results for the well-known spherical Osipkov–Merritt models. We describe the spherical limit together with the elliptic disc and large distance limit in Appendix A, while we present axisymmetric Abel models in § 6.1.

3.3.1 Abel LOSVD

Substituting the expressions (2.5) for the integrals of motion in $S = -E + wI_2 + uI_3$, we obtain

$$S = S_{\text{top}}(\lambda, \mu, \nu) - \frac{1}{2} (H_{\mu\nu} v_\lambda^2 + H_{\nu\lambda} v_\mu^2 + H_{\lambda\mu} v_\nu^2), \quad (3.13)$$

where the expression for $S_{\text{top}}(\lambda, \mu, \nu)$ is given by eq. (2.14) and the terms $H_{\mu\nu}$, $H_{\nu\lambda}$ and $H_{\lambda\mu}$ are defined in eq. (2.11). Defining

$$X^2 = \frac{H_{\mu\nu}}{2[S_{\text{top}}(\lambda, \mu, \nu) - S]} v_\lambda^2, \quad (3.14)$$

and similarly Y and Z by cyclic permutation of $\lambda \rightarrow \mu \rightarrow \nu \rightarrow \lambda$, we can write the expression for S as

$$X^2 + Y^2 + Z^2 = 1. \quad (3.15)$$

For a given position (λ, μ, ν) , each value of S thus defines the surface of the unit sphere in the variables (X, Y, Z) . In these variables, we can write the integral of the DF over velocities, i.e., the stellar mass density, as

$$\begin{aligned} \rho_\star &= \iiint f(S) dv_{x'} dv_{y'} dv_{z'}, \\ &= \int_{S_{\min}}^{S_{\max}} \sqrt{\frac{2[S_{\text{top}} - S]}{H_{\mu\nu}H_{\nu\lambda}H_{\lambda\mu}}} f(S) \left[\iiint_{X^2+Y^2+Z^2=1} dX dY dZ \right] dS. \end{aligned} \quad (3.16)$$

This is the same expression as for the zeroth-order velocity moment of the DF, μ_{000} , in eq. (2.10), where $2T_{000}$ is equal to the integral between square brackets.

The matrix \mathbf{M} in eq. (3.6) provides the conversion from the velocity components in the confocal ellipsoidal coordinate system,

$(v_\lambda, v_\mu, v_\nu)$, to those in the observer's Cartesian coordinate system, $(v_{x'}, v_{y'}, v_{z'})$. Hence, for a given line-of-sight velocity $v_{z'}$, we find

$$e_1 X + e_2 Y + e_3 Z = v_{z'} / g(S). \quad (3.17)$$

The coefficients e_1 , e_2 and e_3 are defined as

$$\begin{aligned} h e_1 &= \sqrt{H_{\nu\lambda}H_{\lambda\mu}} M_{31}, \\ h e_2 &= \sqrt{H_{\lambda\mu}H_{\mu\nu}} M_{32}, \\ h e_3 &= \sqrt{H_{\mu\nu}H_{\nu\lambda}} M_{33}, \end{aligned} \quad (3.18)$$

and normalised with respect to h given by

$$h^2 = H_{\nu\lambda}H_{\lambda\mu} M_{31}^2 + H_{\lambda\mu}H_{\mu\nu} M_{32}^2 + H_{\mu\nu}H_{\nu\lambda} M_{33}^2. \quad (3.19)$$

These coefficients are functions of the position (λ, μ, ν) , the constants (α, β, γ) and the viewing angles $(\vartheta, \varphi, \psi)$ through the components of the matrix \mathbf{M} , and also depend on the DF parameters w and u through the terms $H_{\lambda\mu}$, $H_{\mu\nu}$ and $H_{\nu\lambda}$. It follows that

$$g(S) = h \sqrt{\frac{2[S_{\text{top}} - S]}{H_{\lambda\mu}H_{\mu\nu}H_{\nu\lambda}}}, \quad (3.20)$$

which is a function of the variable S .

We thus find that each combination of values of S and $v_{z'}$ results in the cross section of the surface of the unit sphere in eq. (3.15) with the plane in eq. (3.17), i.e., a circle, in the variables (X, Y, Z) . We rotate the latter coordinate system such that the normal vector (e_1, e_2, e_3) of the plane of the circle coincides with the Z' -axis of the system given by

$$\begin{pmatrix} X \\ Y \\ Z \end{pmatrix} = \begin{pmatrix} \cos \Phi & \sin \Phi \cos \Theta & \sin \Phi \sin \Theta \\ -\sin \Phi & \cos \Phi \cos \Theta & \cos \Phi \sin \Theta \\ 0 & -\sin \Theta & \cos \Theta \end{pmatrix} \begin{pmatrix} X' \\ Y' \\ Z' \end{pmatrix}. \quad (3.21)$$

where the rotation angles Φ and Θ follow from

$$\tan \Phi = \frac{e_1}{e_2}, \quad \tan \Theta = \frac{\sqrt{e_1^2 + e_2^2}}{e_3}. \quad (3.22)$$

In these coordinates the circle is conveniently parameterised as

$$X' = \sqrt{1 - Z'^2} \cos \xi', \quad Y' = \sqrt{1 - Z'^2} \sin \xi', \quad (3.23)$$

where $Z' = v_{z'} / g(S)$. We can now rewrite the integral between square brackets in eq. (3.16) as

$$\iint \left| \frac{\partial \mathbf{R}}{\partial \xi'} \wedge \frac{\partial \mathbf{R}}{\partial Z'} \right| d\xi' dZ' = \frac{1}{g(S)} \iint d\xi' dv_{z'}, \quad (3.24)$$

where the vector $\mathbf{R} = (X, Y, Z)$ and \wedge indicates the cross product. The integral over ξ' is the length of the part of the circle, $\Delta\xi'$, for which the corresponding integral space is accessible by orbits, and hence is in general a function of S and $v_{z'}$ and differs for the different types of Abel components as we show below.

Inserting eq. (3.24) in eq. (3.16), we obtain

$$\begin{aligned} \rho_\star &= \frac{1}{h} \int_{S_{\min} - g(S)}^{S_{\max}} \int_{g(S)}^{g(S)} f(S) \Delta\xi'(v_{z'}, S) dv_{z'} dS, \\ &= \frac{1}{h} \int_{-g(S_{\min})}^{g(S_{\min})} \int_{S_{\min}}^{S_{\text{up}}(v_{z'})} f(S) \Delta\xi'(v_{z'}, S) dS dv_{z'}, \end{aligned} \quad (3.25)$$

where after changing the order of integration in the last step, the upper limit of S is given by $S_{\text{up}} = \min[G(v_{z'}), S_{\max}]$, with

$$G(v_{z'}) = S_{\text{top}}(\lambda, \mu, \nu) - H_{\mu\nu}H_{\nu\lambda}H_{\lambda\mu} \frac{v_{z'}^2}{2h^2}. \quad (3.26)$$

Comparing the first line of eq. (3.16) with the second line of eq. (3.25), we see that the choice of the Abel DF, $f(E, I_2, I_3) = f(S)$, indeed reduces the triple integration (3.12) for the LOSVD to a double integral:

$$\mathcal{L}(x', y', v_{z'}) = \int_{-\infty}^{\infty} \frac{1}{h} \int_{S_{\min}}^{S_{\text{up}}(v_{z'})} f(S) \Delta \xi'(v_{z'}, S) dS dz', \quad (3.27)$$

and vanishes when $|v_{z'}|$ exceeds the 'terminal velocity' $v_t = g(S_{\min})$. The expressions for h and S_{up} follow from eqs (3.19) and (3.26), whereas S_{\max} and $\Delta \xi'$ are different for each of the three Abel component types and are considered next.

3.3.2 Non-rotating components (NR)

As for the intrinsic moments in § 2.3.2, we have for the non-rotating component type that $S_{\max} = S_{\text{top}}(\lambda, \mu, \nu)$, and, since the full integral space is accessible, $\Delta \xi'_{\text{NR}} = 2\pi$, independent of S and $v_{z'}$.

In the case of a basis function $f_\delta(S)$ as defined in eq. (2.24), the integral over S can be evaluated explicitly resulting in

$$\mathcal{L}_\delta^{\text{NR}} = \frac{2\pi}{(\delta+1)(1-S_{\min})^\delta} \int_{-\infty}^{\infty} \frac{1}{h} [G(v_{z'}) - S_{\min}]^{\delta+1} dz'. \quad (3.28)$$

3.3.3 Long-axis rotating components (LR)

The integral space accessible by the (inner and outer) long-axis tube orbits is given by $v_\nu^2 \geq 0$ at $\nu = -\beta$, so that immediately $S_{\max} = S_{\text{top}}(\lambda, \mu, -\beta)$, whereas the calculation of $\Delta \xi'_{\text{LR}}$ is more complex.

Since eq. (3.15) must also hold at $\nu = -\beta$, we find that for LR components, within the unit sphere in the variables (X, Y, Z) , the space is restricted to that within the elliptic cylinder given by

$$\frac{X^2}{a_0} + \frac{Y^2}{b_0} = 1, \quad (3.29)$$

where a_0 and b_0 are defined in eq. (2.17). In the rotated coordinate system (X', Y', Z') defined in eq. (3.21), at height $Z' = v_{z'}/g(S)$, the elliptic cylinder results in an ellipse given by

$$d_1 X'^2 + d_2 Y'^2 + d_3 X'Y' + d_4 X' + d_5 Y' + d_6 = 0 \quad (3.30)$$

for $0 \leq \xi' \leq 2\pi$ and with coefficients

$$\begin{aligned} d_1 &= (b_0 e_2^2 + a_0 e_1^2), \\ d_2 &= e_3^2 (b_0 e_1^2 + a_0 e_2^2), \\ d_3 &= 2e_1 e_2 e_3 (b_0 - a_0), \\ d_4 &= 2e_1 e_2 (e_1^2 + e_2^2)^{\frac{1}{2}} (b_0 - a_0) (v_{z'}/g), \\ d_5 &= 2e_3 (e_1^2 + e_2^2)^{\frac{1}{2}} (b_0 e_1^2 + a_0 e_2^2) (v_{z'}/g), \\ d_6 &= (e_1^2 + e_2^2) [(b_0 e_1^2 + a_0 e_2^2) (v_{z'}/g)^2 - a_0 b_0]. \end{aligned} \quad (3.31)$$

Because all the above relations only involve the squared values of X, Y and Z , they are independent of the sign of the corresponding velocities v_λ, v_μ and v_ν (cf. eq. 3.14), which results in zero net rotation. For the LR components, to obtain net rotation around the long axis, we simply limit the range of v_ν values, e.g., requiring $Z \geq 0$, results in maximum streaming motion around the long axis. This restricts the space in (X', Y', Z') , at given height $Z' = v_{z'}/g(S)$, to one side of the line

$$-(e_1^2 + e_2^2)^{\frac{1}{2}} Y' + e_3 (v_{z'}/g) = 0. \quad (3.32)$$

The restriction to the opposite side of the line inverts the rotation

around the long axis. By choosing different weights for both senses of rotation, we can control the direction and the amount of long-axis streaming motion.

For given values of S and $v_{z'}$, the integral space covered by the LR components is thus the part of the circle in eq. (3.23) that falls within the ellipse in eq. (3.30) and that is on the correct side of the line in eq. (3.32) (see also Fig. 3). The length $\Delta \xi'_{\text{LR}}$ of this part thus ranges from zero to a maximum of 2π when the circle is completely inside the ellipse and on the correct side of the line. To compute this length, we determine the points where the circle (possibly) intersects the ellipse and the line. Substituting the circle parameterisation of eq. (3.23) in the expression for the ellipse in eq. (3.30), we find that the intersections with the ellipse are the (real) zero points of the following fourth order polynomial in $u \equiv \tan(\xi'/2)$

$$\begin{aligned} (d_6 - d_4 R' + d_1 R'^2) u^4 + 2R' (d_5 - d_3 R') u^3 \\ + 2 [d_6 + (2d_2 - d_1) R'^2] u^2 + 2R' (d_5 + d_3 R') u \\ + (d_6 + d_4 R' + d_1 R'^2) = 0, \end{aligned} \quad (3.33)$$

where we have introduced $R' \equiv \sqrt{1 - (v_{z'}/g)^2}$. The intersections with the line result in the following two solutions

$$u_{\pm} = \frac{(e_1^2 + e_2^2)^{\frac{1}{2}} R' \pm [1 - e_3^2 - (v_{z'}/g)^2]^{\frac{1}{2}}}{e_3 (v_{z'}/g)}, \quad (3.34)$$

for $|v_{z'}| \leq g(S)(1 - e_3^2)^{\frac{1}{2}}$, otherwise the line is outside the circle.

We thus (numerically) find up to six real zero points u_i and corresponding angles $\xi'_i = 2 \arctan(u_i)$, sorted from low to high. For the set $\{-\pi, \xi'_1, \xi'_2, \dots, \pi\}$, we compute the lengths of the sequential intervals on the circle for which the corresponding values fall within the ellipse and on the correct side of the line. This can be checked by inserting a value from the corresponding interval, e.g. the central value, in eq. (3.23) and substituting the resulting X' and Y' into eqs (3.30) and (3.32). If the left-hand side is negative (positive), the interval is inside (outside) the ellipse, and (for $Z \geq 0$) on the wrong (correct) side of the line. Finally, the sum of the resulting interval lengths provides $\Delta \xi'_{\text{LR}}$.

3.3.4 Short-axis rotating components (SR)

The short-axis tube orbits are restricted to the region of integral space for which $v_\mu^2 \geq 0$ both at $\mu = -\beta$ and $\mu = -\alpha$, and hence $S_{\max} = S_{\text{top}}(\lambda, -\alpha, \nu)$. For the calculation of $\Delta \xi'_{\text{SR}}$ we have that the space within the unit sphere in (X, Y, Z) is now restricted to the part that falls within *both* the elliptic cylinders

$$\frac{X^2}{a_1} + \frac{Z^2}{c_1} = 1 \quad \text{and} \quad \frac{X^2}{a_2} + \frac{Z^2}{c_2} = 1. \quad (3.35)$$

As in § 2.3.4 for the intrinsic moments, a_1 and c_1 follow from a_0 and b_0 defined in (2.17) by interchanging $\mu \leftrightarrow \nu$, and in turn a_2 and c_2 follow from a_1 and c_1 by interchanging $\alpha \leftrightarrow \beta$.

Both elliptic cylinders result in ellipses in the Z' -plane, as in eq. (3.30) for the LR components, but now with coefficients

$$\begin{aligned} d_1 &= c_i e_2^2, \\ d_2 &= c_i e_1^2 e_3^2 + a_i (e_1^2 + e_2^2)^2, \\ d_3 &= 2c_i e_1 e_2 e_3 \\ d_4 &= 2c_i e_1 e_2 (e_1^2 + e_2^2)^{\frac{1}{2}} (v_{z'}/g), \\ d_5 &= 2e_3 (e_1^2 + e_2^2)^{\frac{1}{2}} [c_i e_1^2 - a_i (e_1^2 + e_2^2)] (v_{z'}/g), \\ d_6 &= (e_1^2 + e_2^2) [(c_i e_1^2 + a_i e_3^2) (v_{z'}/g)^2 - a_i c_i]. \end{aligned} \quad (3.36)$$

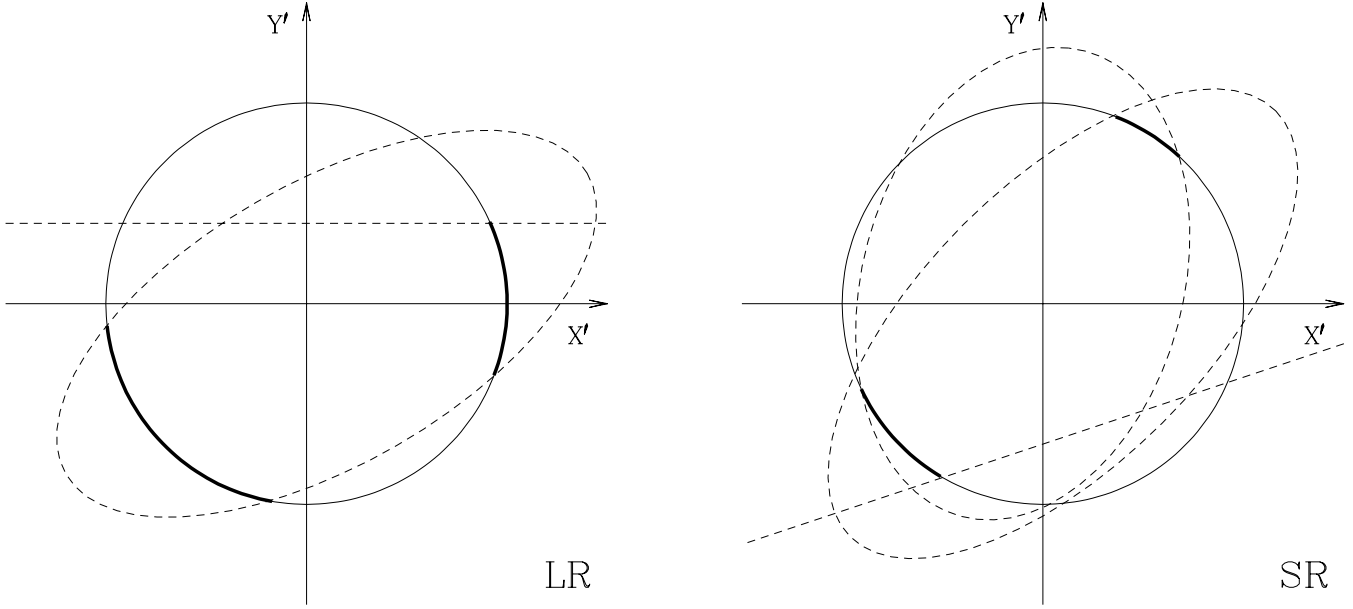


Figure 3. The part of integral space accessible by long-axis (left panel) and short-axis (right panel) tube orbits, for given values of the Abel DF variable S and the line-of-sight velocity $v_{z'}$. This corresponds to the thick part of the circle, which is restricted to be within the dashed ellipse(s) and below [above] the dashed line for long-axis [short-axis] rotating components with maximum streaming (see text for details). The length of the thick part of the circle equals $\Delta\xi'$ in the expression (3.27) of the LOSVD.

for $i = 1, 2$ respectively. The zero points of the corresponding fourth order polynomials in eq. (3.33) are again the intersections with the circle in eq. (3.23).

Net rotation around the short axis follows by limiting the range of v_μ values, e.g., $Y \geq 0$ yields maximum streaming, which restricts the accessible integral space to one side of the line

$$-e_1 X' + e_2 e_3 Y' + e_2 (e_1^2 + e_2^2)^{\frac{1}{2}} (v_{z'}/g) = 0. \quad (3.37)$$

The two solutions of the intersection with the circle are

$$u_{\pm} = \frac{-e_2 e_3 R' \pm (e_1^2 + e_2^2)^{\frac{1}{2}} [1 - e_2^2 - (v_{z'}/g)^2]^{\frac{1}{2}}}{e_1 R' + (e_1^2 + e_2^2)^{\frac{1}{2}} e_2 (v_{z'}/g)}, \quad (3.38)$$

for $|v_{z'}| \leq g(S)(1 - e_2^2)^{\frac{1}{2}}$, otherwise the line is outside the circle.

The combination of all the (real) zero points provides the (ordered) set $\{-\pi, \xi'_1, \xi'_2, \dots, \pi\}$, with at most ten intersections ξ'_i with the circle given in eq. (3.23). We compute the lengths of the circle intervals for which the enclosed values fall within both ellipses and on the correct side of the line. This means, for which the corresponding X' and Y' values substituted in eq. (3.30) result in a negative left-hand side for both pairs of a_i and b_i , and (for $Y \geq 0$) in a positive left-hand side of eq. (3.37). Finally, $\Delta\xi'_{\text{SR}}$ is the sum of the resulting interval lengths.

3.3.5 Other type of components

When considering the LR type of components we make no distinction between inner and outer long-axis tube orbits because they have similar dynamical properties. Similarly, the non-rotating box orbits are part of the NR type of components and are not considered separately. Nevertheless, if we are interested in the specific contribution of these orbit families to the LOSVD, this can be achieved by a straightforward extension of the above analysis.

As can be seen from Fig. 2, the inner and outer long-axis tube

orbits are separated by the plane $I_2 = 0$, or equivalently the regions for which $v_\lambda^2 \geq 0$ at $\lambda = -\alpha$ and $v_\mu^2 \geq 0$ at $\mu = -\alpha$, respectively. This is in addition to the restriction $v_\nu^2 \geq 0$ at $\nu = -\beta$ for both long-axis tube orbits. For the *inner* long-axis tube orbits this implies that $S_{\text{max}} = S_{\text{top}}(\lambda, \mu, -\beta)$. The space within the unit sphere in (X, Y, Z) is now restricted to the part that falls within the intersection of the elliptic cylinders in eq. (3.29) and

$$\frac{Y^2}{b_3} + \frac{Z^2}{c_3} = 1, \quad (3.39)$$

where b_3 and c_3 follow from a_0 and b_0 defined in (2.17) by interchanging $\nu \leftrightarrow \lambda$ and $\beta \leftrightarrow \alpha$. In the Z' -plane, these two elliptic cylinders result in ellipses as in eq. (3.30), with coefficients respectively given in eq. (3.31) and

$$\begin{aligned} d_1 &= c_3 e_1^2, \\ d_2 &= c_3 e_2^2 e_3^2 + b_3 (e_1^2 + e_2^2)^2, \\ d_3 &= -2 c_3 e_1 e_2 e_3 \\ d_4 &= -2 c_3 e_1 e_2 (e_1^2 + e_2^2)^{\frac{1}{2}} (v_{z'}/g), \\ d_5 &= 2 e_3 (e_1^2 + e_2^2)^{\frac{1}{2}} [c_3 e_1^2 - b_3 (e_1^2 + e_2^2)] (v_{z'}/g), \\ d_6 &= (e_1^2 + e_2^2) [(c_3 e_2^2 + b_3 e_3^2) (v_{z'}/g)^2 - b_3 c_3]. \end{aligned} \quad (3.40)$$

As before, $\Delta\xi'$ follows from the combination of the real zero points of the corresponding fourth order polynomials in eq. (3.33), and of eq. (3.32) in the case of maximum streaming around the long axis. For the *outer* long-axis tube orbits, $S_{\text{max}} = \min[S_{\text{top}}(\lambda, \mu, -\beta), S_{\text{top}}(\lambda, -\alpha, \nu)]$. The two elliptic cylinders are the one in eq. (3.29) and the second in eq. (3.35), with the coefficients of the corresponding ellipses in the Z' -plane are given in eq. (3.31) and eq. (3.36) ($i = 2$), respectively.

The part of integral space accessible by box orbits is the region for which both $v_\mu^2 \geq 0$ at $\mu = -\beta$ and $v_\lambda^2 \geq 0$ at $\lambda = -\alpha$ (Fig. 2). Therefore, $S_{\text{max}} = S_{\text{top}}(\lambda, \mu, \nu)$, and the two elliptic cylinders are the first in eq. (3.35) and the one in eq. (3.39). The coefficients of

the corresponding ellipses in the Z' -plane are respectively those in eq. (3.36) ($i = 1$) and in eq. (3.40).

3.4 Gauss-Hermite moments

We have seen that the line-of-sight velocity moments $\mu_k(x', y')$ can be derived either via line-of-sight integration of the intrinsic velocity moments (eq. 3.10) or as moments of the LOSVD (eq. 3.11). The lowest order line-of-sight velocity moments μ_0, μ_1 and μ_2 provide the surface mass density Σ , the mean line-of-sight velocity V and dispersion σ by

$$\Sigma = \mu_0, \quad V = \frac{\mu_1}{\mu_0}, \quad \text{and} \quad \sigma^2 = \frac{\mu_0 \mu_2 - \mu_1^2}{\mu_0^2}, \quad (3.41)$$

all three as a function of (x', y') . Whereas Σ, V and σ can be measured routinely, determinations of the higher order moments (μ_3, μ_4, \dots) are more complicated. Spectroscopic observations of the integrated light of galaxies provide the LOSVD as function of position on the sky plane. Unfortunately, the wings of the LOSVD become quickly dominated by the noise in the observations, and since the higher order moments significantly depend on the wings, their measurements can become very uncertain. Instead of these true higher-order moments, one often uses the Gauss-Hermite moments (h_3, h_4, \dots), which are much less sensitive to the wings of the LOSVD (van der Marel & Franx 1993; Gerhard 1993).

There is no simple (analytic) relation between the true moments and the Gauss-Hermite moments, including the lower order moments $\Sigma_{\text{GH}}, V_{\text{GH}}$ and σ_{GH} (but see eq. 18 of van der Marel & Franx 1993 for approximate relations to lowest order in h_3 and h_4). Nevertheless, we have shown that for Abel models the full LOSVD can be computed in an efficient way from eq. (3.27), so that by fitting a Gauss-Hermite series to the resulting LOSVD, we can derive the Gauss-Hermite moments accurately, all as function of (x', y') .

Still, the calculation of the line-of-sight velocity moments through the intrinsic moments is useful, e.g., in case of investigating a range of viewing directions. The intrinsic moments have to be computed once, after which only a (numerical) integration along the line-of-sight is needed for each viewing direction. This is (much) faster than calculating the LOSVD separately at each direction. The higher order true moments can even be used to (numerically) determine the Gauss-Hermite moments. One way is to find the Gauss-Hermite LOSVD of which the true moments best-fit those from the Abel model. However, in practise this direct fitting of the true moments has several (numerical) problems. Because it is a non-linear minimisation problem, the convergence can take long and may result in a local instead of the global best-fit solution, possibly resulting in Gauss-Hermite moments that are significantly different from their true values. If, instead, we first (re)construct the LOSVD from the true moments by means of an Edgeworth expansion (see Appendix C) and then fit a Gauss-Hermite series, the Gauss-Hermite moments can be calculated accurately and efficiently. Evidently, once the viewing direction is known, it is more straightforward to compute the full LOSVD to derive the (higher-order) Gauss-Hermite moments.

When we construct a galaxy model consisting of multiple Abel DF components (§ 2.4), we cannot simply combine the corresponding Gauss-Hermite moments in a linear way, because they are non-linear functions of the DF. Instead, we first add together the

LOSVDs of the different DF components⁵, each multiplied with a constant weight, and then parameterise the resulting combined LOSVD as a Gauss-Hermite series. Because the mass included in each DF component is different, in order to obtain the mass fractions per DF component, we multiply the latter weights with the mass of the corresponding DF component divided by the total (luminous) mass. To change the sense of rotation of a rotating DF component (LR or SR), the corresponding observables do not have to be recomputed, as a change in the sign of the odd velocity moments is sufficient.

3.5 Surface brightness

The surface brightness follows upon integration of the luminosity density along the line-of-sight. The luminosity density in turn is related to the mass density ρ_* via the stellar mass-to-light ratio M_*/L . With ρ_* the zeroth-order velocity moment of the DF (eq. 2.8), the surface brightness follows as

$$\text{SB}(x', y') = \int_{-\infty}^{\infty} (M_*/L)^{-1} \mu_{000}(x', y', z') dz'. \quad (3.42)$$

In the special case when (M_*/L) does not change (e.g., due to variation in the underlying stellar populations) with position, we can take it out of the integral and $\text{SB} = \Sigma/(M_*/L)$, where Σ is the surface mass density defined in eq. (3.41).

In addition to the luminous matter, a galaxy may also contain dark matter. While in the outer parts of late-type galaxies the presence of dark matter, as predicted by the cold dark matter paradigm for galaxy formation (e.g., Kauffmann & van den Bosch 2002), was demonstrated convincingly already more than two decades ago (e.g., van Albada et al. 1985), the proof in the outer parts of early-type galaxies remains uncertain, mainly due to a lack of kinematic constraints. As a consequence, in the outer parts of galaxies, commonly a simple functional form for the dark matter distribution is assumed, often the universal profile from the CDM paradigm (Navarro, Frenk & White 1997).

The dark matter distribution in the inner parts of galaxies is probably even more poorly understood (e.g., Primack 2004). For this reason, in current dynamical studies of the central parts of early-type galaxies, it is commonly assumed that both (M_*/L) and the dark matter fraction are constant, i.e., mass follows light. In this case the surface brightness also follows from $\text{SB} = \Sigma_S/(M/L)$, where (M/L) is the (constant) total mass-to-light ratio and Σ_S the surface mass density, which after deprojection yields ρ_S , the mass density related to the potential V_S via Poisson's equation (2.4). In case of a Stäckel potential (2.3), Σ_S (and hence the surface brightness) has concentric isodensity contours that show no twist (e.g., Franx 1988).

4 TRIAXIAL THREE-INTEGRAL GALAXY MODELS

After choosing a Stäckel potential, we investigate the shape of the density generated by the Abel DF components, and use these components to construct a triaxial galaxy model with three integrals of motion.

⁵ Or, in case the LOSVD is not readily accessible, the true line-of-sight velocity moments, which are also linear functions of the DF.

4.1 Isochrone potential

There are various choices for the potential that provide useful test models for comparison with the kinematics of triaxial elliptical galaxies (e.g., Arnold et al. 1994). One option is to consider the so-called perfect ellipsoid, for which Statler (1987) already computed numerical Schwarzschild models and Hunter & de Zeeuw (1992) investigated the maximum streaming thin orbit models. It has a density distribution stratified on similar concentric ellipsoids, but the potential function $U(\tau)$ contains elliptic integrals, which slows down numerical calculations. An alternative is to consider the set of models introduced by de Zeeuw & Pfenniger (1988), which have nearly ellipsoidal density figures, and have a potential and density that are evaluated easily and swiftly. They are defined by the choice:

$$U(\tau) = -GM\sqrt{\tau}(\tau + \beta), \quad (4.1)$$

so that the triaxial Stäckel potential has the elegant form

$$V_S(\lambda, \mu, \nu) = \frac{-GM(\sqrt{\lambda\mu} + \sqrt{\mu\nu} + \sqrt{\nu\lambda} - \beta)}{(\sqrt{\lambda} + \sqrt{\mu})(\sqrt{\mu} + \sqrt{\nu})(\sqrt{\nu} + \sqrt{\lambda})}, \quad (4.2)$$

where we set $GM = \sqrt{-\gamma} + \sqrt{-\alpha}$ so that $V_S(-\alpha, -\beta, -\gamma) = -1$ in the centre. In the oblate axisymmetric limit this potential is that of the Kuzmin-Kutuzov (1962) models of Dejonghe & de Zeeuw (1988), and in the spherical limit it reduces to Hénon's (1959) isochrone. For all these models, $V_S = U[-\alpha, -\beta, \tau]$ along the short z -axis is identical to the isochrone potential $-GM/(\sqrt{\tau} + \sqrt{-\alpha})$. We therefore refer to models with $U(\tau)$ of the form (4.1) as isochrone models. Since the potential falls off as $1/r$ at large radii, all these models have finite total mass.

The expressions for the integrals of motion are given in (2.5), where $U[\lambda, \mu, \nu] = V_S$ and the third order divided difference $U[\lambda, \mu, \nu, \sigma]$ is given by the symmetric expression⁶

$$U[\lambda, \mu, \nu, \sigma] = \frac{-GM - V_S(\sqrt{\lambda} + \sqrt{\mu} + \sqrt{\nu} + \sqrt{\sigma})}{(\sqrt{\lambda} + \sqrt{\sigma})(\sqrt{\mu} + \sqrt{\sigma})(\sqrt{\nu} + \sqrt{\sigma})}. \quad (4.3)$$

These triaxial isochrone models have the convenient property that the expressions for the potential and the integrals of motion contain only elementary functions of the (confocal ellipsoidal) coordinates and have no singularities.

The same is true for the associated mass density ρ_S , of which the expression is given in Appendix C of de Zeeuw & Pfenniger (1988), and a contour plot of ρ_S in the (x, z) -plane is shown in their Fig. 2. These authors also derive the axis ratios of ρ_S in the centre (their eq. C7) and at large radii (their eq. C11), in terms of the axis ratios ζ and ξ of the confocal ellipsoidal coordinate system, defined as

$$\zeta^2 = (-\beta)/(-\alpha), \quad \xi^2 = (-\gamma)/(-\alpha). \quad (4.4)$$

Although ρ_S becomes slightly rounder at larger radii, its axis ratios remain smaller than unity (for $\xi < \zeta < 1$) because at large radii $\rho_S \sim 1/r^4$ in all directions. Characteristic values for the axis ratios can be obtained from the (normalised) moments of inertia along the principal axes of the density,

$$a^2 = \frac{\int x^2 \rho(x, 0, 0) dx}{\int \rho(x, 0, 0) dx}, \quad (4.5)$$

where the intermediate and short semi-axis length, b and c , of

the inertia ellipsoid follow from the long semi-axis length a by replacing x with y and z , and at the same time $\rho(x, 0, 0)$ with $\rho(0, y, 0)$ and $\rho(0, 0, z)$, respectively. Taking for example $\zeta = 0.8$ and $\xi = 0.64$, the semi-axis lengths of the inertia ellipsoid result in the characteristic axis ratios $b_S/a_S = 0.88$ and $c_S/a_S = 0.80$ for the density ρ_S . The contours of the projected density are nearly elliptic with slowly varying axis ratios.

For triaxial mass models with a Stäckel potential V_S , de Zeeuw, Peletier & Franx (1986) have shown that the corresponding intrinsic mass density ρ_S cannot fall off more rapidly than $1/r^4$, except along the short z -axis. All models in which ρ_S falls off less rapidly than $1/r^4$ become round at large radii. When $\rho_S \sim 1/r^4$, as is the case for, e.g., the above isochrone potential and the perfect ellipsoid (e.g., de Zeeuw 1985a), the model remains triaxial at large radii. Moreover, mass models containing a linear combination of different Stäckel potentials are possible as long as the associated confocal ellipsoidal coordinate systems share the same foci (e.g., de Zeeuw & Pfenniger 1988; Batsleer & Dejonghe 1994). This shows that, although we choose here a (single-component) isochrone potential, our method is capable of providing Abel models for a large range of Stäckel potentials, with a similarly large range of shapes of the corresponding mass model. The same holds true for the luminous mass density, which we consider next.

4.2 The shape of the luminous mass density

Whereas the shape of the (total) mass density ρ_S is fixed by the choice of the potential V_S , and ζ and ξ (eq. 4.4), the shape of the (luminous) mass density ρ_* , which is the zeroth order velocity moment of the DF (eq. 2.8), also depends on the DF parameters w , u and δ , and the type of component. For $\zeta = 0.8$ and $\xi = 0.64$, we show in Fig. 4 for non-rotating DF components the characteristic (eq. 4.5) axis ratios of the corresponding density, as function of w and u . We have set $\delta = 1$, but the axis ratios depend only weakly on it, with ρ_* becoming slightly flatter for increasing δ . The thick contours are drawn at the levels that correspond to the values of the characteristic axis ratios of ρ_S , respectively $b_S/a_S = 0.88$, $c_S/b_S = 0.90$ and $c_S/a_S = 0.80$. These values are independent of w and u (as well as the other DF parameters).

While the intermediate-over-long axis ratio b/a increases with increasing w , its value is only weakly dependent of u . By contrast, the short-over-intermediate axis ratio c/b mainly increases with increasing u . The short-over-long axis ratio c/a is the product of the previous two axis ratios and thus depends on both w and u . When both w and u are negative, the density ρ_* has its long-axis along the x -axis and its short-axis along the z -axis, in the same way as the potential V_S and the associated density ρ_S . Above certain positive values of either w or u , the axis ratios become larger than unity, which means that ρ_* is no longer aligned with the underlying coordinate system in the same way as V_S and ρ_S . For example, when $(-\alpha)w = -0.5$ and $(-\alpha)u = 0.5$, $b/a < 1$ but $c/b > 1$, so that in this case ρ_* has its short axis along the y -axis.

A change in the sign of w and u has a strong effect on the radial slope of ρ_* . In Fig. 5, the radial profiles of ρ_* along the principal axes are shown for three combinations of w and u . The density is normalised to the central value ρ_0 . The profiles along the y -axis (dotted curves) and along the z -axis (dashed curves) are arbitrarily offset vertically with respect to the profile along the x -axis (solid curves) to enhance visualisation. The thin curves are the profiles of the (luminous) mass density ρ_* for varying δ , from $\delta = 0$ (darkest curve) to $\delta = 4$ (lightest curve), in unit steps. The thick black

⁶ Substituting eq. (4.2) shows that $U[\lambda, \mu, \nu, \sigma]$ is in fact fully symmetric:
$$\frac{U[\lambda, \mu, \nu, \sigma]}{GM} = \frac{\sqrt{\lambda\mu\nu\sigma} + \sqrt{\mu\nu\sigma\lambda} + \sqrt{\nu\sigma\lambda\mu} + \sqrt{\sigma\lambda\mu\nu} - \beta(\sqrt{\lambda} + \sqrt{\mu} + \sqrt{\nu} + \sqrt{\sigma})}{(\sqrt{\lambda} + \sqrt{\mu})(\sqrt{\mu} + \sqrt{\nu})(\sqrt{\nu} + \sqrt{\lambda})(\sqrt{\lambda} + \sqrt{\sigma})(\sqrt{\mu} + \sqrt{\sigma})(\sqrt{\nu} + \sqrt{\sigma})}$$

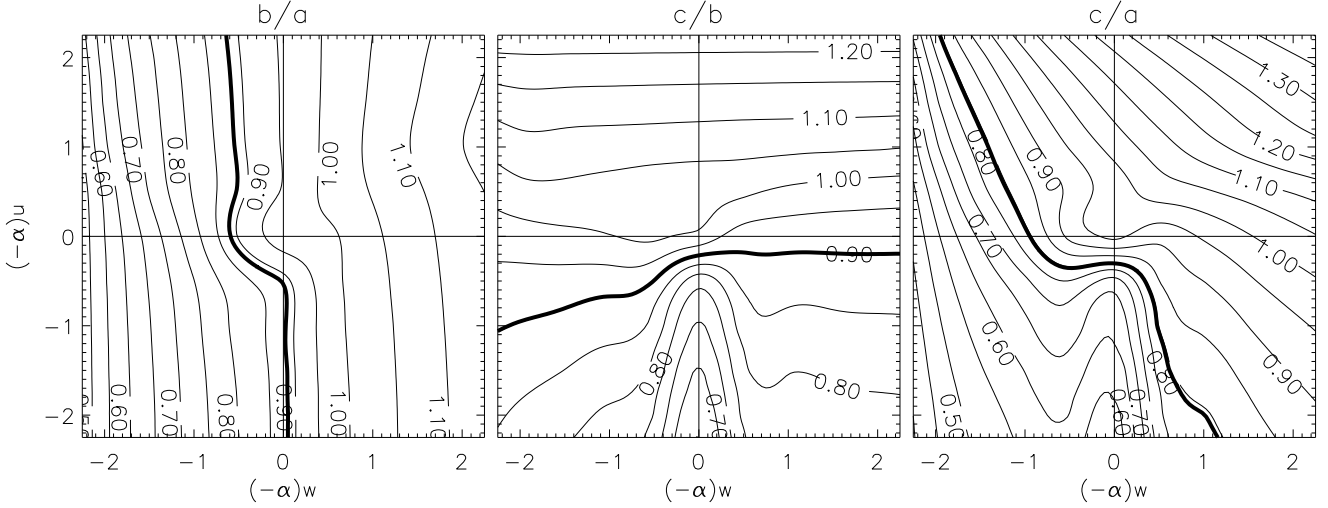


Figure 4. The characteristic axis ratios b/a , c/b and c/a of the luminous mass density for a non-rotating Abel component, as function of the DF parameters w and u , while $\delta = 1$. The axis ratios of the confocal ellipsoidal coordinate system are $\zeta = 0.8$ and $\xi = 0.64$, so that cf. (2.12) $(-\alpha)w \geq -25/9 \approx -2.78$ and $(-\alpha)u \leq 625/144 \approx 4.34$. The thick contours are drawn at the levels that correspond to the characteristic axis ratios of the total mass density ρ_S , associated with the underlying isochrone Stäckel potential (4.2), respectively $b_S/a_S = 0.88$, $c_S/b_S = 0.90$ and $c_S/a_S = 0.80$. The intermediate-over-long axis ratio b/a depends mainly on w , the short-over-intermediate axis ratio c/b depends mainly on u , and c/a is the product of the previous two.

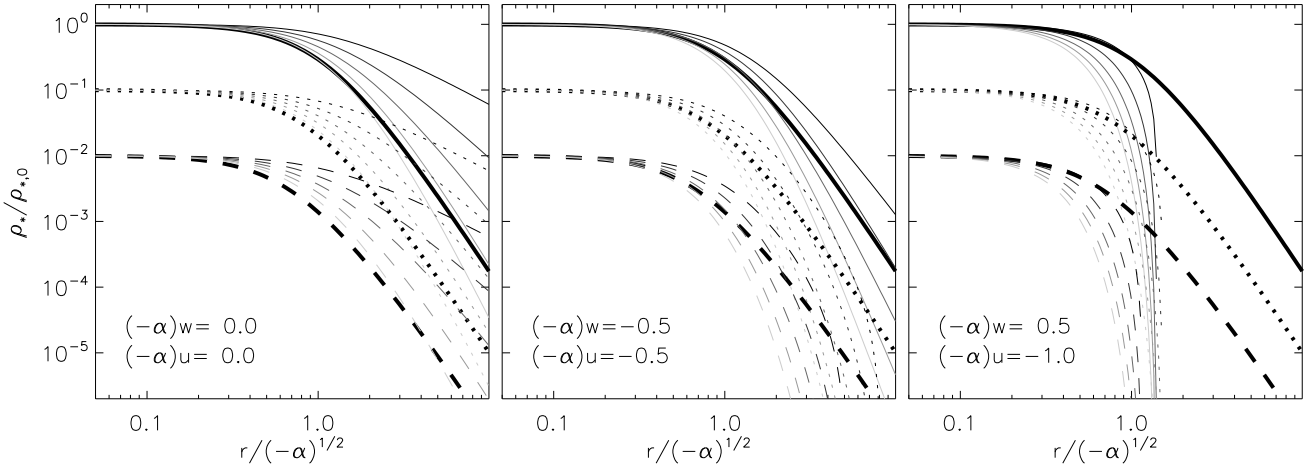


Figure 5. Principal axes profiles of the luminous mass density ρ_* for a non-rotating Abel component, normalised to the central value $\rho_{*,0}$. Each panel is for a different combination of the DF parameters w and u , while the grey scale indicates variation in δ from zero (darkest curve) to four (lightest curve), in unity steps. The profiles along the y -axis (dotted curves) and along the z -axis (dashed curves) are arbitrarily offset vertically with respect to the profile along the x -axis (solid curves) to enhance visualisation. The thick black curves show the profiles for the (total) mass density ρ_S , associated with the underlying isochrone Stäckel potential (4.2), with $\zeta = 0.8$ and $\xi = 0.64$. When the value of either w or u is positive (right panel), the profiles show a break at $r \sim \sqrt{-\alpha}$, so that these compact components may be used to represent kinematically decoupled components.

curves show the profiles for the (total) mass density ρ_S , which is independent of w , u and δ .

The profiles of ρ_* steepen for increasing δ and for increasing absolute values of w and u . In particular, when either w or u becomes positive (right panel), the profiles suddenly become much steeper and drop to zero already at relatively small radii $r \sim \sqrt{-\alpha}$. The resulting Abel components are thus compact and, as we saw above, can be different in shape and orientation from the main body of the galaxy model. Therefore, they can be used to represent kinematically decoupled components. When both $w \leq 0$ and $u \leq 0$ (left and middle panel), ρ_* falls off much more gently and the Abel components cover a larger region. When $w = u = 0$ (left panel),

so that the DF only depends on energy, the profiles as well as the shape (Fig. 4) of ρ_* can even be flatter than those of ρ_S . However, already for small non-zero values of w and u , generally $\rho_* \leq \rho_S$ everywhere in the galaxy model, and $\rho_* < \rho_S$ in the outer parts. Although self-consistency $\rho_* = \rho_S$ is only possible in the spherical case (for fixed values of w and u , see § 2.3), one can choose the parameters w , u and δ so that $\rho_* \sim \rho_S$. At the same time, having $\rho_* < \rho_S$ in the outer parts of the galaxy model, allows for a possible dark halo contribution.

The shape of ρ_* can furthermore change due to the additional contribution from long-axis rotating and short-axis rotating components. Although these components have no density along their ro-

tation axis, the behaviour of their overall shape as function of w , u and δ is similar as for the corresponding non-rotating components.

The above analysis shows that, given the triaxial isochrone potential (4.2), we can use Abel components to construct a galaxy model with a realistic density. Depending on the choice of w , u and δ , the galaxy model can contain compact (kinematically decoupled) components and account for possible dark matter (in the outer parts). Furthermore, we show below that even with a small number DF components, enough kinematic variation is possible to mimic the two-dimensional kinematic maps of early-type galaxies provided by observations with current integral-field spectrographs. This means that we can construct simple but realistic galaxy models to test our Schwarzschild software (§ 5 and 6.4).

4.3 A triaxial Abel model

As before, we choose the isochrone Stäckel potential (4.2), we take $\zeta = 0.8$ and $\xi = 0.64$ for the axis ratios of the coordinate system (4.4), resulting in a triaxiality parameter (2.6) of about $T = 0.61$, and we set the scale length $\sqrt{-\alpha} = 10''$. Assuming a distance of $D = 20$ Mpc and a total mass of $10^{11} M_\odot$ results in a central value for the potential $V_0 \sim 2.7 \times 10^5 \text{ km}^2 \text{ s}^{-2}$, which also sets the unit of velocity. We restrict the number of DF components to three, one of each type. For the first component of type NR we set $w = u = -0.5/(-\alpha)$ and $\delta = 1$, so that the shape of the corresponding density is similar to that of ρ_S , except in the outer parts where a steeper profile mimics the presence of dark matter (see Figs. 4 and 5). For the second and third component, respectively of type LR and SR, we adopt the same parameters, expect that we take $w = 0.5/(-\alpha)$ and $u = -1.0/(-\alpha)$ for the SR component, which therefore is more compact than the NR and LR component.

We set the line-of-sight by choosing $\vartheta = 70^\circ$ and $\varphi = 30^\circ$ for the viewing angles. After rotation over the misalignment angle $\psi = 101^\circ$ eq. (3.1), we compute for each DF component the LOSVD as a function of the positions on a rectangular grid on the sky plane, illustrated in Fig. 6 for five sky positions. By fitting a Gauss-Hermite series to each LOSVD, we obtain the maps of the mean line-of-sight surface mass density Σ , velocity V , dispersion σ and higher-order Gauss-Hermite moments h_3 and h_4 , shown in Fig. 7. The parameters of each DF component are given on the right. The NR component has zero (green) odd velocity moments. For the LR and SR component, the even velocity moments show a decrease in the centre, because these components have zero density along respectively the intrinsic long and short axis. We add the LOSVDs of the NR, LR and SR components, weighted with mass fractions of respectively 80%, 12.5% and 7.5%, and fit a Gauss-Hermite series to obtain maps of Σ , V , σ , h_3 and h_4 . We convert Σ to the surface brightness by dividing by a constant stellar mass-to-light ratio of $(M_*/L) = 4 M_\odot/L_\odot$.

To convert these ‘perfect’ kinematics to ‘realistic’ observations, similar to those obtained with integral-field spectrographs such as SAURON (Bacon et al. 2001), we finally apply the following steps. We compute the kinematics on a rectangular grid consisting of 30 by 40 square pixels of $1''$ in size. Using the adaptive spatial two-dimensional binning scheme of Cappellari & Copin (2003), we bin the pixels according to the criterion that each of the resulting (Voronoi) bins contains a minimum in signal-to-noise (S/N), which we take proportional to the square root of the surface brightness. For the mean errors in the kinematics we adopt the typical values of 7.5 km s^{-1} for V and σ and 0.03 for h_3 and h_4 in the kinematics of a representative sample of early-type galaxies observed with SAURON (Emsellem et al. 2004). We then weigh these val-

ues with the S/N in each bin to mimic the observed variation in measurement errors across the field. Finally, we use the computed measurement errors to (Gaussian) randomise the kinematic maps. In this way, we include the randomness that is always present in real observations. The resulting kinematic maps are shown in the top panels of Fig. 8. Because of the eight-fold symmetry of the triaxial model, the maps of the even (odd) velocity moments are always point-(anti)-symmetric, apart from the noise added.

5 RECOVERY OF TRIAXIAL GALAXY MODELS

We briefly describe our numerical implementation of Schwarzschild’s method in triaxial geometry (see vdB07 for a full description), which we then use to fit the observables of the triaxial Abel model constructed in § 4.3. We investigate the recovery of the intrinsic velocity moments and, through the distribution of the orbital mass weights, the recovery of the three-integral DF.

5.1 Triaxial Schwarzschild models

The first step is to infer the gravitational potential from the observed surface brightness. We do this by means of the Multi-Gaussian Expansion method (MGE; e.g., Cappellari 2002), which allows for possible position angle twists and ellipticity variations in the surface brightness. For a given set of viewing angles $(\vartheta, \varphi, \psi)$ (see § 3.1), we deproject the surface brightness and we multiply it by a mass-to-light ratio (M/L) to get the intrinsic mass density, from which the gravitational potential then follows by solving Poisson’s equation. We calculate orbits numerically in the resulting gravitational potential.

To obtain a representative library of orbits, the integrals of motion have to be sampled well. The energy can be sampled directly, but since the other integrals of motion are generally not known, we start, at a given energy, orbits from a polar grid in the (x, z) -plane, which is crossed perpendicularly by all families of (regular) orbits. We restrict ourselves to the region in the first quadrant that is enclosed by the equipotential and the thin orbit curves to avoid duplication of the tube orbits. To have enough box orbits to support the triaxial shape, we also start orbits by dropping them from the equipotential surface (Schwarzschild 1979, 1993).

Assigning a mass weight γ_j to each orbit j from the library, we compute their combined properties and find the weighted superposition that best fits the observed surface brightness and (two-dimensional) kinematics. However, the resulting orbital weight distribution may vary rapidly, and hence probably corresponds to an unrealistic DF. To obtain a smoothly varying DF, we both dither the orbits by considering a bundle of integrated orbits that were started close to each other, and we regularise when looking for the best-fit set of orbital weights by requiring them to vary smoothly between neighbouring orbits (in integral space). Finally, the best-fit Schwarzschild model follows from the minimum in the (Chi-squared) difference between (photometric and kinematic) observables and the corresponding model predictions, weighted with the errors in the observables.

5.2 Fit to observables of a triaxial Abel model

In this case, the gravitational potential is known and given by the isochrone Stäckel potential V_S eq. (4.1). However, to closely simulate the Schwarzschild modelling of real galaxies, we infer the potential from a deprojection of an MGE fit of the surface mass

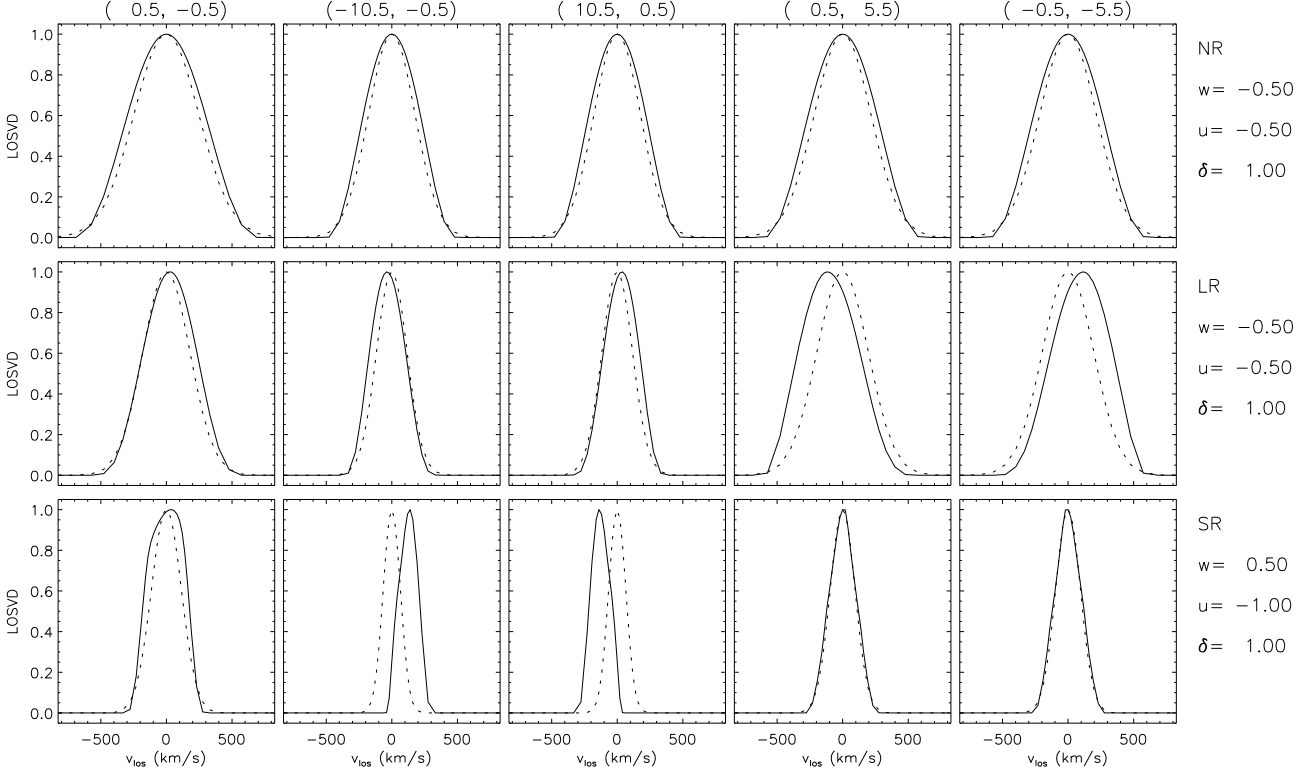


Figure 6. Line-of-sight velocity distribution (LOSVD) at five different positions (x', y') on sky-plane (in arcsec at the top of each column) of three different Abel components. The isochrone Stäckel potential (4.2) is used, with $\zeta = 0.8$ and $\xi = 0.64$ ($T = 0.61$), and scale length $\sqrt{-\alpha} = 10''$. The model is placed at a distance of $D = 20$ Mpc and the adopted viewing angles are $\vartheta = 70^\circ$ and $\varphi = 30^\circ$. From top to bottom the LOSVDs of a non-rotating (NR), long-axis rotating (LR) and short-axis rotating (SR) Abel component are shown, with the corresponding DF parameters w , u and δ given on the right. The height of each LOSVD is normalised to unity, and a (dashed) Gaussian distribution with zero mean and the same dispersion as the LOSVD is shown as a reference.

density Σ_S generated by V_S . The resulting potential reproduces V_S to high precision, with relative differences less than 10^{-3} . We compute a library of orbits by sampling 21 energies E via a logarithmic grid in radius from $1''$ to $123''$ that contains ≥ 99.9 per cent of the total mass. At each energy, we construct a uniform polar start space grid of 7 radii by 8 angles within the first quadrant of the (x, z) -plane and drop box orbits from a similar uniform polar grid on the equipotential surface in the first octant. This results in a total of $21 \times 7 \times 8 \times 2 = 2352$ starting positions, from each of which a bundle of 5^3 orbits are started. Taking into account the two senses of rotation of the tube orbits, this results in a total 441000 orbits that are numerically integrated in the potential.

We sum the velocities of each bundle of orbits in histograms with 401 bins, at a velocity resolution of 10 km s^{-1} . We fit the weighted sum of the velocity histograms to the intrinsic mass density ρ_* , which we obtain from a deprojection of an MGE fit to the observed surface brightness, multiplied with the (constant) $(M_*/L) = 4 \text{ M}_\odot/L_\odot$. Simultaneously, we fit the projected values of the velocity histograms to the observed surface brightness and higher-order velocity moments. Finally, at the same time, we regularise the orbital weights in E and in the starting positions by minimising their second order derivatives. The strenght of the regularisation is given by the a smoothening parameter (e.g., Cretton et al. 1999), which we set to $\lambda = 0.1$ (see vdB07).

From Fig. 8 it is clear that the (simulated) observables of the triaxial Abel model (top panels) are very well matched by the best-fit triaxial Schwarzschild model (bottom panels). The signature of

the kinematically decoupled component in the maps of the mean line-of-sight velocity V and Gauss-Hermite moment h_3 is accurately fitted, as well as the kinematics of the main body up to h_4 within the added noise (§ 4.3). Below we investigate how well the intrinsic velocity moments as well as the three-integral DF — which are not (directly) fitted — are recovered. Here, we keep the mass-to-light ratio and the viewing angles fixed to the input values of the triaxial Abel model (§ 4.3), while in vdB07 we vary these global parameters to study how well Schwarzschild’s method is able to determine them.

5.3 Intrinsic velocity moments

We calculate the intrinsic first and second order velocity moments of the Schwarzschild model by combining the appropriate moments of the orbits that receive weight in the superposition, and investigate how well they compare with the intrinsic velocity moments of the Abel model. In general, there are three first $\langle v_i \rangle$ and six second order velocity moments $\langle v_s v_t \rangle$ ($s, t = x, y, z$). Combining them yields the six dispersion components σ_{st} of the velocity dispersion tensor, where $\sigma_{st}^2 \equiv \langle v_s v_t \rangle - \langle v_s \rangle \langle v_t \rangle$.

We first consider the (x, z) -plane, as it is crossed perpendicularly by all four (major) orbit families. Because $\langle v_x \rangle = \langle v_z \rangle = \sigma_{xy} = \sigma_{yz} = 0$, we are left with $\langle v_y \rangle$ perpendicular to the (x, z) -plane as the only non-vanishing mean motion and σ_{zx} in the (x, z) -plane as the only non-vanishing cross-term. The average root-mean-square velocity dispersion σ_{RMS} is given by $\sigma_{\text{RMS}}^2 =$

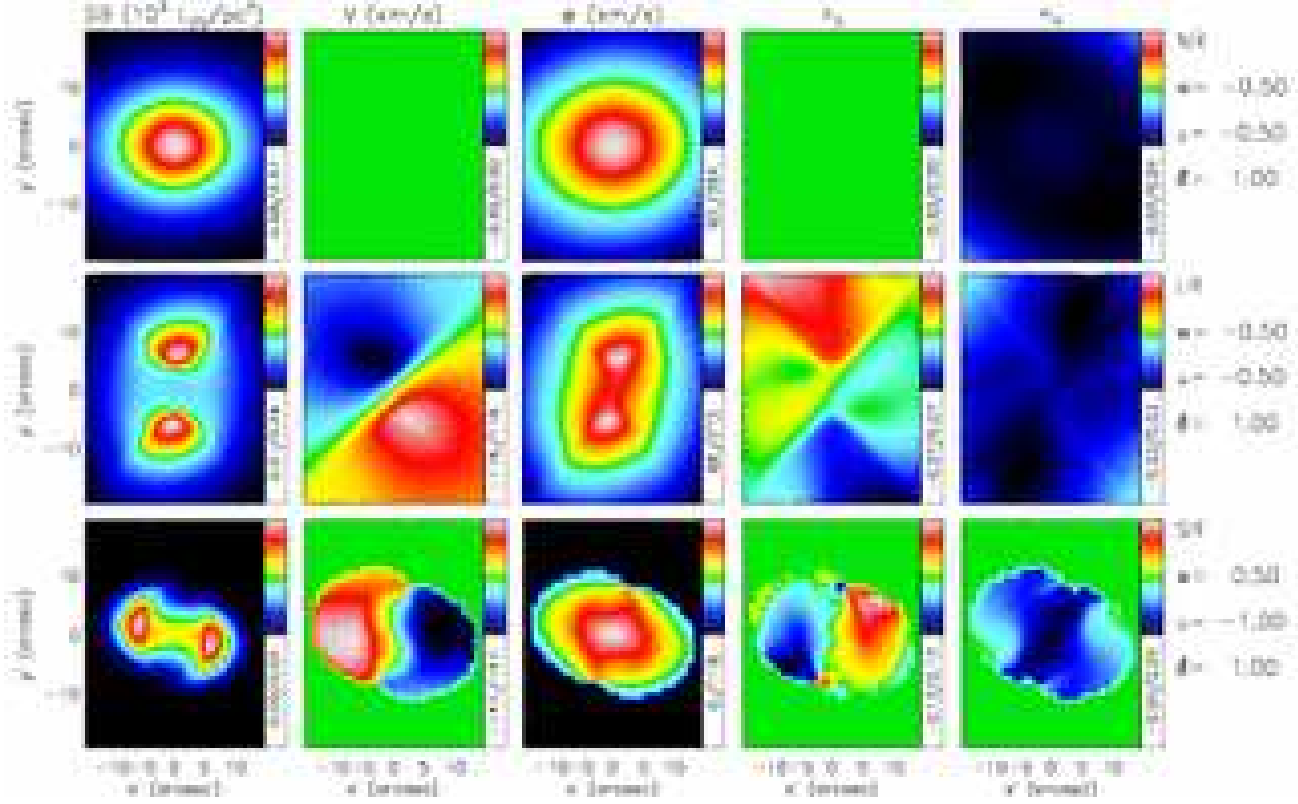


Figure 7. Maps of the surface brightness (SB; in $10^3 L_{\odot} \text{pc}^{-2}$), mean line-of-sight velocity V and dispersion σ (both in km s^{-1}), and higher order Gauss-Hermite moments h_3 and h_4 , of the same three Abel DF components as in Fig. 6, obtained by fitting a Gauss-Hermite series to the LOSVDs at each (pixel) position on the plane of the sky. The numerical artifacts at the edges of the compact SR component (third row) disappear when combined with components that extend over the full field-of-view (see e.g. the top row of Fig. 8).

$(\sigma_{xx}^2 + \sigma_{yy}^2 + \sigma_{zz}^2)/3$. The ratio $\langle v_y \rangle / \sigma_{\text{RMS}}$ of ordered-over-random motion is a measure of the importance of rotation for the gravitational support of a galaxy. In Fig. 9, the colours represent the values of this ratio in the (x, z) -plane, for the input triaxial Abel model (left panel) and for the best-fit triaxial Schwarzschild model (right panel).

In a Stäckel potential the axes of the velocity ellipsoid are aligned with the confocal ellipsoidal coordinate system (e.g., Edington 1915; van de Ven et al. 2003). As a result, one of the axes of the velocity ellipsoid is perpendicular to the (x, z) -plane, with semi-axis length σ_{yy} . The other two axes lie in the (x, z) -plane and have semi-axis lengths given by

$$\sigma_{\pm}^2 = \frac{1}{2}(\sigma_{xx}^2 + \sigma_{zz}^2) \pm \sqrt{\frac{1}{4}(\sigma_{xx}^2 - \sigma_{zz}^2)^2 + \sigma_{xz}^4}. \quad (5.1)$$

The ellipses overplotted in Fig. 9 show the corresponding cross sections of the velocity ellipsoid with the (x, z) -plane. The flattening of the ellipses is thus given by the ratio σ_{-}/σ_{+} , while the angle θ_{xz} of the major-axis with respect to the x -axis is given by⁷

$$\tan(2\theta_{xz}) = 2\sigma_{xz}^2 / (\sigma_{xx}^2 - \sigma_{zz}^2). \quad (5.2)$$

In addition, the cross on top of each ellipse represents the ratio

σ_{yy}/σ_{+} , i.e., the (relative) size of the velocity ellipsoid in the perpendicular direction. For an isotropic velocity distribution the ellipses become circles and the crosses fill the circles. Finally, the black curves are contours of constant mass density in steps of one magnitude.

The density of the triaxial Abel model (solid curve) is well fitted by the triaxial Schwarzschild model (dashed curve), with a (biweight⁸) mean fractional difference below 1%. In both the Abel model and the fitted Schwarzschild model the value of $\langle v_y \rangle / \sigma_{\text{RMS}}$ is relatively low, with a mean value ~ 0.14 , indicating that gravitational support is mainly due to random motion. Still, the average rotation of the long-axis tube orbits (with $\langle v_y \rangle < 0$) due to the maximum streaming LR component in the input Abel model, as well as, the opposite maximum streaming of the (compact) short-axis rotating component are clearly visible, and best recovered by the best-fit Schwarzschild model. The average absolute difference in both $\langle v_y \rangle$ and σ_{RMS} is below 6 km s^{-1} , and thus well within the typical error of 7.5 km s^{-1} assigned to the simulated mean line-of-sight velocity V and velocity dispersion σ of the Abel model (see § 4.3). The corresponding uncertainty in $\langle v_y \rangle / \sigma_{\text{RMS}}$ is ~ 0.03 .

We see in Fig. 9 that, at larger radii, the ellipses become more radially elongated and the relative size of the crosses decreases in the radial direction, but they still fill the ellipses in the angular direc-

⁷ In case of alignment with the confocal ellipsoidal coordinate system, this angle is given by the tangent to the curves of constant (μ, ν) , i.e., $\tan \theta_{xz} = (z/x)(\lambda + \alpha)/(\lambda + \gamma)$, which indicates approaching alignment with the polar coordinate system at large radius.

⁸ The biweight mean (e.g., Andrews et al. 1972; Beers, Flynn & Gebhardt 1990) is a robust estimator for a broad range of non-Gaussian underlying populations and is less sensitive to outliers than other moment estimators.

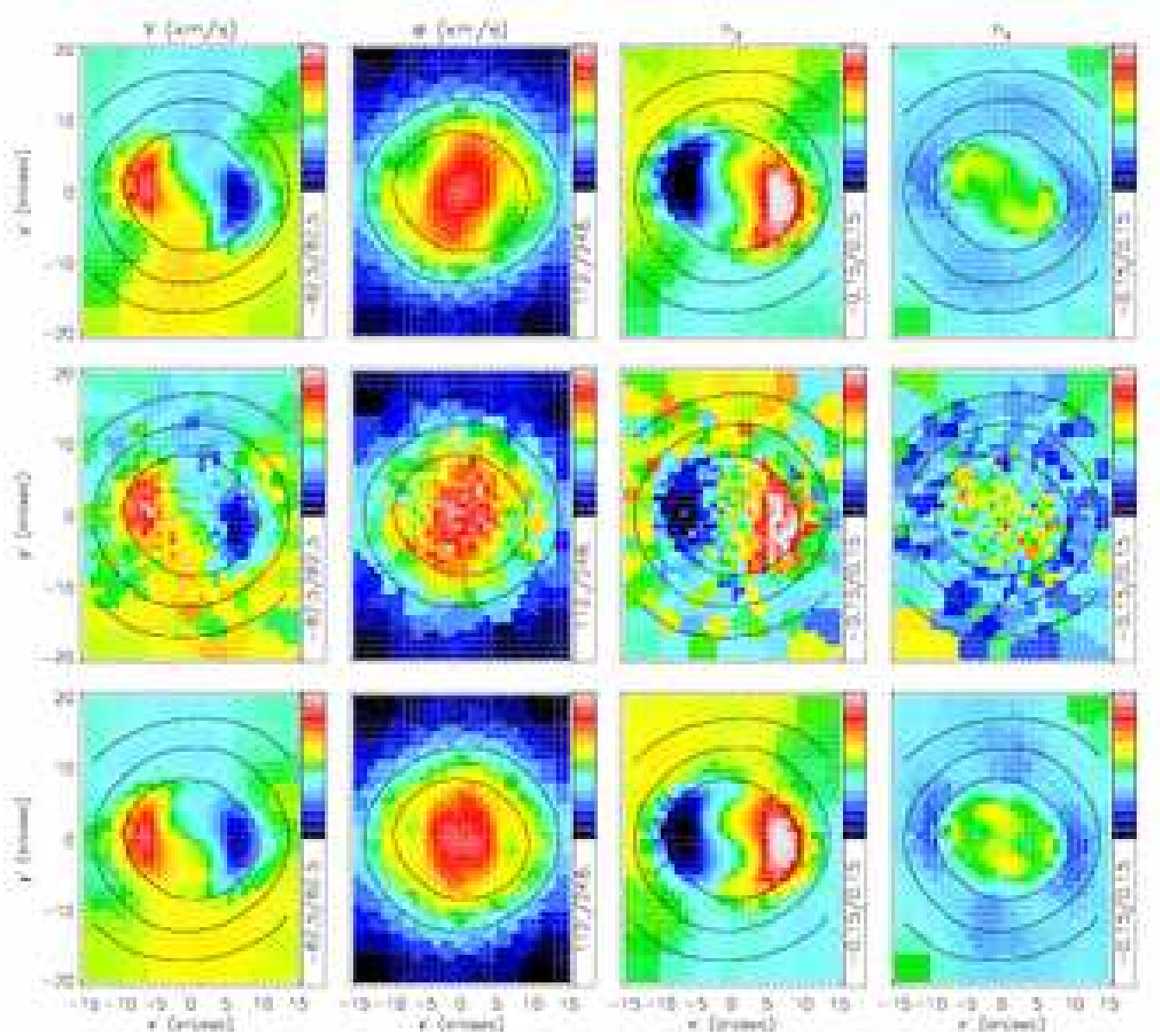


Figure 8. Kinematic maps for a triaxial Abel model (top row) and converted to observables with realistic measurement errors added (middle row; see § 4.3), and for the best-fit triaxial Schwarzschild model (bottom row; see § 5.1). From left to right: mean line-of-sight velocity V and dispersion σ (both in km s^{-1}), and Gauss-Hermite moments h_3 and h_4 . Isophotes of the surface brightness of the Abel model are overplotted in each map. At the right side of each map, the (linear) scale of the corresponding kinematics is indicated by the colour bar, and the limits are given below.

tion. This implies a velocity distribution that becomes increasingly radially anisotropic outwards, but remains close to isotropic in the tangential direction everywhere. This shape and orientation of the velocity ellipsoid in the input Abel model is well reproduced by the best-fit Schwarzschild model, with only a (mild) underestimation of the radial anisotropy towards the z -axis. This is likely the result of numerical difficulties due to the small number of (sampled) long-axis tube orbits that contribute in this region. The absolute difference in the semi-axis lengths σ_+ , σ_- and σ_{yy} of the velocity ellipsoid is on average $\sim 8 \text{ km s}^{-1}$. This uncertainty includes both deviations in shape and orientation of the velocity ellipsoid, and is within the expected range due to the errors in the simulated kinematics. The corresponding axis ratios σ_-/σ_+ and σ_{yy}/σ_+ of the velocity ellipsoid are on average recovered within $\sim 5\%$.

Away from the (x, z) -plane, the average fractional difference in the density between the input Abel model and the best-fit Schwarzschild model stays below 1%. Fig. 10 compares the intrinsic moments of the input triaxial Abel model (top) with those of the best-fit triaxial Schwarzschild model (bottom) in three dimensions. The first column shows the (amplitude) of the streaming motion v_{str} , given by $v_{\text{str}}^2 = v_x^2 + v_y^2 + v_z^2$, and normalised by σ_{RMS} . These quantities are computed on a polar grid (r, θ, ϕ) in the first octant. The (logarithmic) sampling of the radius r is indicated by the black dots between the top and bottom panels, while each row is for a different polar angle θ as indicated on the right, and the colours represent the (linear) change in azimuthal angle ϕ . The limit $\phi = 0^\circ$ (black curves) corresponds to the (x, z) -plane discussed above. The resulting ordered-over-random motion V/σ

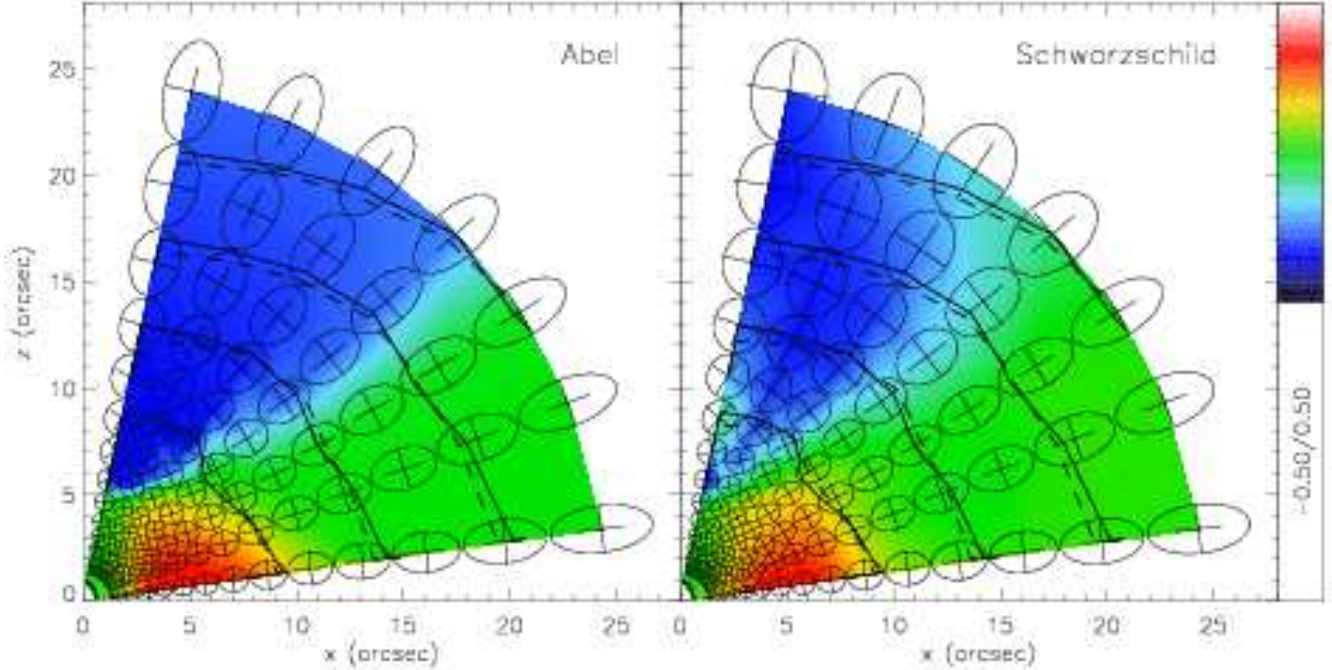


Figure 9. The colours represent the mean motion $\langle v_y \rangle$ perpendicular to the (x, z) -plane, normalised by σ_{RMS} (excluding the axes to avoid numerical problems), for the input triaxial Abel model (left) and for the best-fit triaxial Schwarzschild model (right). The ellipses are cross sections of the velocity ellipsoid with the (x, z) -plane and the crosses represent the (relative) size of the velocity ellipsoid in the perpendicular (y -axis) direction. The black curves are contours of constant mass density in steps of one magnitude, for the input Abel model (solid) and for the fitted Schwarzschild model (dashed). See § 5.3 for details.

is well recovered by the Schwarzschild model, apart from the upper panel, which is likely the result of the above mentioned numerical difficulties close to the z -axis. Overall, the average absolute difference in both v_{str} and σ_{RMS} is below 6 km s^{-1} and the uncertainty in $v_{\text{str}}/\sigma_{\text{RMS}}$ is ~ 0.03 .

The second and third column of Fig. 10 show respectively the intermediate-over-major σ_b/σ_a and minor-over-major σ_c/σ_a axis ratios of the velocity ellipsoid. The velocity ellipsoid of the triaxial Abel model is aligned with the confocal ellipsoidal coordinate system, so that its semi-axis lengths $\sigma_a \geq \sigma_b \geq \sigma_c$ follow directly from $\sigma_\tau^2 = \langle v_\tau^2 \rangle - \langle v_\tau \rangle^2$ with $\tau = \lambda, \mu, \nu$. In general, this is not the case for the triaxial Schwarzschild model, and instead we diagonalize the (symmetric) velocity dispersion tensor with components $\langle \sigma_{st} \rangle$ ($s, t = x, y, z$). As before, the axis ratios of the velocity ellipsoid are quite well recovered by the best-fit Schwarzschild model, except towards the z -axis (upper panels) where it underestimates the anisotropy in the velocity distribution of the input Abel model. Similarly, away from the (x, z) -plane ($\phi = 0^\circ$, black curves), the Schwarzschild model increasingly overestimates the σ_b/σ_a ratio, while the σ_c/σ_a remains well reproduced. It is plausible that the recovery in the (x, z) -plane is better, because it is optimally sampled as starting space for the numerical orbit calculations, and it is crossed perpendicularly by all four major orbit families. Nevertheless, the absolute difference in σ_a , σ_b and σ_c between the input Abel model and the best-fit Schwarzschild model is on average $\sim 9 \text{ km s}^{-1}$. The axis ratios σ_b/σ_a and σ_c/σ_a are on average recovered within $\sim 6\%$.

5.4 Three-integral distribution function

The fitted triaxial Schwarzschild model results in a mass weight γ per orbit. These mass weights are a function of the three integrals of motion (E, I_2, I_3) . In general, only the energy is exact, but for a separable potential I_2 and I_3 are also known explicitly and given by eq. (2.5). The orbital mass weights follow from the DF by integrating $f(E, I_2, I_3)$ over the part of phase-space (\mathbf{x}, \mathbf{v}) that is accessible by the orbit. Since each orbit is a (unique) delta-function in integral-space, the resulting orbital mass weights are in principle zero. However, as described in § 5.1 and § 5.2, final orbits consists each of a bundle of 125 orbits started closely to each other and their assigned mass weights are required to vary smoothly between neighbouring orbits.

To estimate the orbital mass weights from the input triaxial Abel model, we divide the integral-space in finite cells and link each cell to the orbit that corresponds to its centroid. The corresponding mass weights then follow from

$$\gamma(E, I_2, I_3) = \iiint_{\text{cell}} f(E, I_2, I_3) \Delta V(E, I_2, I_3) dE dI_2 dI_3, \quad (5.3)$$

where

$$\Delta V(E, I_2, I_3) = \iiint_{\Omega} \left| \frac{\partial(v_x, v_y, v_z)}{\partial(E, I_2, I_3)} \right| dx dy dz, \quad (5.4)$$

with Ω the volume in configuration space accessible by the orbit. The multi-component DF of the input triaxial Abel model consists of basis functions defined in eq. (2.24), with the DF parameters and weights per component given in § 4.3. Below, we first calculate ΔV and the cell in integral space, and then return to the comparison of the orbital mass weights.

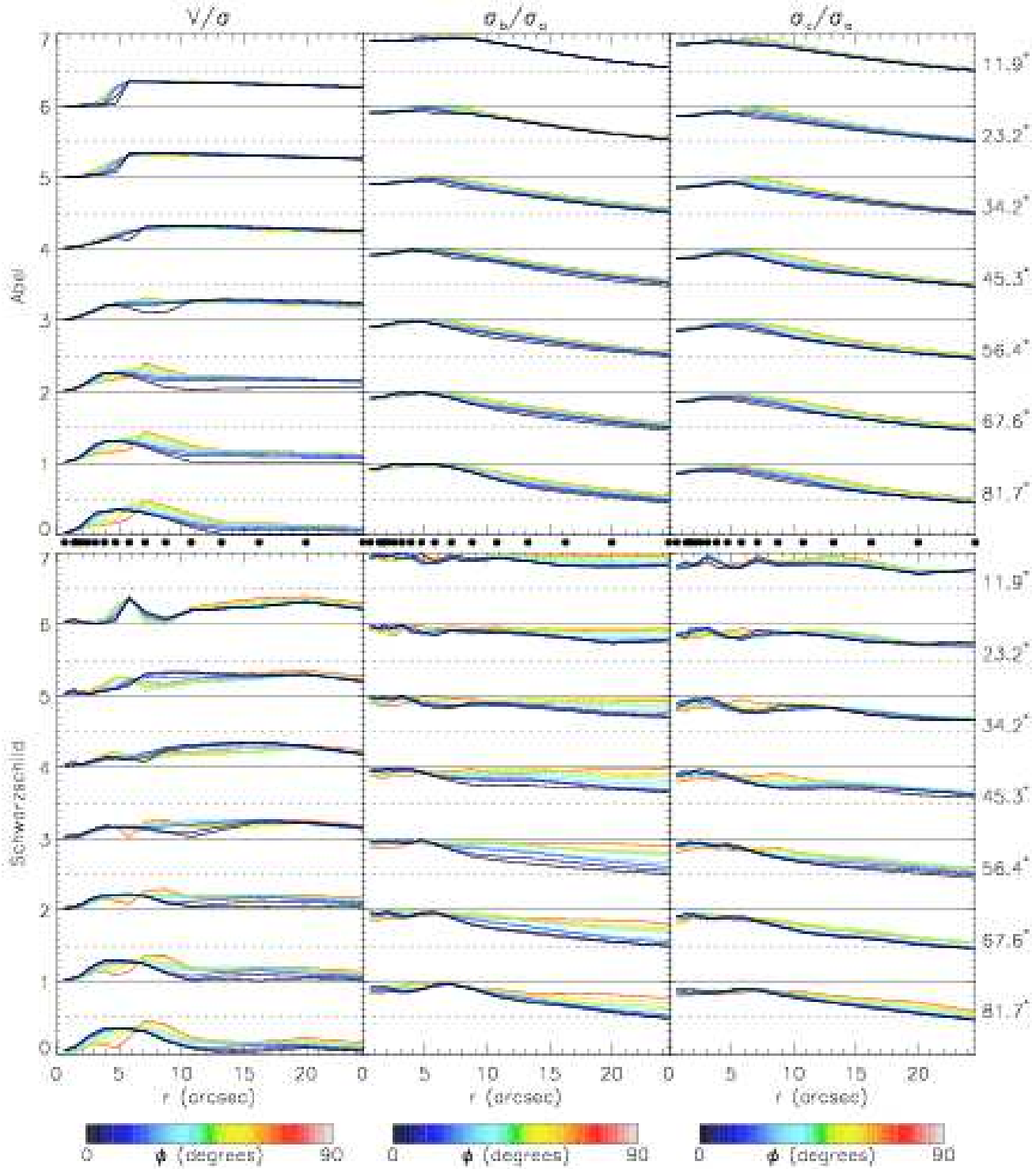


Figure 10. Intrinsic velocity moments in three dimensions for the input triaxial Abel model (top) and for the best-fit triaxial Schwarzschild model (bottom). The first column shows the (amplitude) of the streaming motion v_{str} , normalised by σ_{RMS} . The second and third column show the axis ratios of the velocity ellipsoid, where σ_a , σ_b and σ_c are respectively the semi-lengths of the major, intermediate and minor principal axes. These quantities are computed on a polar grid (r, θ, ϕ) in the first octant. The (logarithmic) sampling of the radius r (in arcsec) is indicated by the black dots between the top and bottom panels. Each row is for a different polar angle θ (in degrees) as indicated on the right, with the top panel close to the z -axis and the bottom panel close to the (x, y) -plane. The colours represent the (linear) change in azimuthal angle ϕ (in degrees), with limits 0° and 90° corresponding to the (x, z) -plane and (y, z) -plane, respectively. See § 5.3 for details.

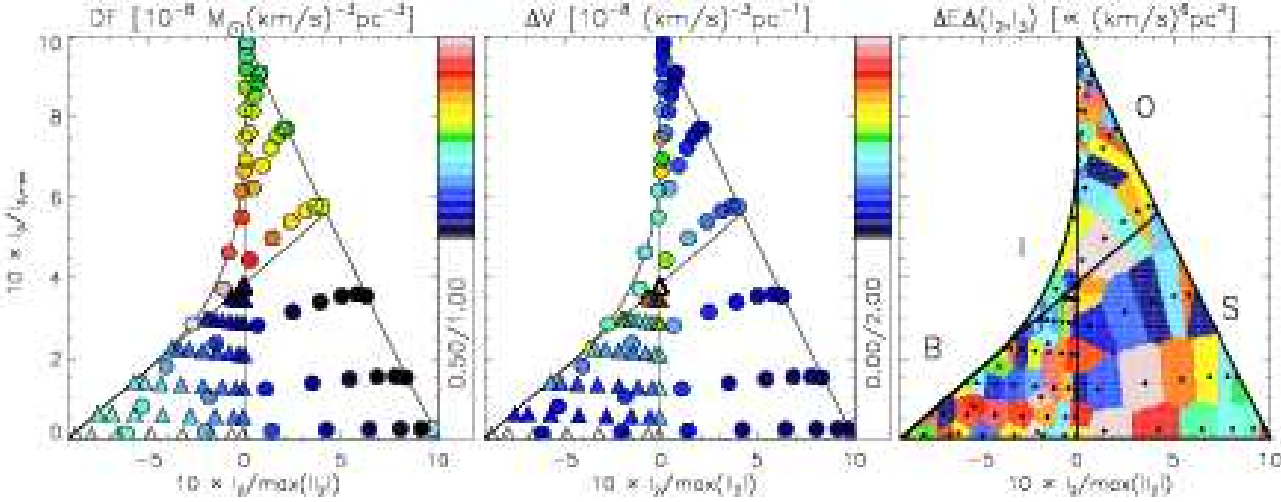


Figure 11. Three quantities involved in the calculation of the orbital mass weights for a triaxial Abel model with an isochrone potential. For a given energy E , in each panel, the values of the second and third integral of motion, I_2 and I_3 , indicated by the symbols, correspond to the orbital starting position and velocities in the triaxial Schwarzschild model that is fitted to the observables of this triaxial Abel model. The solid curves, calculated with the expressions in § 5.4.2, bound and separate the regions of the box (B) orbits, inner (I) and outer (O) long-axis tube orbits and short-axis (S) tube orbits. The circles refer to orbits started in the (x, z) -plane and the triangles represent the additional set of orbits dropped from the equipotential surface (see § 5.1). The latter box orbits may overlap with those started from the (x, z) -plane. The colours in the *left panel* indicate the value of the DF $f(E, I_2, I_3)$ for each orbit in units of $M_\odot (\text{km/s})^{-3} \text{pc}^{-3}$, with the (linear) scale given by the vertical bar on the right. The colours in the *middle panel* represent the values of $\Delta V(E, I_2, I_3)$ defined in eq. (5.4) in units of $(\text{km/s})^{-3} \text{pc}^{-1}$. The area of each Voronoi bin in the *right panel*, multiplied by the range in energy E , approximates the cell $\Delta E \Delta(I_2, I_3)$ in integral space for each orbit. The product of these three quantities yields an estimate of the mass weight $\gamma(E, I_2, I_3)$ for each orbit.

5.4.1 Integral over configuration-space

The expression for $\Delta V(E, I_2, I_3)$ of a single orbit in a triaxial Stäckel potential can be deduced from the relations in § 7.1 of de Zeeuw (1985a). It is given by

$$\Delta V(E, I_2, I_3) = (\gamma - \alpha) \iiint_{\Omega} \frac{(\lambda - \mu)(\mu - \nu)(\nu - \lambda)}{a(\lambda)a(\mu)a(\nu)} \times \sqrt{\frac{8(\lambda + \beta)(\mu + \beta)(\nu + \beta)}{[E - V_{\text{eff}}(\lambda)][E - V_{\text{eff}}(\mu)][E - V_{\text{eff}}(\nu)]}} d\lambda d\mu d\nu, \quad (5.5)$$

where $a(\tau)$, $\tau = \lambda, \mu, \nu$, is defined as

$$a(\tau) = (\tau + \alpha)(\tau + \beta)(\tau + \gamma), \quad (5.6)$$

the effective potential V_{eff} as

$$V_{\text{eff}}(\tau) = \frac{I_2}{\tau + \alpha} + \frac{I_3}{\tau + \gamma} + U[\tau, -\alpha, -\gamma], \quad (5.7)$$

and Ω is the volume in configuration space accessible by the orbit in the triaxial separable potential that obeys (E, I_2, I_3) . The last term in eq. (5.7) is equal to the Stäckel potential (2.3) along the intermediate y -axis.

Because of the separability of the equations of motion, each orbit in a triaxial separable potential can be considered as a sum of three independent motions. Each of these one-dimensional motions is either an oscillation or rotation in one of the three confocal ellipsoidal coordinates (λ, μ, ν) , such that the configuration space volume Ω is bounded by the corresponding coordinate surfaces. The values of (λ, μ, ν) that correspond to these bounding surfaces can be found from Table 1 for the four families of regular orbits: boxes (B), inner (I) and outer (O) long-axis tubes, and short-axis (S) tubes. Whereas α, β and γ are the limits on (λ, μ, ν) set by the foci of the confocal ellipsoidal coordinate system, the other limits are the solutions of $E = V_{\text{eff}}(\tau)$ (see Fig. 7 of de Zeeuw 1985a). In the

case of the triaxial isochrone Stäckel potential (4.2), we can write this equation as a fourth-order polynomial in $\sqrt{\tau}$. The solutions are then the squares of three of the four roots of this polynomial (the fourth root is always negative).

For each orbit in our Schwarzschild model, we compute (E, I_2, I_3) by substituting the starting position and velocities of the orbit into the expressions (2.5). From the value of E and the sign of I_2 (while always $I_3 \geq 0$), we determine to which orbit family it belongs. The corresponding configuration space volume Ω is then given by the boundaries for λ, μ and ν in the last three columns of Table 1. The value of $\Delta V(E, I_2, I_3)$ follows by numerical evaluation of the right-hand side of eq. (5.5).

The integrand in eq. (5.5) contains singularities at the integration limits, which can be easily removed for a triaxial isochrone potential. We write the integrand completely in terms of $(\sqrt{\sigma} \pm \sqrt{\tau})^{1/2}$, where $\sigma, \tau = \lambda, \mu, \nu$ or a constant value. Suppose now that the integral over λ ranges from λ_0 to λ_1 and the terms $(\sqrt{\lambda} - \sqrt{\lambda_0})^{1/2}$ and $(\sqrt{\lambda_1} - \sqrt{\lambda})^{1/2}$ appear in the denominator. The substitution $\sqrt{\lambda} = \sqrt{\lambda_0} + (\sqrt{\lambda_1} - \sqrt{\lambda_0}) \sin^2 \eta$ then removes both singularities since $d\lambda / [(\sqrt{\lambda} - \sqrt{\lambda_0})(\sqrt{\lambda_1} - \sqrt{\lambda})]^{1/2} = 4\sqrt{\lambda} d\eta$.

5.4.2 Cell in integral space

We approximate the triple integration over the cell in integral space in eq. (5.3) by the volume $\Delta E \Delta(I_2, I_3)$. Here ΔE is the (logarithmic) range in E between subsequent sets of orbits at different energies (see § 5.1), with limits given by the central potential and $E = 0$. Because we do not directly sample I_2 and I_3 in our implementation of Schwarzschild's method, as their expressions are in general unknown, we cannot directly calculate the area $\Delta(I_2, I_3)$. Instead, we compute the Voronoi diagram of the points in the (I_2, I_3) -plane that correspond to the starting position and velocities of each orbit, at a given energy E . An example is given in

Table 1. Configuration space volume Ω accessible by the four families of regular orbits.

| orbit | I_2 | E | λ | μ | ν |
|-----------------------------|-------|---|---|---|----------------------------------|
| Box orbits | < 0 | $V_{\text{eff}}(-\beta) \dots 0$ | $-\alpha \dots \lambda_{\text{max}}$ | $-\beta \dots \mu_{\text{max}}$ | $-\gamma \dots \nu_{\text{max}}$ |
| Inner long-axis tube orbits | < 0 | $\min[V_{\text{eff}}(\mu)] \dots V_{\text{eff}}(-\beta)$ | $-\alpha \dots \lambda_{\text{max}}$ | $\mu_{\text{min}} \dots \mu_{\text{max}}$ | $-\gamma \dots -\beta$ |
| Outer long-axis tube orbits | > 0 | $\min[V_{\text{eff}}(\lambda)] \dots V_{\text{eff}}(-\beta)$ | $\lambda_{\text{min}} \dots \lambda_{\text{max}}$ | $\mu_{\text{min}} \dots -\alpha$ | $-\gamma \dots -\beta$ |
| Short-axis tube orbits | > 0 | $\max\{V_{\text{eff}}(-\beta), \min[V_{\text{eff}}(\lambda)]\} \dots 0$ | $\lambda_{\text{min}} \dots \lambda_{\text{max}}$ | $-\beta \dots -\alpha$ | $-\gamma \dots \nu_{\text{max}}$ |

the right panel of Fig. 11. The area of the Voronoi bins approximates the area $\Delta(I_2, I_3)$ for each orbit.

The four families of regular orbits are separated by two lines that follow from $I_2 = 0$ and $E = V_{\text{eff}}(-\beta)$. The latter provides the part of the boundary on I_2 and I_3 for the box orbits. The remainder of this boundary is given by the positivity constraint on I_3 and by the solution of (cf. eqs 64 and 65 of de Zeeuw 1985a)

$$E = V_{\text{eff}}(\kappa_0) \quad \text{and} \quad \left[\frac{dV_{\text{eff}}(\kappa)}{d\kappa} \right]_{\kappa_0} = 0, \quad \kappa_0 \geq -\beta. \quad (5.8)$$

Substituting V_{eff} from eq. (5.7) and using $dU[\tau, -\alpha, -\gamma]/d\tau = U[\tau, \tau, -\alpha, -\gamma]$, we find the solution

$$I_2 = \frac{(\kappa_0 + \alpha)^2}{(\alpha - \gamma)} \left\{ E - U[-\alpha, \kappa_0, \kappa_0] \right\}, \quad (5.9)$$

and similarly for I_3 by interchanging $\alpha \leftrightarrow \gamma$. For $-\beta \leq \kappa_0 \leq -\alpha$, the solution describes the boundary curve for which $I_2 \leq 0$ and corresponds to the thin I tube orbits. For $\kappa_0 \geq -\alpha$, we find the boundary curve for which $I_2 \geq 0$, corresponding to the thin O and S tube orbits.

There are limits on the values of κ_0 depending on the value of E , and sometimes there are no valid solutions for κ_0 , which implies that only box orbits contribute at that energy. These limits can be obtained from the thin orbit curves in the (x, z) -plane. With $y = v_x = v_z = 0$, the expressions (2.5) for the integrals of motion reduce in this plane to

$$\begin{aligned} E &= \frac{1}{2}v_y^2 + U[\lambda, \kappa, -\beta], \\ I_2 &= x^2 \left\{ \frac{1}{2}v_y^2 + (\alpha - \beta)U[\lambda, \kappa, -\beta, -\alpha] \right\}, \\ I_3 &= z^2 \left\{ \frac{1}{2}v_y^2 + (\gamma - \beta)U[\lambda, \kappa, -\beta, -\gamma] \right\}, \end{aligned} \quad (5.10)$$

with $-\gamma \leq \kappa \leq -\alpha$ replacing μ and ν respectively above and below the focal curve given by $z^2/(\gamma - \beta) - x^2/(\beta - \alpha) = 1$. Next, we substitute the expression for E in those for I_2 and I_3 and we use that $(\tau + \beta)U[\lambda, \kappa, \tau, -\beta] = U[\lambda, \kappa, \tau] - U[\lambda, \kappa, -\beta]$, respectively for $\tau = -\alpha$ and $\tau = -\gamma$. We find that the thin orbit curves follow by solving $I_2 = 0$ and thus $E = U[\lambda, \kappa_0, \kappa_0]$ for I tubes, and $I_3 = 0$ and thus $E = U[\kappa_0, \kappa_0, \kappa]$, with $\kappa = \mu$ for O tubes and $\kappa = \nu$ for S tubes. In general these equations have to be solved numerically, but in the case of the triaxial isochrone potential (4.2), they reduce to a second order polynomial in $\sqrt{\kappa_0}$ and the solutions simply follow from the roots of the polynomial.

5.4.3 Orbital mass weight distribution

Once we have computed for each orbit the DF $f(E, I_2, I_3)$, $\Delta V(E, I_2, I_3)$ and the cell $\Delta E \Delta(I_2, I_3)$ in integral space (Fig. 11), its (approximate) mass weight $\gamma(E, I_2, I_3)$ follows by multiplication of these three quantities. As before, the choice of maximum streaming for the (LR and SR) rotating components re-

duces the accessible integral space, and thus also the corresponding orbital mass weights, by a factor two.

The resulting orbital mass weight distribution of the input triaxial Abel model is shown in the top panels of Fig. 12, and that of the fitted triaxial Schwarzschild model in the bottom panels. The energy E increases from left to right, which corresponds to increasing distance from the centre as is indicated by the radius R_E (in arcsec) at the top of each panel. For this representative radius we use the radius of the corresponding thin (S) tube orbit on the x -axis. The values of I_2 and I_3 , on the horizontal and vertical axes respectively, are both normalised with respect to their maximum amplitude at the given energy. In each panel, the mass weight values are normalised with respect to the maximum in that panel. Between the two rows of panels, the fraction of the summed values in each panel with respect to the total mass weight in all panels is given (in %).

The panels with $R_E \lesssim 40''$ are best constrained by the kinematic observables. This takes into account that even orbits that extend beyond the maximum radius covered by the observables can contribute significantly at smaller radii. In these panels, the main features of the orbital mass weight distribution of the triaxial Abel model are recovered. In the outer parts the Schwarzschild model is still constrained by the mass model, which extends to a radius of about $100''$, but the orbital mass weight distribution deviates from that of the input Abel model due to the lack of kinematic constraints. A point-by-point comparison yields an average fractional error of $\sim 50\%$, and if we consider in each panel the mass weights above the mean value, which together contribute more than half of the total mass, the fractional error decreases to $\sim 30\%$. However, this way of quantifying the recovery is (somewhat) misleading since the relatively large fractional errors are at least partially caused by the strong peaks in the orbital mass weight distribution. For example, if in the input Abel model a certain orbit gets a significant weight, but in the Schwarzschild model, due to numerical uncertainties, this weight is assigned to a neighboring orbit with a (slightly) different value of I_3 , the relative error at each of the corresponding points in the integral space can be very large.

Henceforth, we show in Fig. 13 the orbital mass weights as function of each of the three integrals of motion separately by collapsing the cube in (E, I_2, I_3) in the remaining two dimensions. We again use R_E as a representative radius for E (first panel), but since the (range of) values for I_2 and I_3 change with E (see also Fig. 12), we use their index in the cube instead. In addition to the total distribution, we also show the contribution of the three different NR, LR and SR components separately, as well as for the latter two rotating components the contributions from the two directions of rotation by making the mass weights for one of the directions negative. Since the input triaxial Abel model (diamonds connected by solid curves) is constructed with maximum streaming in one of the two directions for both the LR and SR component (see § 4.3), the opposite direction in both cases has zero mass weight. This is nicely reproduced by the best-fit triaxial Schwarzschild model

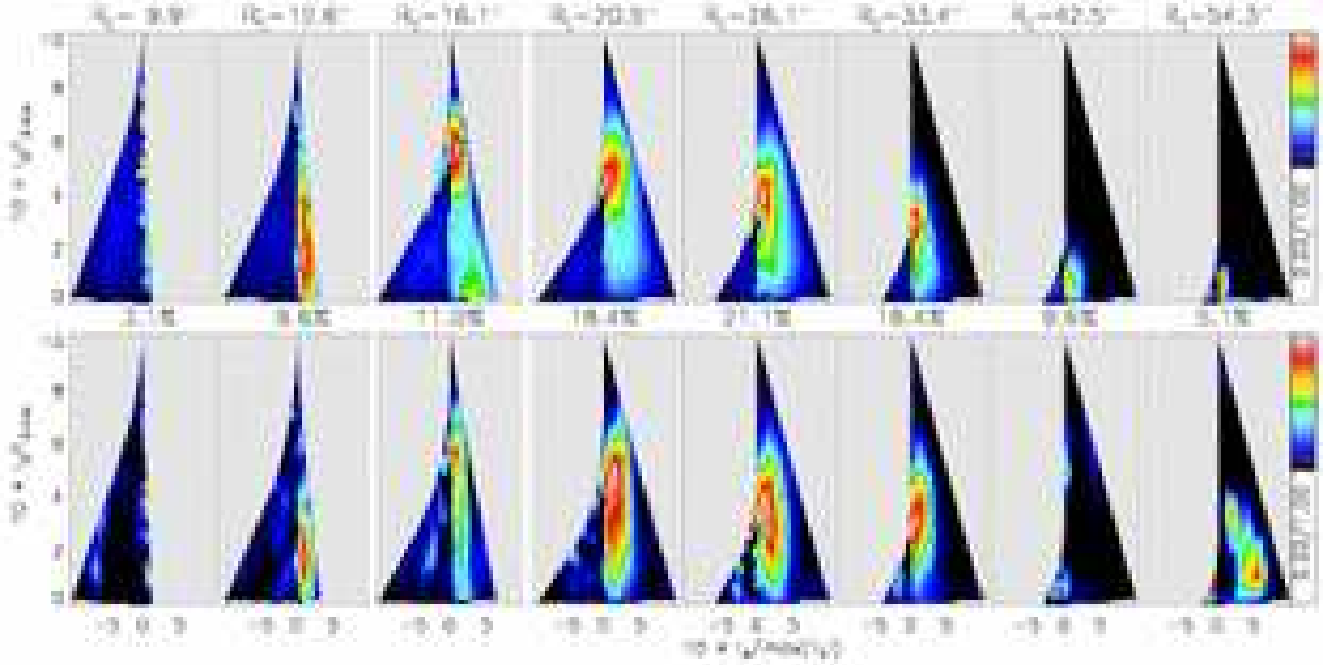


Figure 12. The orbital mass weight distribution for the input triaxial Abel model (top) and for the best-fit triaxial Schwarzschild model (bottom). From left to right the energy increases, corresponding to increasing distance from the centre, indicated by the radius R_E (in arcsec) of the thin short-axis tube orbit on the x -axis. The vertical and horizontal axes represent respectively the second and third integral of motion, I_2 and I_3 , normalised by their maximum amplitude (for given E). In each panel, the colours represent the mass weights, normalised with respect to the maximum in that panel, and with the (linear) scale given by the vertical bars on the right. Between the two rows of panels, the fraction (in %) of the included mass with respect to the total mass is indicated.

(crosses connected by dotted curves) in which $\sim 2\%$ of the total mass, or $\sim 10\%$ of the mass of the LR and SR components, is wrongly assigned to the opposite direction. Keeping in mind that the orbital mass weights itself are not directly fitted and that the typical velocity error of 7.5 km s^{-1} is more than 10% of the maximum in the simulated velocity field (see § 4.3), these percentages are (well) within the expected uncertainties.

From the first panel of Fig. 13, we see that mass as function of E is well recovered, even in the outer parts where (nearly) all the constraints come only from the mass model. The average absolute difference is $\sim 0.7\%$. Whereas for E the constraints provided by the mass model already seem sufficient, for I_2 and I_3 the kinematic constraints are essential. Not surprisingly, we then also see that the recovery is less good with an average absolute difference of $\sim 1.9\%$ in I_2 and $\sim 1.0\%$ in I_3 . The main contribution is from the NR component, while the two rotating components seem to better recovered.

6 AXISYMMETRIC THREE-INTEGRAL GALAXY MODELS

We now consider three-integral galaxy models in the axisymmetric limit. As we have seen in the Introduction (Section 1), various groups have successfully developed independent axisymmetric implementations of Schwarzschild's method and verified their codes in a number of ways. The published tests to recover a known (analytical) input model have been limited to spherical geometry or to an axisymmetric DF that is a function of the two integrals of motion E and L_z only.

Here, we present the velocity moments of the three-integral

Abel DF in the axisymmetric limit and we choose again the isochrone form in eq. (4.1) for the Stäckel potential. The properties of the resulting three-integral Kuzmin-Kutuzov models can be expressed explicitly in cylindrical coordinates. We construct an axisymmetric oblate Abel model and fit Schwarzschild models to the resulting observables to test how well the axisymmetric implementation of Schwarzschild's method, as presented in Cappellari et al. (2006), recovers the intrinsic velocity moments as well as the three-integral DF.

6.1 Velocity moments and line-of-sight velocity distribution

When two of the three constants α , β or γ are equal, the confocal ellipsoidal coordinates (λ, μ, ν) reduce to spheroidal coordinates and the triaxial Stäckel potential (2.3) becomes axisymmetric.

6.1.1 Oblate axisymmetric model

When $\beta = \alpha \neq \gamma$ (triaxiality parameter $T = 0$), we cannot use μ as a coordinate and replace it by the azimuthal angle ϕ , defined as $\tan \phi = y/x$. The relation between (λ, ϕ, ν) and the usual cylindrical coordinates (R, ϕ, z) is given by

$$R^2 = \frac{(\lambda + \alpha)(\nu + \alpha)}{\alpha - \gamma}, \quad z^2 = \frac{(\lambda + \gamma)(\nu + \gamma)}{\gamma - \alpha}. \quad (6.1)$$

The Stäckel potential $V_S(\lambda, \nu) = U[\lambda, -\alpha, \nu]$ is *oblate axisymmetric*. The corresponding integrals of motion follow by substitution of $\mu = -\beta = -\alpha$ in the expressions (2.5), so that the second integral of motion reduces to $I_2 = \frac{1}{2}L_z^2$.

With the choice (2.9) for the DF, the expression for velocity moments $\mu_{lmn}(\lambda, \nu)$ is that of the triaxial case given in

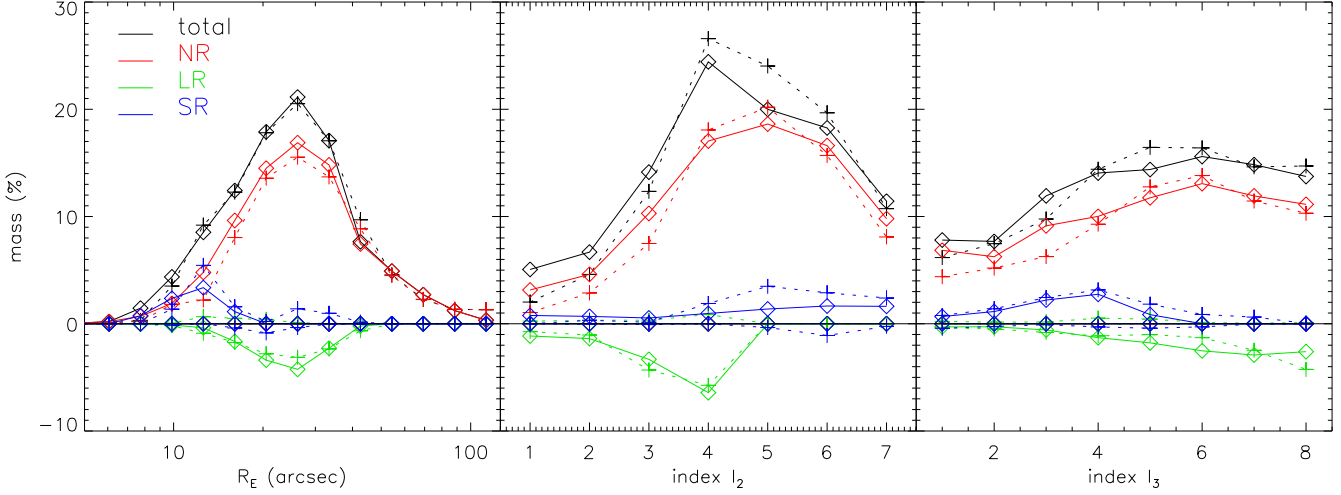


Figure 13. The orbital mass weights (in % of the total mass) for the input triaxial Abel model (diamonds connected by solid curves) and for the best-fit triaxial Schwarzschild model (crosses connected by dotted curves), as function of each of the three integrals of motion. These ‘projections’ of the three-dimensional orbital mass weight distribution shown in Fig. 12 are obtained by collapsing the cube in (E, I_2, I_3) in two dimensions. As before, we represent the energy E in the first panel by the radius R_E (in arcsec) of the thin short-axis tube orbit on the x -axis. For the second and third integral of motion, I_2 and I_3 , we use the index in the cube, since the (range of) their values changes with E . The total distribution (black colour) is split into contributions from the non-rotating (NR; red), long-axis rotating (LR; green) and short-axis rotating (SR; blue) components. Moreover, for each rotating component the contributions from the two directions of rotation are separated by making the mass weights for one of the directions negative.

eq. (2.10), but with $\mu = -\beta = -\alpha$. From Fig. 1, we see that the lower limit on w vanishes. For the NR type of components, $S_{\max} = S_{\text{top}}(\lambda, \mu, -\gamma)$ and the corresponding velocity moments $\mu_{lmn}^{\text{NR}}(\lambda, \nu)$ vanish when either l , m or n is odd. Because the only family of orbits that exists are the short-axis tube orbits, we can introduce net rotation (around the short z -axis) by setting the DF to zero for $L_z < 0$, so that $\mu_{lmn}^{\text{SR}}(\lambda, \nu) = \frac{1}{2}\mu_{lmn}^{\text{NR}}(\lambda, \nu)$. These SR velocity moments vanish when either l or n is odd, but are non-zero if m is odd. They should be multiplied with $(-1)^m$ for maximum streaming in the opposite direction. By choosing different weights for both senses of rotation, we can control the direction and the amount of streaming motion.

In the conversion to observables described in § 3, the matrix \mathbf{Q} , which transforms the velocity components $(v_\lambda, v_\phi, v_\nu)$ to (v_x, v_y, v_z) , reduces to

$$\mathbf{Q} = \begin{pmatrix} A \cos \phi & -\sin \phi & -B \cos \phi \\ A \sin \phi & \cos \phi & -B \sin \phi \\ B & 0 & A \end{pmatrix}, \quad (6.2)$$

where A and B are defined as

$$A^2 = \frac{(\lambda + \gamma)(\nu + \alpha)}{(\lambda - \nu)(\alpha - \gamma)}, \quad B^2 = \frac{(\lambda + \alpha)(\nu + \gamma)}{(\lambda - \nu)(\gamma - \alpha)}. \quad (6.3)$$

Because of the symmetry around the short-axis, the azimuthal viewing angle φ loses its meaning and the misalignment angle $\psi = 0^\circ$. We are left with only the polar viewing angle ϑ , which is commonly referred to as the inclination i , with $i = 0^\circ$ face-on and $i = 90^\circ$ edge-on viewing. As a consequence, the projection matrix \mathbf{P} is a function of i only and follows by substituting $\vartheta = i$ and $\varphi = 0$ in eq. (3.4). The rotation matrix \mathbf{R} in eq. (3.5) reduces to the identity matrix, so that $\mathbf{M} = \mathbf{P}\mathbf{S}\mathbf{Q}$.

The expression for the LOSVD follows from that of the triaxial case in eq. (3.27) by substituting $\mu = -\beta = -\alpha$. For the NR components, again $\Delta\xi'_{\text{NR}} = 2\pi$ and the simplified expression (3.28) holds in case of a DF basis function as defined in eq. (2.24). To introduce net rotation, we require that $(v_\mu =) v_\phi \geq 0$ as in

§ 3.3.4, which yields SR components with maximum streaming. As illustrated in the right panel of Fig. 3, $\Delta\xi'_{\text{SR}}$ is the length of the part of the circle between the intersections $\xi_\pm = 2 \arctan(u_\pm)$ with the line (with u_\pm given in eq. 3.38), and which is on the correct side of the line in eq. (3.37). This is again similar to SR components in the triaxial case, but without the restriction to stay within the ellipses.

6.1.2 Prolate axisymmetric model

When $\beta = \gamma \neq \alpha$ ($T = 1$), we replace the coordinate ν by the angle χ , defined as $\tan \chi = z/y$. The resulting coordinates (λ, μ, χ) follow from the above coordinates (λ, ϕ, ν) by taking $\nu \rightarrow \mu$, $\phi \rightarrow \chi$, and $\gamma \rightarrow \alpha \rightarrow \beta$. The Stäckel potential $V_S(\lambda, \mu) = U[\lambda, \mu, -\gamma]$ is now *prolate axisymmetric*. By substituting $\nu = -\beta = -\gamma$ in eqs (2.5) and (2.10), we obtain the expressions respectively for the integrals of motion (with $I_3 = \frac{1}{2}L_x^2$) and for the intrinsic velocity moments $\mu_{lmn}(\lambda, \mu)$. From Fig. 1, we see that now the upper limit on u vanishes. For the NR components, $S_{\max} = S_{\text{top}}(\lambda, \mu, -\gamma)$, and since we only have the long-axis tube orbits, we can introduce net rotation (around the x -axis) by setting the DF to zero for $L_x < 0$, so that $\mu_{lmn}^{\text{LR}}(\lambda, \mu) = \frac{1}{2}\mu_{lmn}^{\text{NR}}(\lambda, \mu)$. These LR velocity moments vanish if either l or m is odd and multiplication with $(-1)^n$ yields net rotation in the opposite direction.

The matrix \mathbf{Q} , which transforms $(v_\lambda, v_\mu, v_\chi)$ to (v_x, v_y, v_z) , in this case reduces to

$$\mathbf{Q} = \begin{pmatrix} C & -D & 0 \\ D \cos \chi & C \cos \chi & -\sin \chi \\ D \sin \chi & C \sin \chi & \cos \chi \end{pmatrix}, \quad (6.4)$$

where C and D are given by

$$C^2 = \frac{(\lambda + \beta)(\mu + \alpha)}{(\lambda - \mu)(\alpha - \beta)}, \quad D^2 = \frac{(\lambda + \alpha)(\mu + \beta)}{(\lambda - \mu)(\beta - \alpha)}. \quad (6.5)$$

In the projection matrix \mathbf{P} in eq. (3.4), we substitute $\vartheta = \pi/2 - i$ and $\varphi = 0$, so that for inclination $i = 0^\circ$ and $i = 90^\circ$, we are

respectively viewing the prolate mass model end-on and side-on. In the rotation matrix \mathbf{R} we take $\psi = 90^\circ$ to align the projected major axis horizontally. The expression for the LOSVD follows from eq. (3.27) by substituting $\nu = -\beta = -\gamma$, and by requiring $(v_\nu =) v_\chi \geq 0$ we obtain LR components with maximum streaming. As for the oblate case and illustrated in the left panel of Fig. 3, $\Delta\xi'_{\text{SR}}$ is the length of the circle part between the angles $\xi_\pm = 2 \arctan(u_\pm)$ (with u_\pm given in eq. 3.34) which is on the correct side of the line in eq. (3.32).

6.2 Kuzmin-Kutuzov potential

In the axisymmetric limit, the form (4.1) for $U(\tau)$ results in the Kuzmin-Kutuzov (1962) potential. We give the properties relevant for our analysis, while further details can be found in Dejonghe & de Zeeuw (1988), including expressions and plots of the mass density ρ_S , its axis ratios, and the two-integral DF $f(E, L_z^2)$ consistent with ρ_S [see also Batsleer & Dejonghe (1993), who also corrected a typographical error in $f(E, L_z^2)$].

When $\beta = \alpha$, the oblate axisymmetric potential $V_S(\lambda, \nu) = U[\lambda, -\alpha, \nu]$ and the third order divided difference $U[\lambda, -\alpha, \nu, \sigma]$, which both appear in the expressions for the integral of motions (2.5), have the simple forms

$$V_S(\lambda, \nu) = \frac{-GM}{\sqrt{\lambda} + \sqrt{\nu}}, \quad (6.6)$$

$$U[\lambda, -\alpha, \nu, \sigma] = \frac{GM}{(\sqrt{\lambda} + \sqrt{\nu})(\sqrt{\lambda} + \sqrt{\sigma})(\sqrt{\nu} + \sqrt{\sigma})}, \quad (6.7)$$

where again $GM = \sqrt{-\gamma} + \sqrt{-\alpha}$, so that $V_S = -1$ in the centre. By means of the relations

$$\lambda + \nu = R^2 + z^2 - \alpha - \gamma, \quad \lambda\nu = \alpha\gamma - \gamma R^2 - \alpha z^2, \quad (6.8)$$

and $(\sqrt{\lambda} + \sqrt{\nu})^2 = \lambda + \nu + 2\sqrt{\lambda\nu}$ and $(\sqrt{\lambda} + \sqrt{\sigma})(\sqrt{\nu} + \sqrt{\sigma}) = \sqrt{\lambda\nu} + \sqrt{\sigma}(\sqrt{\lambda} + \sqrt{\nu}) + \sigma$, we can write the potential and integrals of motion explicitly as elementary expressions in the usual cylindrical coordinates.

When $\beta = \gamma$, the prolate potential $V_S(\lambda, \mu) = U[\lambda, \mu, -\gamma]$ and the third order divided difference $U[\lambda, \mu, -\gamma, \sigma]$ follow respectively from (6.6) and (6.7) by replacing ν by μ .

6.3 An axisymmetric Abel model

The above constructed triaxial Abel model (§ 4.3) transforms into an oblate axisymmetric Abel model if we let ζ approach unity, while keeping $\xi = 0.64$ fixed. Similar to the triaxial case, the DF contains a NR component with the same parameters, $u = w = -0.5/(-\alpha)$ and $\delta = 1$, but we exclude the LR component since long-axis tube orbits do not exist in an oblate axisymmetric galaxy. We include two SR components, one with the same parameters as the NR component, and for the other we set $w = 0.5/(-\alpha)$ and $u = -1.0/(-\alpha)$, and we choose the sense of rotation in the opposite direction. The latter implies a compact counter-rotating component, which is clearly visible in the kinematic maps shown in the top panels of Fig. 14. The inclination is the same value as the polar angle ϑ for the triaxial Abel model, i.e. $i = 70^\circ$, and the mass fractions of the three DF components are respectively 20%, 60% and 20%. Due to axisymmetry, all maps of the even (odd) velocity moments are bi-(anti)-symmetric and the velocity field shows a straight zero-velocity curve. The signatures of the counter-rotation are similar in the velocity field and h_3 (but anti-correlated), and result in a decrease of σ and an increase of h_4 in the centre.

6.4 Recovery of axisymmetric three-integral models

We now describe the application of our axisymmetric implementation of Schwarzschild's method to the observables of the oblate axisymmetric Abel model of § 6.3, while highlighting the differences with the application in triaxial geometry described in Section 5.

6.4.1 Axisymmetric Schwarzschild model fit to observables of an oblate axisymmetric Abel model

We use the implementation of Schwarzschild's method in axisymmetric geometry that is described in detail in Cappellari et al. (2006). The main differences with respect to our triaxial implementation are certain simplifications due to the extra symmetry. There are no twists in the surface brightness and of the four families of regular orbits only the short-axis tube orbits are supported. We use the same set-up as in the triaxial case, but since there are no box orbits, the additional dropping of orbits from the equipotential surface is not needed.

Fig. 14 shows that the (simulated) observables of the oblate axisymmetric Abel model (top panels) are very well matched by the best-fit axisymmetric Schwarzschild model (bottom panels). The kinematics of the main body as well as the signatures of the counter-rotating core are accurately fitted within the (added) noise.

6.4.2 Intrinsic velocity moments

It is convenient to analyse the intrinsic velocity moments of (oblate) axisymmetric models in cylindrical coordinates (R, ϕ, z) . Because of axisymmetry the models are independent of the azimuthal angle ϕ , and it is sufficient to consider the meridional (R, z) -plane. The analysis of the intrinsic velocity moments in the (R, z) -plane is similar to that for the triaxial case in the (x, z) -plane (§ 5.3). In this case, the mean azimuthal rotation $\langle v_\phi \rangle$, perpendicular to the meridional plane, is the only non-vanishing first-order velocity moment. In Fig. 15, we compare the values of $\langle v_\phi \rangle / \sigma_{\text{RMS}}$, indicated by the colours, for the Abel model (left panel) with those for the fitted Schwarzschild model (right panel). The root-mean-square velocity dispersion σ_{RMS} is defined as $\sigma_{\text{RMS}}^2 = (\sigma_R^2 + \sigma_\phi^2 + \sigma_z^2)/3$. The azimuthal axis of the velocity ellipsoid, with semi-axis length σ_ϕ defined as $\sigma_\phi^2 = \langle v_\phi^2 \rangle - \langle v_\phi \rangle^2$, is perpendicular to the meridional plane. The cross sections with the meridional plane are indicated by the ellipses in Fig. 15, where the semi-axis lengths follow from (5.1) by replacing (x, z) with (R, z) .

As in the triaxial case the density (solid curve) is well fitted by the axisymmetric Schwarzschild model (dashed curve). The Abel model shows a strong gradient in $\langle v_\phi \rangle / \sigma_{\text{RMS}}$, which is correctly recovered by the axisymmetric Schwarzschild model. The absolute difference is on average less than 0.06, except near the symmetry z -axis. This is likely the result of numerical difficulties due to the small number of (sampled) short-axis tube orbits that contribute in this region. The shape and orientation of the ellipses are nearly identical, indicating that the anisotropic velocity distribution of the Abel model is reproduced within the expected uncertainties due to the errors in the simulated kinematics. The axis ratios σ_- / σ_+ and σ_ϕ / σ_+ of the velocity ellipsoid are on average recovered within $\sim 5\%$.

6.4.3 Three-integral distribution function

In the oblate axisymmetric case, all (regular) orbits are short-axis tube orbits with $I_2 = \frac{1}{2}L_z^2$ and energy E ranging from

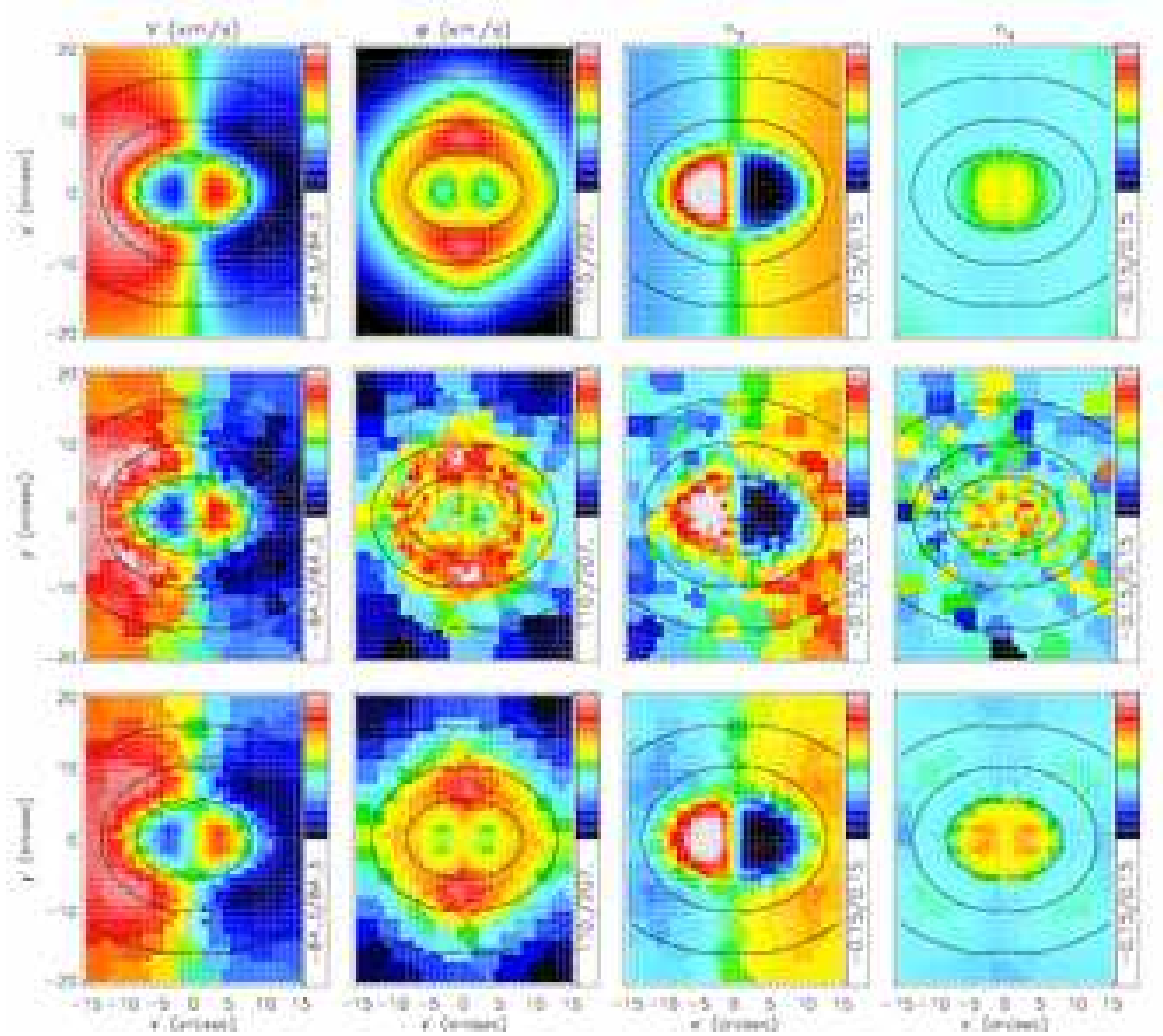


Figure 14. Kinematic maps for an oblate axisymmetric Abel model (top row) and converted to observables with realistic measurement errors added (middle row; see § 6.3) and for the fitted axisymmetric Schwarzschild model (bottom row; see § 6.4). Parameters and colour scale are as in Fig. 8.

$\min [V_{\text{eff}}(\lambda)]$ to zero. The expression for ΔV in eq. (5.5) reduces to

$$\Delta V(E, L_z, I_3) = \frac{4\pi}{|L_z|} \int_{-\gamma}^{\nu_{\max}} \int_{\lambda_{\min}}^{\lambda_{\max}} \frac{(\nu - \lambda)}{(\lambda + \alpha)(\lambda + \gamma)(\nu + \alpha)(\nu + \gamma)} \times \sqrt{\frac{(\lambda + \alpha)(\nu + \alpha)}{[E - V_{\text{eff}}(\lambda)][E - V_{\text{eff}}(\nu)]}} d\lambda d\nu \quad (6.9)$$

where as before ν_{\max} , λ_{\min} and λ_{\max} are the solutions of $E = V_{\text{eff}}(\tau)$ (see Fig. 23 of de Zeeuw 1985a). The factor in front of the double integral includes the factor 2π from the integration over the azimuthal angle ϕ .

In Fig. 16, we compare the orbital mass weight distribution of the input oblate Abel model (top panels), with that of the best-fit axisymmetric Schwarzschild model (bottom panels). The three-

integral mass weight distributions are quite similar, even in the panels with a relatively low mass content. The average fractional error is $\sim 30\%$, and if we consider in each panel the mass weights above the mean value, which together contribute more than half of the total mass, the fractional error decreases to around $\sim 20\%$. Because of possible strong point-to-point fluctuations as discussed in § 5.4.3, we also show in Fig. 17 the orbital mass distribution as function of each of the three integrals of motion separately by collapsing the cube in (E, I_2, I_3) in the remaining two dimensions. Besides the total distribution, we show separately the contributions from the NR component and the two opposite rotating SR components in the input oblate Abel model (see § 6.3). While the compact counter-rotating SR component (blue) is nicely reproduced by the best-fit axisymmetric Schwarzschild model, the mass assigned to the main SR component is too high ($\sim 10\%$ of the total mass), which also results in an underestimation of the NR component. This

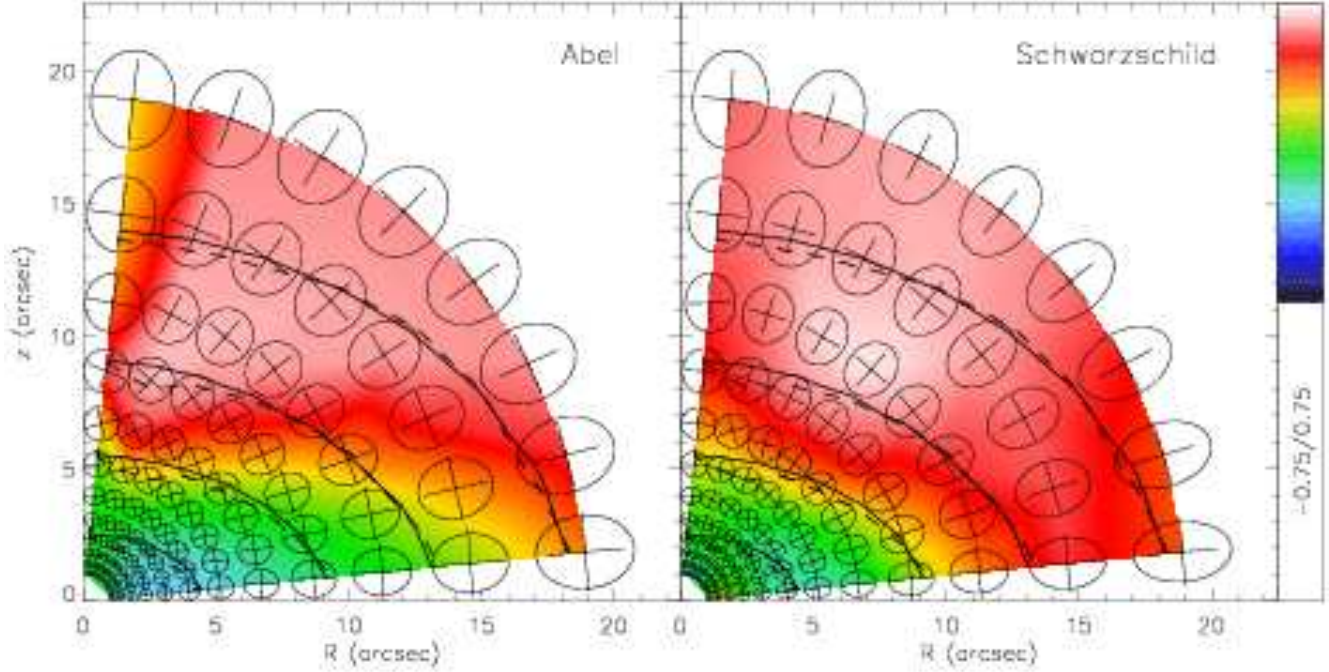


Figure 15. The mean azimuthal motion (v_ϕ) perpendicular to the meridional plane, normalised by σ_{RMS} , for an oblate axisymmetric Abel model (left) and for the best-fit axisymmetric Schwarzschild model (right). Parameters as in Fig. 9.

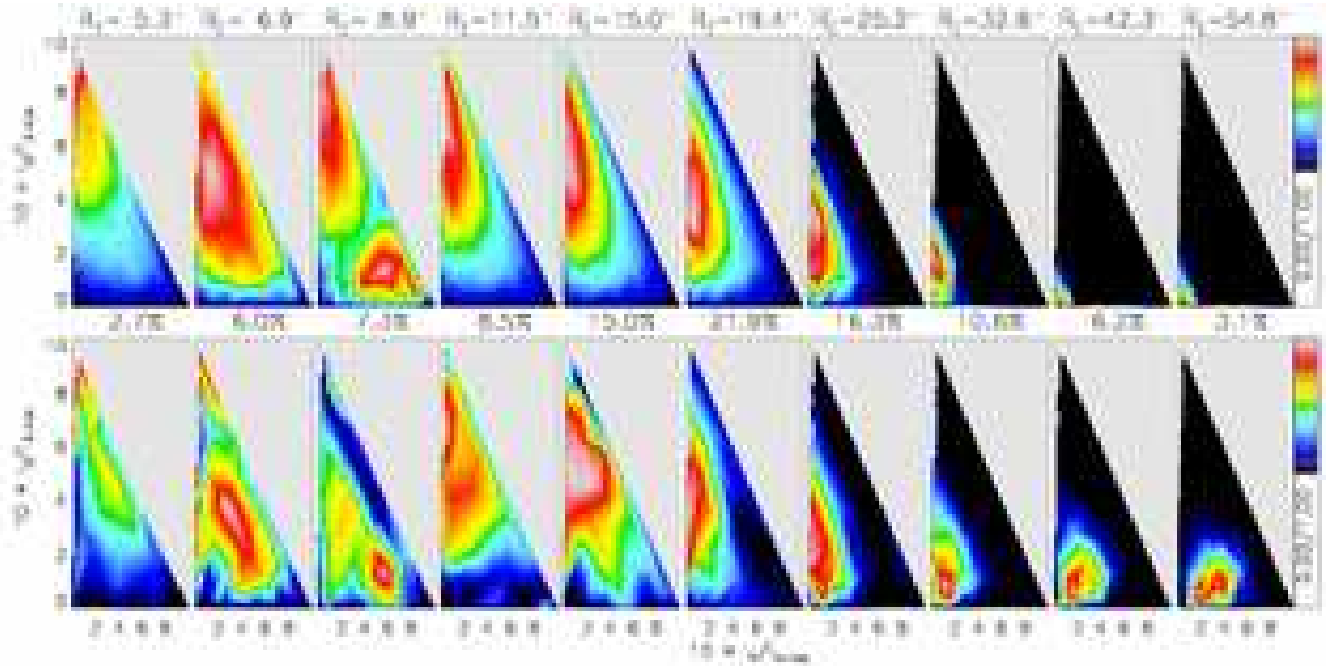


Figure 16. The mass weight distribution for the input oblate Abel model (top) and for the best-fit axisymmetric Schwarzschild model (bottom). Parameters as in Fig. 12. The second integral of motion $I_2 = \frac{1}{2}L_z^2 \geq 0$, where L_z is the component of the angular momentum parallel to the symmetry z -axis.

is reflected in the average absolute difference in mass as function of E , which is $\sim 1.3\%$. As for the triaxial case, the recovery for I_2 and I_3 is less good with average uncertainties of $\sim 2.1\%$ and $\sim 2.4\%$, respectively.

A similar good recovery was found by Krajnović et al. (2005)

for the case of a two-integral DF $f(E, L_z)$, which implies an isotropic velocity distribution in the meridional plane. Thomas et al. (2004) showed that their independent axisymmetric numerical implementation of Schwarzschild's method is similarly able to recover an analytical $f(E, L_z)$. Our results show that the orbital

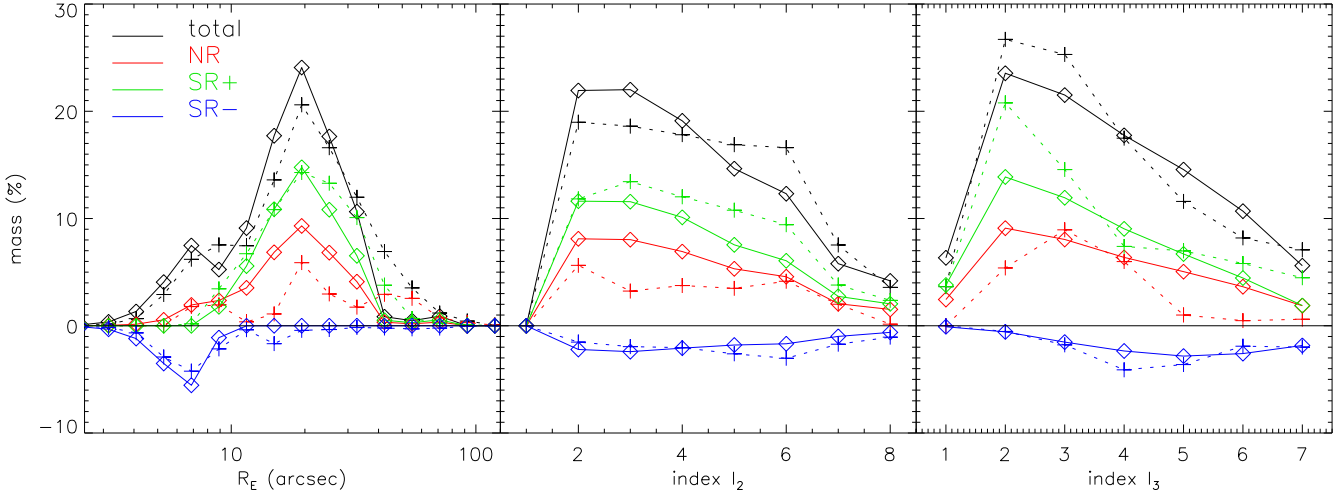


Figure 17. The orbital mass weights for the input oblate Abel model (diamonds connected by solid curves) and for the best-fit axisymmetric Schwarzschild model (crosses connected by dotted curves). The parameters are as in Fig. 13, except that rotation can only come from short-axis rotating (SR) components, for which the two directions of rotation are indicated separately.

mass weight distribution that follows from a fully three-integral DF $f(E, L_z, I_3)$ can be recovered as well.

7 DISCUSSION AND CONCLUSIONS

We have extended the Abel models introduced by DL91 and generalised by MD99, and shown that, in addition to the intrinsic velocity moments, the full LOSVD of these models can be calculated in a straightforward way. We have then used the Abel models to construct realistic axisymmetric and triaxial galaxy models to test the accuracy of Schwarzschild’s orbit superposition method.

Although Abel models have separable potentials with a central core and assume a specific functional form for the (three-integral) DF, they display a large range of shapes and their observables, which can be calculated easily, include many of the features seen in the kinematic maps of early-type galaxies. We have used an isochrone Stäckel potential that in the axisymmetric limit reduces to the Kuzmin-Kutuzov model and becomes Hénon’s isochrone in the spherical limit. Because of the simple form of the isochrone potential, the resulting Abel models are ideally suited to test numerical implementations of the Schwarzschild orbit superposition method. The calculation of ΔV , needed when comparing the orbital mass weight distribution of the Schwarzschild models with the three-integral DF of the Abel models, simplifies significantly for this case.

Integral-field observations in principle provide the LOSVD as a function of position on the sky, so that it is a function $\mathcal{L}(x', y', v_{z'})$ that depends on three variables. The oblate axisymmetric and triaxial galaxy models we have constructed, have a DF which is a sum of Abel components $f(S) = f(-E + wI_2 + uI_3)$ with different values of the parameters w and u , so that the DF is a function of three variables as well, namely the integrals of motion E , I_2 and I_3 . We have shown that the simulated integral-field observables of these models are matched in detail by the best-fit Schwarzschild model. This does not automatically imply that the intrinsic velocity moments and the three-integral DF — which are not directly fitted — are also correctly recovered.

First consider three-integral oblate models, i.e., with a DF that

is a function $f(E, L_z, I_3)$. In the special case that a galaxy happens to be well approximated by a two-integral DF $f(E, L_z)$, the density $\rho(R, z)$ uniquely determines the even part of $f(E, L_z)$ and the mean streaming $\rho\langle v_\phi \rangle$ in the meridional plane fixes the part of $f(E, L_z)$ that is odd in L_z (Dejonghe 1986). Ignoring non-uniqueness in the deprojection of the surface density Σ (Rybicki 1987) and the mean streaming motion V on the plane of the sky, these two quantities define a two-integral DF completely. The observed velocity dispersion and higher-order velocity moments of the LOSVD then provide additional information, which for example can be used to constrain the inclination (e.g., Cappellari et al. 2006). However, the reliability of the derived inclination, of course, depends on the correctness of the assumption of a two-integral DF. In the more realistic case of a three-integral DF $f(E, L_z, I_3)$, such a one-to-one relation with (the velocity moments of) the observed LOSVD $\mathcal{L}(x', y', v_{z'})$ has not been established. Nevertheless, we showed that, given integral-field observations of the velocity moments of the LOSVD (up to h_4), recovery of the full three-integral DF is possible with Schwarzschild’s method, for the correct inclination and mass-to-light ratio.

In the triaxial case, the DF is again a function of three integrals of motion, but the orbital structure in these models is substantially richer than in the oblate axisymmetric models, with four major orbit families, instead of only one. This introduces a fundamental non-uniqueness in the recovery of the DF. Whereas in the oblate axisymmetric case $\rho(R, z)$ uniquely defines the even part of $f(E, L_z)$, in the (separable) triaxial case the density $\rho(x, y, z)$ does *not* uniquely determine the even part of $f(E, I_2, I_3)$, although both of these are functions of three variables (Hunter & de Zeeuw 1992). It is (yet) unknown how much specification of $\mathcal{L}(x', y', v_{z'})$ can narrow down the range of possible DFs further, even ignoring the non-uniqueness caused by the required deprojection of the surface brightness. Our results show that Schwarzschild’s method recovers the correct orbital mass weight distribution associated to $f(E, I_2, I_3)$. Given the very large freedom in the orbit choice for this case, the modest resolution of our orbit library, and the resulting approximations in the evaluation of the phase space volume, the agreement between the orbital mass weights found in § 5.4 is in fact remarkable. It may be possible to improve the DF recovery

further by refining the sampling of the orbits and the regularisation of the orbital mass weights.

Our analysis shows that it is clear that Abel models are useful for testing orbit-based modelling methods such as Schwarzschild's method. In particular the oblate limiting case with a Kuzmin-Kutuzov potential (§ 6.4) provides a new and convenient test for existing axisymmetric Schwarzschild codes. Furthermore, because Abel models with a few DF components can already provide quite a good representation of observed early-type galaxies, they can be used as a way to (numerically) build three-integral dynamical models of these galaxies (see e.g. MD96 for an application to Centaurus A).

We conclude that Schwarzschild's method is able to recover the internal dynamical structure of realistic models of early-type galaxies. We show in vdB07 that Schwarzschild's method also allows for an accurate determination of the mass-to-light ratio and provides significant constraints on the viewing direction and intrinsic shape. The axisymmetric Schwarzschild method has already been successfully applied by us and other groups to determine the black hole mass, mass-to-light ratio (profile), dark matter profile as well as the (three-integral) DF of early-type galaxies. With our extension to triaxial geometry, described in detail in vdB07, we are now able to model early-type galaxies — in particular the giant ellipticals — which show clear signatures of non-axisymmetry, including isophote twist, kinematic misalignment and kinematic decoupled components. Moreover, since triaxial galaxies may appear axisymmetric (or even spherical) in projection, we can investigate the effect of intrinsic triaxiality on the measurements of e.g. black hole masses based on axisymmetric model fits to observations of galaxies. Work along these lines is in progress.

ACKNOWLEDGEMENTS

We sincerely thank the referee for constructive comments and suggestions that improved the presentation, and Michele Cappellari and Anne-Marie Weijmans for a careful reading of an earlier version of the manuscript. GvdV acknowledges support provided by NASA through grant NNG04GL47G and through Hubble Fellowship grant HST-HF-01202.01-A awarded by the Space Telescope Science Institute, which is operated by the Association of Universities for Research in Astronomy, Inc., for NASA, under contract NAS 5-26555. RvdB acknowledges support by the Netherlands Organization for Scientific Research (NWO) through grant 614.000.301.

REFERENCES

- Andrews D. F., Bickel P. J., Hampel F. R., Rogers W., Tukey J., 1972, *Robust Estimates of Locations: Survey and Advances*. Princeton University, Princeton
- Arnold R., 1990, *MNRAS*, 244, 465
- Arnold R., de Zeeuw P. T., Hunter C., 1994, *MNRAS*, 271, 924
- Bacon R., et al. 2001, *MNRAS*, 326, 23
- Batsleer P., Dejonghe H., 1993, *A&A*, 271, 104
- Batsleer P., Dejonghe H., 1994, *A&A*, 287, 43
- Beers T. C., Flynn K., Gebhardt K., 1990, *AJ*, 100, 32
- Binney J., 1982, *MNRAS*, 201, 15
- Blinnikov S., Moessner R., 1998, *A&AS*, 130, 193
- Camm G. L., 1941, *MNRAS*, 101, 195
- Cappellari M., 2002, *MNRAS*, 333, 400
- Cappellari M., Bacon R., Bureau M., Damen M. C., Davies R. L., de Zeeuw P. T., Emsellem E., Falcón-Barroso J., Krajnović D., Kuntschner H., McDermid R. M., Peletier R. F., Sarzi M., van den Bosch R. C. E., van de Ven G., 2006, *MNRAS*, 366, 1126
- Cappellari M., Copin Y., 2003, *MNRAS*, 342, 345
- Cappellari M., Verolme E. K., van der Marel R. P., Verdoes Kleijn G. A., Illingworth G. D., Franx M., Carollo C. M., de Zeeuw P. T., 2002, *ApJ*, 578, 787
- Carlson B. C., 1977, *Special Functions of Applied Mathematics*. Academic Press, New York San Francisco London
- Carollo C. M., de Zeeuw P. T., van der Marel R. P., 1995, *MNRAS*, 276, 1131
- Chandrasekhar S., 1940, *ApJ*, 92, 441
- Copin Y., Cretton N., Emsellem E., 2004, *A&A*, 415, 889
- Cretton N., de Zeeuw P. T., van der Marel R. P., Rix H., 1999, *ApJS*, 124, 383
- Cretton N., Emsellem E., 2004, *MNRAS*, 347, L31
- Cretton N., Rix H.-W., de Zeeuw P. T., 2000, *ApJ*, 536, 319
- Cretton N., van den Bosch F. C., 1999, *ApJ*, 514, 704
- de Zeeuw P. T., 1985a, *MNRAS*, 216, 273
- de Zeeuw P. T., 1985b, *MNRAS*, 216, 599
- de Zeeuw P. T., Franx M., 1989, *ApJ*, 343, 617
- de Zeeuw P. T., Hunter C., Schwarzschild M., 1987, *ApJ*, 317, 607
- de Zeeuw P. T., Lynden-Bell D., 1985, *MNRAS*, 215, 713
- de Zeeuw P. T., Peletier R., Franx M., 1986, *MNRAS*, 221, 1001
- de Zeeuw P. T., Pfenniger D., 1988, *MNRAS*, 235, 949
- Dejonghe H., 1986, *Phys. Rep.*, 133, 217
- Dejonghe H., de Zeeuw P. T., 1988, *ApJ*, 333, 90
- Dejonghe H., Laurent D., 1991, *MNRAS*, 252, 606 [DL91]
- Eddington A. S., 1915, *MNRAS*, 76, 37
- Eddington A. S., 1916, *MNRAS*, 76, 572
- Edgeworth F. Y., 1905, *Cambridge Philos. Soc.*, 20, 36
- Emsellem E., et al. 2004, *MNRAS*, 352, 721
- Evans N. W., de Zeeuw P. T., 1992, *MNRAS*, 257, 152
- Franx M., 1988, *MNRAS*, 231, 285
- Gebhardt K., et al. 2000, *AJ*, 119, 1157
- Gebhardt K., et al. 2003, *ApJ*, 583, 92
- Gerhard O. E., 1993, *MNRAS*, 265, 213
- Gradshteyn I. S., Ryzhik I. M., 1994, *Table of Integrals, Series and Products*. Academic Press, San Diego
- Henon M., 1959, *Annales d'Astrophysique*, 22, 126
- Hunter C., de Zeeuw P. T., 1992, *ApJ*, 389, 79
- Jeans J. H., 1915, *MNRAS*, 76, 70
- Kauffmann G., van den Bosch F., 2002, *Scientific American*, 286, 36
- Krajnović D., Cappellari M., Emsellem E., McDermid R. M., de Zeeuw P. T., 2005, *MNRAS*, 357, 1113
- Kuzmin G. G., 1973, in *Proc. All-Union Conf., Dynamics of Galaxies and Clusters*. ed. T. B. Omarov (Alma Ata: Akad. Nauk Kazakhskoj SSR), 71 (English transl. in *IAU Symp. 127, Structure and Dynamics of Ell. Galaxies*, ed. P.T. de Zeeuw [Dordrecht: Reidel], 553)
- Kuzmin G. G., Kutuzov S. A., 1962, *Bull. Abastumani Astroph. Obs.*, 27, 82
- Lynden-Bell D., 1962, *MNRAS*, 124, 1
- Mathieu A., Dejonghe H., 1996, *A&A*, 314, 25
- Mathieu A., Dejonghe H., 1999, *MNRAS*, 303, 455 [MD99]
- Mathieu A., Dejonghe H., Hui X., 1996, *A&A*, 309, 30
- Merritt D., 1985, *AJ*, 90, 1027
- Navarro J. F., Frenk C. S., White S. D. M., 1997, *ApJ*, 490, 493
- Osipkov L. P., 1979, *Pis'ma v Astronomicheskii Zhurnal*, 5, 77
- Pfenniger D., 1984, *A&A*, 134, 373

- Primack J. R., 2004, in IAU Symp. 220: Dark Matter in Galaxies, eds. S. D. Ryder, D. J. Pisano, M. A. Walker, and K. C. Freeman, p. 53
- Richstone D. O., Tremaine S., 1984, *ApJ*, 286, 27
- Rix H., de Zeeuw P. T., Cretton N., van der Marel R. P., Carollo C. M., 1997, *ApJ*, 488, 702
- Rybicki G. B., 1987, in IAU Symp. 127: Structure and Dynamics of Elliptical Galaxies, ed. P. T. de Zeeuw, p. 397
- Schwarzschild M., 1979, *ApJ*, 232, 236
- Schwarzschild M., 1982, *ApJ*, 263, 599
- Schwarzschild M., 1993, *ApJ*, 409, 563
- Statler T. S., 1987, *ApJ*, 321, 113
- Statler T. S., 1991, *AJ*, 102, 882
- Statler T. S., 1994, *ApJ*, 425, 458
- Teuben P., 1987, *MNRAS*, 227, 815
- Thomas J., Saglia R. P., Bender R., Thomas D., Gebhardt K., Magorrian J., Corsini E. M., Wegner G., 2005, *MNRAS*, 360, 1355
- Thomas J., Saglia R. P., Bender R., Thomas D., Gebhardt K., Magorrian J., Richstone D., 2004, *MNRAS*, 353, 391
- Valluri M., Merritt D., Emsellem E., 2004, *ApJ*, 602, 66
- van Albada T. S., Bahcall J. N., Begeman K., Sancisi R., 1985, *ApJ*, 295, 305
- van de Ven G., Hunter C., Verolme E. K., de Zeeuw P. T., 2003, *MNRAS*, 342, 1056
- van de Ven G., van den Bosch R. C. E., Verolme E. K., de Zeeuw P. T., 2006, *A&A*, 445, 513
- van den Bosch R., de Zeeuw T., Gebhardt K., Noyola E., van de Ven G., 2006, *ApJ*, 641, 852
- van den Bosch R. C. E., van de Ven G., Verolme E. K., Cappellari M., de Zeeuw P. T., 2007, *MNRAS*, submitted [vdB07]
- van der Marel R. P., Cretton N., de Zeeuw P. T., Rix H., 1998, *ApJ*, 493, 613
- van der Marel R. P., de Zeeuw P., Rix H.-W., Quinlan G. D., 1997, *Nature*, 385, 610
- van der Marel R. P., Franx M., 1993, *ApJ*, 407, 525
- Vandervoort P. O., 1984, *ApJ*, 287, 475
- Verolme E. K., de Zeeuw P. T., 2002, *MNRAS*, 331, 959
- Verolme E. K., et al. 2002, *MNRAS*, 335, 517
- Verolme E. K., et al. 2003, in *Galaxies and Chaos*, eds. G. Contopoulos and N. Voglis, LNP vol. 626, p. 279
- Weinacht J., 1924, *Math. Ann.*, 91, 279

APPENDIX A: LIMITING CASES

When two or all three of the constants α , β or γ that define the confocal ellipsoidal coordinate system are equal, the triaxial Abel models reduce to limiting cases with more symmetry and thus with fewer degrees of freedom. The oblate and prolate axisymmetric limits are described in § 6.1. DL91 derived the velocity moments for the non-rotating Abel models for elliptic discs and in the spherical limit. We summarise their results and give the rotating Abel models as well as the expressions for the LOSVD for these limiting cases. At the same time, we also derive the properties of the non-rotating and rotating Abel models in the limit of large radii.

A1 Elliptic disc potential

The two-dimensional analogues of the triaxial Abel models are the elliptic Abel discs with Stäckel potential $V_S(\lambda, \mu) = U[\lambda, \mu]$ in

confocal elliptic coordinates (λ, μ) . The relations with (x, y) follow from those in § 2.1 by setting $z = 0$ or equivalently $\nu = -\gamma$. The two integrals of motion E and I_2 are given by

$$\begin{aligned} E &= \frac{1}{2} (v_x^2 + v_y^2) + U[\lambda, \mu], \\ I_2 &= \frac{1}{2} L_z^2 + \frac{1}{2} (\alpha - \beta) v_x^2 + (\alpha - \beta) x^2 U[\lambda, \mu, -\alpha]. \end{aligned} \quad (\text{A1})$$

A1.1 Velocity moments

Choosing the DF as $f(E, I_2) = f(S)$, with $S = -E + w I_2$, the velocity moments can be evaluated as

$$\begin{aligned} \mu_{lm}(\lambda, \mu) &= \sqrt{\frac{2^{l+m+2}}{h_\mu^{l+1} h_\lambda^{m+1}}} \\ &\times \int_{S_{\min}}^{S_{\max}} T_{lm} [S_{\text{top}}(\lambda, \mu) - S]^{(l+m)/2} f(S) dS, \end{aligned} \quad (\text{A2})$$

with the terms h_μ and h_λ defined as

$$h_\tau = 1 - (\tau + \alpha) w, \quad \tau = \lambda, \mu. \quad (\text{A3})$$

As in the general triaxial case, $S_{\min} \geq S_{\text{lim}}$, where the expression of the latter is given along the w -axis ($u = 0$) in Fig. 1. The accessible part of the (E, I_2) -integral space is now a triangle, the top of which is $S_{\text{top}}(\lambda, \mu) = -U[\lambda, \mu] + w(\lambda + \alpha)(\mu + \alpha)U[\lambda, \mu, -\alpha]$.

For the NR components we have that $S_{\max} = S_{\text{top}}(\lambda, \mu)$ and $T_{lm}^{\text{NR}} = B(\frac{l+1}{2}, \frac{m+1}{2})$. Of the two possible orbit families, the box orbits have no net rotation and the tube orbits rotate around the axis perpendicular to the disc (the z -axis). Since this is similar to the short-axis tube orbits in the general triaxial case, we refer to the rotating type as the SR type. This SR type reaches the region of the accessible integral space (the triangle) for which $v_\mu^2 \geq 0$ at $\mu = -\alpha$ (or $I_2 \geq 0$). Therefore, $S_{\max} = S_{\text{top}}(\lambda, -\alpha)$ and

$$T_{lm}^{\text{SR}} = 2 \int_0^{\arcsin(\sqrt{a_2})} \sin^l \theta \cos^m \theta d\theta, \quad (\text{A4})$$

where a_2 is defined as

$$a_2 = \frac{(\lambda + \alpha) h_\mu [S_{\text{top}}(\lambda, -\alpha) - S]}{(\lambda - \mu) h_{(-\alpha)} [S_{\text{top}}(\lambda, \mu) - S]}. \quad (\text{A5})$$

The integral (A4) can be evaluated in terms of elementary functions (e.g., Gradshteyn & Ryzhik 1994, relations 2.513 on p.160–162). The NR velocity moments $\mu_{lm}^{\text{NR}}(\lambda, \mu)$ vanish when either l or m is odd, and the SR velocity moments $\mu_{lm}^{\text{SR}}(\lambda, \mu)$ vanish when l is odd. The latter should be multiplied with $(-1)^m$ for net rotation in the opposite direction.

The matrix \mathbf{Q} , which transforms the velocity components $(v_\lambda, v_\mu, v_\nu)$ to (v_x, v_y, v_z) , is that for the prolate case given in eq. (6.4), but with $\chi = 0$ substituted. The sign matrix \mathbf{S} , projection matrix \mathbf{P} and rotation matrix \mathbf{R} are the same as for the triaxial case given in respectively eqs (3.3)–(3.5). The polar angle is the inclination, $\vartheta = i$, and the azimuthal angle φ the orientation of the infinitesimally thin disc ($\gamma = 0$) in the plane $z = 0$. In the expression (3.1) for the misalignment angle ψ , the triaxiality parameter thus reduces to $T = 1 - \beta/\alpha$, with $0 < \beta < \alpha$, bracketing the limiting cases of a needle and a circular disc.

A1.2 Line-of-sight velocity distribution

Starting with the expression for the stellar (surface) mass density $\Sigma_*(x', y') = \mu_{00}(\lambda, \mu)$ from eq. (A2), we derive the Abel LOSVD

for the elliptic disc in a similar way as in § 3.3.1 for the triaxial case⁹. The cross section of the unit sphere with a plane, reduces to the cross section of the unit circle $X^2 + Y^2 = 1$ with a line $e_1 X + e_2 Y = v_{z'}/g(S)$. Here, the variable X is defined as

$$X = \frac{h v_\lambda}{g(S) \sqrt{h_\lambda}}, \quad \text{with} \quad g(S) = h \sqrt{\frac{2[S_{\text{top}}(\lambda, \mu) - S]}{h_\lambda h_\mu}}, \quad (\text{A6})$$

and the variable Y follows by interchanging $\lambda \leftrightarrow \mu$. The coefficients of the line are $e_1 = \sqrt{h_\lambda} M_{31}/h$ and $e_2 = \sqrt{h_\mu} M_{32}/h$. We can write the normalisation $h^2 = h_\lambda M_{31}^2 + h_\mu M_{32}^2$, explicitly as

$$h = \sin i \left\{ [1 - (\lambda + \alpha) w] (C \cos \varphi + D \sin \varphi)^2 + [1 - (\mu + \alpha) w] (C \sin \varphi - D \cos \varphi)^2 \right\}^{\frac{1}{2}}, \quad (\text{A7})$$

with C and D defined in eq. (6.5). In this way we can write Σ_* as a double integral over S and $v_{z'}$, so that at a given line-of-sight velocity the LOSVD becomes

$$\begin{aligned} \mathcal{L}(x', y', v_{z'}) &= \frac{1}{h} \int_{S_{\min}}^{S_{\text{up}}(v_{z'})} \frac{f(S)}{\sqrt{2[G(v_{z'}) - S]}} \Delta(v_{z'}, S) dS, \\ &= \frac{\sqrt{2[G(v_{z'}) - S_{\min}]}}{h} \int_0^{\eta_{\text{up}}} f(S) \Delta(v_{z'}, S) \sin \eta d\eta, \quad (\text{A8}) \end{aligned}$$

which vanishes when $|v_{z'}|$ exceeds the 'terminal velocity' $v_t = g(S_{\min})$. The second expression removes the possible singularity at the upper limit of S , given by $S_{\text{up}} = \min[G(v_{z'}), S_{\max}]$, with

$$G(v_{z'}) = S_{\text{top}}(\lambda, \mu) - h_\lambda h_\mu v_{z'}^2 / (2h^2). \quad (\text{A9})$$

Hence, η_{up} is given by $\sin^2 \eta_{\text{up}} = [S_{\text{up}} - S_{\min}] / [G(v_{z'}) - S_{\min}]$. Depending on the integral space accessible by the orbits, the value of $\Delta(v_{z'}, S)$ is either zero, one or two.

For the NR components, $S_{\max} = S_{\text{top}}(\lambda, \mu)$, and, since the full integral space is accessible, $\Delta_{\text{NR}} = 2$, independent of S and $v_{z'}$. In the case of a basis function $f_\delta(S)$ as defined in eq. (2.24), the integral over S can be evaluated explicitly resulting in

$$\mathcal{L}_\delta^{\text{NR}} = \frac{4^{\delta+1} B(\delta+1, \delta+1)}{\sqrt{2}(1 - S_{\min})^\delta} \frac{1}{h} [G(v_{z'}) - S_{\min}]^{\delta+\frac{1}{2}}. \quad (\text{A10})$$

For SR components with maximum streaming, both $v_\mu^2 \geq 0$ at $\mu = -\alpha$ and $v_\mu \geq 0$, which is equivalently to $0 \leq Y \leq \sqrt{a_2}$, where a_2 is defined in eq. (A5). The intersection of the above unit circle and line provides the following two solutions

$$Y_\pm = e_2 [v_{z'}/g(S)] \pm e_1 \sqrt{1 - [v_{z'}/g(S)]^2}. \quad (\text{A11})$$

Given the values of $v_{z'}$ and S , Δ_{SR} is thus equal to 0, 1 or 2 if for respectively none, one or both of the solutions $0 \leq Y_\pm \leq \sqrt{a_2}$.

The expression for h in eq. (A7) shows that the LOSVD in eq. (A8) is inversely proportional to $\sin i$. For face-on viewing at inclination $i = 0^\circ$ the LOSVD reduces to $\Sigma_*(x', y') \delta(v_{z'})$. Because the velocity perpendicular to the disc $v_z = 0$, the face-on LOSVD is zero at all line-of-sight velocities, except at $v_{z'} = 0$ when it equals the surface mass density. For edge-on viewing at inclination $i = 90^\circ$, the LOSVD follows upon substituting $y' = 0$ in eq. (A8) and integrating over the line-of-sight z' . For $i < 90^\circ$, the

latter integration is not needed, since at each position (x', y') on the plane of the sky there is only a single (unique) point along z' where it intersects the infinitesimally thin disc. The edge-on LOSVD and also Σ_* are thus spatially only one-dimensional functions of x' , and vanish for non-zero y' -values.

Further information on elliptic Stäckel discs can be found in Teuben (1987), de Zeeuw, Hunter & Schwarzschild (1987), and Evans & de Zeeuw (1992).

A2 Large distance limit

At large radii, $\lambda \rightarrow r^2 \gg -\alpha$, so that the confocal ellipsoidal coordinates of § 2.1 reduce to conical coordinates (r, μ, ν) , with r the usual distance to the origin, i.e., $r^2 = x^2 + y^2 + z^2$, and μ and ν angular coordinates on the sphere. In these coordinates the Stäckel potential is of the form $V_S(r, \mu, \nu) = V(r) + U[\mu, \nu]/r^2$, where $V(r)$ is an arbitrary smooth function of r . The corresponding integrals of motion are given by

$$\begin{aligned} E &= \frac{1}{2} (v_x^2 + v_y^2 + v_z^2) + V_S(r, \mu, \nu), \\ I_2 &= \frac{1}{2} T L_y^2 + \frac{1}{2} L_z^2 + (\alpha - \beta) \frac{x^2}{r^2} U[\mu, \nu, -\alpha], \\ I_3 &= \frac{1}{2} L_x^2 + \frac{1}{2} (1 - T) L_y^2 + (\gamma - \beta) \frac{z^2}{r^2} U[\mu, \nu, -\gamma]. \end{aligned} \quad (\text{A12})$$

With the choice (2.9) for the DF, the expression for the velocity moments becomes

$$\begin{aligned} \mu_{lmn}(r, \mu, \nu) &= \frac{1}{r^{m+n+2}} \sqrt{\frac{2^{l+m+n+3}}{F_\nu^{m+1} F_\mu^{n+1}}} \\ &\times \int_{S_{\min}}^{S_{\max}} T_{lmn} [S_{\text{top}}(r, \mu, \nu) - S]^{(l+m+n+1)/2} f(S) dS, \quad (\text{A13}) \end{aligned}$$

where F_ν and F_μ are defined as

$$F_\tau = \frac{1}{r^2} + \frac{(\tau + \alpha) w - (\tau + \gamma) u}{\gamma - \alpha}, \quad \tau = \mu, \nu. \quad (\text{A14})$$

As in the general triaxial case, $S_{\min} \geq S_{\text{lim}}$, where S_{lim} can be obtained from Fig. 1. The expressions of S_{\max} and T_{lmn} for the NR, LR and SR types are those given in §§ 2.3.2–2.3.4 respectively, but with $S_{\text{top}}(\lambda, \mu, \nu)$ (eq. 2.14) replaced by

$$\begin{aligned} S_{\text{top}}(r, \mu, \nu) &= -V_S(r, \mu, \nu) \\ &- w \frac{(\mu + \alpha)(\nu + \alpha)}{\gamma - \alpha} U[\mu, \nu, -\alpha] \\ &- u \frac{(\mu + \gamma)(\nu + \gamma)}{\alpha - \gamma} U[\mu, \nu, -\gamma], \end{aligned} \quad (\text{A15})$$

and the parameters a_0 and b_0 (2.17) reduce to

$$\begin{aligned} a_0 &= \frac{S_{\text{top}}(r, \mu, -\beta) - S}{S_{\text{top}}(r, \mu, \nu) - S}, \\ b_0 &= \frac{(\mu + \beta) F_\nu [S_{\text{top}}(r, \mu, -\beta) - S]}{(\mu - \nu) F_{(-\beta)} [S_{\text{top}}(r, \mu, \nu) - S]}, \end{aligned} \quad (\text{A16})$$

which by interchanging $\nu \leftrightarrow \mu$ become a_1 and b_1 , and in turn a_2 and b_2 follow by $\beta \leftrightarrow \alpha$.

In the conversion to observables described in § 3, in the matrix \mathbf{Q} , which transforms the velocity components (v_r, v_μ, v_ν) to (v_x, v_y, v_z) , all terms $\lambda + \sigma$ ($\sigma = -\alpha, -\beta, -\gamma, \mu, \nu$) cancel out (cf. eq. 25 of Statler 1994). The expression for the LOSVD follows from that of the triaxial case in eq. (3.27) by substituting $H_{\mu\nu} = 1$, $H_{\nu\lambda} = r^2 F_\nu$, $F_{\lambda\mu} = r^2 F_\mu$ and $S_{\text{top}}(\lambda, \mu, \nu) = S_{\text{top}}(r, \mu, \nu)$. Suppose now that at large radii r , the function $V(r)$ in the

⁹ Alternatively, one can invert the relations $S = S_{\text{top}}(\lambda, \mu) - \frac{1}{2}(h_\mu v_\lambda^2 + h_\lambda v_\mu^2)$ and $v_{z'} = M_{31} v_\lambda + M_{32} v_\mu$ to find the Jacobian to transform from the coordinates (v_λ, v_μ) to $(S, v_{z'})$. Leaving out the integral over $v_{z'}$, yields the same expression for the LOSVD as in eq. (A8).

Stäckel potential vanishes and we keep in the above expressions only the dominant terms. In this case, F_μ , F_ν and S_{top} reduce to functions of μ and ν only. As a result, the velocity moments (A13) are independent of r , except for the prefactor $1/r^{m+n+2}$, and therefore are scale-free. Once we have calculated the velocity moments at a radius r , those at radius $r' = qr$, with q a constant, follow by a simple scaling, $\mu_{lmn}(r', \mu, \nu) = \mu_{lmn}(r, \mu, \nu)/q^{m+n+2}$. The same holds true for the line-of-sight velocity moments $\mu_k(r, \mu, \nu)$, but not for the LOSVD.

A3 Spherical potential

When $\alpha = \beta = \gamma$, both μ and ν lose their meaning and we replace them by the customary polar angle θ and azimuthal angle ϕ . The expressions for the Abel models in these spherical coordinates (r, θ, ϕ) follow in a straightforward way from those in § A2 for the large distance limit in conical coordinates (r, μ, ν) .

The Stäckel potential $V_S = V(r)$ is spherically symmetric. The expressions for the integrals of motion follow from (A12), where for I_2 and I_3 the right-most terms vanish. The triaxiality parameter T is now a free parameter, so that, together with the parameters w and u , we can rewrite $S = -E + w I_2 + u I_3$ as

$$S = -E + \frac{1}{2}uL_x^2 + \frac{1}{2}[(1-T)u + Tw]L_y^2 + \frac{1}{2}wL_z^2. \quad (\text{A17})$$

This means that with the choice (2.9) for the DF, we cover the most general homogeneous quadratic form in the velocities that is allowed by the integrals of motion in a spherical symmetric potential, i.e., the energy E and all three components of the angular momentum vector \mathbf{L} (cf. DL91). These include the models considered by Osipkov (1979) and Merritt (1985) with the DF of the form $f(-E \pm L^2/r_a^2)$ and those studied by Arnold (1990) with a more general DF of the form $f(-E \pm L^2/r_a^2 \pm L_z^2/r_b^2)$. These models follow by setting $u = w = \pm 2/r_a^2$, and by taking $u = \pm 2/r_a^2$, $w = u \pm 2/r_b^2$ and $T = 0$, respectively.

A3.1 Velocity moments

The velocity moments follow from eq. (A13), with

$$F_\tau = \frac{1}{r^2} - \frac{1}{2}(w + u) + \frac{1}{2}(w - u) \left[\cos^2 \theta + T (\sin^2 \theta \sin^2 \phi - 1) \pm \sqrt{\Lambda} \right], \quad (\text{A18})$$

where the positive and negative sign are for F_μ and F_ν , and

$$\Lambda = [\sin^2 \theta + T (\sin^2 \theta \sin^2 \phi - 1)]^2 + 4T \sin^2 \theta \cos^2 \theta \sin^2 \phi. \quad (\text{A19})$$

Taking $\alpha = \beta = \gamma$ in Fig. 1, we see that the boundaries on w and u both vanish. The separatrices L_1 and L_2 , defined in eq. (2.13), reduce to the negative w -axis and the line $w = u$, respectively. Furthermore, $S_{\text{max}} = S_{\text{top}} = -V(r)$, and for T_{lmn} we use the expression (2.15). The resulting velocity moments $\mu_{lmn}(r, \theta, \phi)$, which are in general *not* spherically symmetric, vanish when either l , m or n is odd.

The latter implies no net rotation, which is the case when the (conserved) angular momentum vectors \mathbf{L} for the orbits are randomly oriented. We may introduce net rotation by assuming that (a fraction of) the orbits have a preferred sense of rotation around an angular momentum vector \mathbf{L}_0 that points in a specific direction given by θ_0 and ϕ_0 . Using the projection matrix P in

eq. (3.4) with $\vartheta = \theta_0$ and $\varphi = \phi_0$, we transform to the coordinate system $(r' = r, \theta', \phi')$, in which \mathbf{L}_0 is aligned with the z' -axis. If we next set the DF to zero for $L_{z'} < 0$, we find $\mu'_{lmn}(r, \theta', \phi') = \frac{1}{2}\mu_{lmn}(r, \theta', \phi')$, which does still vanish when l or m is odd, but is non-zero when n is odd, resulting in maximum streaming around the z' -axis, and multiplication with $(-1)^n$ for opposite direction of rotation. With the inverse of the projection matrix, we can then transform these velocity moments to the original coordinates system (r, θ, ϕ) . In this way, we can build spherical Abel models, which in addition to a non-rotating part consist of a component or several components with a preferred rotation axis. Mathieu, Dejonghe & Hui (1996) used this approach to construct a dynamical model of Centaurus A, with a spherical potential, but triaxial luminosity density and DF components with rotation around the apparent long and short axis.

From the customary definition of the spherical coordinate system, $x = r \sin \theta \cos \phi$, $y = r \sin \theta \sin \phi$ and $z = r \cos \theta$, it follows directly that the matrix \mathbf{Q} , which transforms the velocity components (v_r, v_θ, v_ϕ) to (v_x, v_y, v_z) , is given by

$$\mathbf{Q} = \begin{pmatrix} \sin \theta \cos \phi & \cos \theta \cos \phi & -\sin \phi \\ \sin \theta \sin \phi & \cos \theta \sin \phi & \cos \phi \\ \cos \theta & -\sin \theta & 0 \end{pmatrix}. \quad (\text{A20})$$

In case the orbits have no preferred sense of rotation, we may set the viewing angles $\vartheta = \varphi = 0$ without loss of generality, so that with $\psi = 0$ from eq. (3.1), $(x', y') = (y, -x)$ on the plane of the sky and $z' = z$ along the line-of-sight, and similarly for the Cartesian velocity components.

A3.2 Line-of-sight velocity distribution

There is no obvious further simplification of the LOSVD for rotating components. For the NR components, the LOSVD follows from eq. (3.27) with $S_{\text{max}} = S_{\text{top}} = -V(r)$ and $\Delta\xi' = 2\pi$, or from eq. (3.28) after substituting the basis function $f_\delta(S)$ from eq. (2.24). Since the line-of-sight velocity $v_{z'} = \text{sgn}(z)[\cos \theta v_r - \sin \theta v_\theta]$, it follows that $M_{31}^2 = \cos^2 \theta$, $M_{32} = \sin^2 \theta$ and $M_{33}^2 = 0$ in eq. (3.19) for h . Moreover, $H_{\mu\nu} = 1$ and $H_{\tau\lambda} = r^2 F_\tau$ ($\tau = \mu, \nu$), with F_τ given in eq. (A18).

Carollo et al. (1995) compute the LOSVD for Osipkov-Merritt models with $f(-E - L^2/(2r_a^2))$, which is a special case of the Abel DF $f(S)$, that follows from eq. (A17) by setting $u = w = -1/r_a^2$. Substituting the latter in eq. (A18), we find that $H_{\lambda\mu} = H_{\lambda\nu} = (r_a^2 + r^2)/r_a^2$, so that

$$h^2 = (r_a^2 + r^2)(r_a^2 + r^2 - R'^2)/r_a^4, \quad (\text{A21})$$

$$G(v_{z'}) = -V(r) - \frac{r_a^2 + r^2}{r_a^2 + r^2 - R'^2} \frac{v_{z'}^2}{2}, \quad (\text{A22})$$

with radius $R' = r \sin \theta$ on the plane of the sky. After substitution in eq. (3.27), and transforming the integral over dz' to dr , we find the following LOSVD

$$\mathcal{L}(R', v_{z'}) = 4\pi \int_{R'}^{\infty} \frac{r}{h\sqrt{r^2 - R'^2}} \int_{S_{\text{min}}}^{G(v_{z'})} f(S) dS dr. \quad (\text{A23})$$

This is the same as the (unnormalised) velocity profile in eq. (27) of Carollo et al. (1995), with Φ_∞ , the lower limit of their (relative) potential $\Phi(r) = -V(r)$, equal to S_{min} , which from Fig. 1 in this case has $S_{\text{lim}} = 0$ as lower limit. Their function $g(r, R')$ and upper limit Q_{max} in eqs (25) and (26), are equivalent to respectively the

Table B1. The function \mathcal{M} for odd s .

| $s \ i \ j$ | $\mathcal{M}(s, i, j; a, b, \phi)$ |
|-------------|--|
| 100 | ϕ |
| 300 | $\frac{1}{2}(4 - a - b)\phi + \frac{1}{4}(b - a)\sin 2\phi$ |
| 310 | $-\frac{1}{2}\phi - \frac{1}{4}\sin 2\phi$ |
| 301 | $-\frac{1}{2}\phi + \frac{1}{4}\sin 2\phi$ |
| 500 | $\frac{1}{8}(24 - 12a - 12b + 3a^2 + 3b^2 + 2ab)\phi$ $+ \frac{1}{4}(b - a)(3 - a - b)\sin 2\phi + \frac{1}{32}(b - a)^2\sin 4\phi$ |
| 510 | $-\frac{1}{4}(6 - 3a - b)\phi - \frac{1}{4}(3 - 2a)\sin 2\phi - \frac{1}{16}(b - a)\sin 4\phi$ |
| 501 | $-\frac{1}{4}(6 - 3b - a)\phi + \frac{1}{4}(3 - 2b)\sin 2\phi + \frac{1}{16}(b - a)\sin 4\phi$ |
| 520 | $\frac{3}{4}\phi + \frac{1}{2}\sin 2\phi + \frac{1}{16}\sin 4\phi$ |
| 511 | $\frac{1}{4}\phi - \frac{1}{16}\sin 4\phi$ |
| 502 | $\frac{3}{4}\phi - \frac{1}{2}\sin 2\phi + \frac{1}{16}\sin 4\phi$ |

inverse of h and $G(v_{z'})$ in eqs (A21) and (A22) above. The well-known isotropic case follows upon taken the limit $r_a \rightarrow \infty$, so that $f(S) \rightarrow f(-E)$, $h \rightarrow 1$ and $G(v_{z'}) \rightarrow -V(r) - v_{z'}^2/2$.

APPENDIX B: THE FUNCTION \mathcal{M}

The function \mathcal{M} that appears in the velocity moments of the rotating Abel components is defined as

$$\mathcal{M}(s, i, j; a, b, \phi) = \int_0^\phi \left(\frac{\partial}{\partial a} \right)^i \left(\frac{\partial}{\partial b} \right)^j \frac{1 - \sqrt{[1 - p(\theta)]^{s+1}}}{p(\theta)} d\theta, \quad (\text{B1})$$

with $p(\theta) \equiv a \cos^2 \theta + b \sin^2 \theta$. For odd s , corresponding to odd velocity moments, the integral can be evaluated in a straightforward way in terms of elementary functions. In Table B1, we give the resulting expressions for $s = 1, 3, 5$.

For even s , the integral can be evaluated in terms of the (incomplete) elliptic integrals. To simplify the numerical evaluation we use Carlson's (1977) symmetrical forms R_F , R_D and R_J (for the relations between both forms see e.g. de Zeeuw & Pfenniger 1988). In Table B2, we give the expressions for $s = 0, 2, 4$, where we have introduced the following quantities based on these symmetric elliptic integrals

$$\begin{aligned} F &= \frac{\sqrt{1-a} \sin \phi}{a} R_F(\cos^2 \phi, \Delta^2, 1), \\ D &= \frac{\sin^3 \phi}{3\sqrt{1-a}} R_D(\cos^2 \phi, \Delta^2, 1), \\ J &= \frac{(b-a)\sin^3 \phi}{3a^2\sqrt{1-a}} R_J(\cos^2 \phi, \Delta^2, 1, \frac{p(\phi)}{a}), \end{aligned} \quad (\text{B2})$$

with $\Delta^2 = [1 - p(\phi)]/(1 - a)$, and we have defined the terms

$$\begin{aligned} A &= \frac{1}{\sqrt{ab}} \arctan \left(\sqrt{\frac{b}{a}} \tan \phi \right), \\ P &= \sin \phi \cos \phi \sqrt{1 - p(\phi)}, \\ Q &= \sin \phi \cos \phi \frac{1 - \sqrt{1 - p(\phi)}}{p(\phi)}. \end{aligned} \quad (\text{B3})$$

In Fig. B1, we show the $\mathcal{M}(s, i, j; a, b, \phi)$ as function of ϕ for the case that $a = 0.1$ and $b = 0.5$, up to order $s = 5$.

We now consider some special cases. When either a or b is zero, the corresponding velocity moments vanish (eqs 2.16 and

2.19), and when $a_i > b_i$ the arguments of the function \mathcal{M} are interchanged (eqs 2.18, 2.20 and 2.21). This means we only have to consider the range $0 < a \leq b$, together with $0 < \phi \leq \pi/2$, since \mathcal{M} vanishes when $\phi = 0$.

When $a = b$, it follows that $p(\theta) = a$ in eq. (B1), so we can separate $\mathcal{M}(s, i, j; a, a, \phi) = \mathcal{M}_1(s, i, j; a) \mathcal{M}_2(i, j; \phi)$, where

$$\mathcal{M}_1(s, i, j; a) = \frac{d^{i+j}}{da^{i+j}} \frac{1 - \sqrt{(1-a)^{s+1}}}{a} \quad (\text{B4})$$

$$\mathcal{M}_2(i, j; \phi) = \int_0^\phi \cos^{2i} \theta \sin^{2j} \theta \int_0^\phi \cos^{2i} \theta \sin^{2j} \theta d\theta.$$

For $a = 1$, the expression for \mathcal{M}_1 simplifies to $(-1)^{i+j}(i+j)!$. The integral in the expression for \mathcal{M}_2 can be evaluated explicitly using e.g. the relations 2.513 of Gradshteyn & Ryzhik (1994). For $\phi = \pi/2$, it reduces to the beta function $B(i + 1/2, j + 1/2)$.

When $a < b = 1$, the elliptic integrals become elementary, so that the quantities F , D and J in eq. (B2) reduce to

$$\begin{aligned} F &= \frac{\sqrt{1-a}}{a} \ln \left[\tan \left(\frac{\pi}{4} + \frac{\phi}{2} \right) \right], \\ D &= \frac{a}{1-a} F - \frac{\sin \phi}{\sqrt{1-a}}, \\ J &= F - \frac{1}{\sqrt{a}} \arctan \left(\sqrt{\frac{1-a}{a}} \sin \phi \right). \end{aligned} \quad (\text{B5})$$

Although F diverges when $\phi \rightarrow \pi/2$, substitution of these reduced quantities in the expressions of \mathcal{M} for even s (Table B2), shows that all terms with F cancel. For $\phi = \pi/2$, the function \mathcal{M} is thus everywhere finite, with $A = \pi/(2\sqrt{ab})$ and $P = Q = 0$.

APPENDIX C: EDGEWORTH EXPANSION

For the (re)construction of the LOSVD from its true line-of-sight velocity moments, one can use the well-known Gram-Charlier series, the terms of which are simple functions of the true moments (see e.g. Appendix B2 of van der Marel & Franx 1993), but it has poor convergence properties. The terms in the Edgeworth (1905) expansion are also directly related to the true moments, but since it is a true asymptotic expansion its accuracy is controlled, so that, unlike the Gauss-Hermite and Gram-Charlier expansions, convergence plays no role (see Blinnikov & Moessner 1998 for a comparison between the expansions and for further references).

The Edgeworth expansion of the LOSVD up to order N is given by

$$\mathcal{L}_N^{\text{ED}}(v) = \Sigma \frac{e^{-\frac{1}{2}w^2}}{\sqrt{2\pi}\sigma} \left[1 + \sum_{n=3}^N D_n \right], \quad (\text{C1})$$

with $w = (v - V)/\sigma$ and

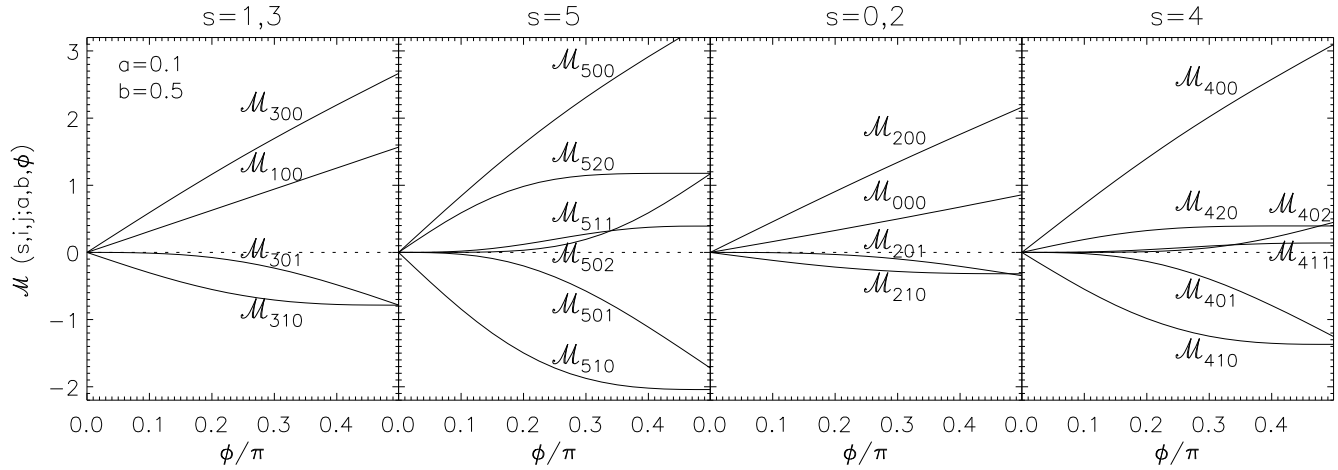
$$D_n = \sum_{\{l_{i-2}\}} \mathcal{H}_{n+2(l-1)}(w) \prod_{i=3}^n \frac{1}{l_{i-2}!} \left(\frac{d_i}{i!} \right)^{l_{i-2}}. \quad (\text{C2})$$

The Hermite polynomials \mathcal{H}_m are related to those defined by van der Marel & Franx (1993) as $\mathcal{H}_m(w) = \sqrt{m!} H_m(w/\sqrt{2})$. We have defined $l = \sum_{j=1}^{n-2} l_j$, where the sets $\{l_j\}$ are the non-negative integer solutions of the Diophantine equation

$$l_j + 2l_j + \dots + (n-2)l_{n-2} = n-2, \quad n \geq 3, \quad (\text{C3})$$

Table B2. The function \mathcal{M} for even s .

| $s\ i\ j$ | $\mathcal{M}(s, i, j; a, b, \phi)$ |
|-----------|---|
| 000 | $A - F + J$ |
| 200 | $A - (1 - a)F - (b - a)D + J$ |
| 210 | $-\frac{1}{2a}[A + Q - (1 + a)F + (1 - a)D + J]$ |
| 201 | $-\frac{1}{2b}[A - Q - F - (1 - b)D + J]$ |
| 400 | $A + \frac{1}{3}(b - a)P - \frac{1}{3}(2a^2 + ab - 6a + 3)F + \frac{1}{3}(2a + 2b - 7)(b - a)D + J$ |
| 410 | $-\frac{1}{2a}[A + aP + Q - (1 + 2a)(1 - a)F + (2a^2 - 2a - ab + 1)D + J]$ |
| 401 | $-\frac{1}{2b}[A - bP - Q - (1 - ab)F - (2b^2 - 2b - ab + 1)D + J]$ |
| 420 | $\frac{3}{4a^2}\left\{A + \frac{a^2 p(\phi) - ab}{3(b-a)p(\phi)}P + \frac{5a \cos^2 \phi + 3b \sin^2 \phi}{3p(\phi)}Q + \frac{2a^3 - 3a^2 b + 4a^2 + 3a - 3ab - 3b}{3(b-a)}F - \frac{(2a^2 + 5a - 4ab - 3b)(1-a)}{3(b-a)}D + J\right\}$ |
| 411 | $\frac{1}{4ab}\left\{A + \frac{ab - ab p(\phi)}{(b-a)p(\phi)}P + \frac{b \sin^2 \phi - a \cos^2 \phi}{p(\phi)}Q + \frac{a^2 b - ab + a - b}{b-a}F + \frac{a^2 b + ab^2 - 4ab + a + b}{b-a}D + J\right\}$ |
| 402 | $\frac{3}{4b^2}\left\{A + \frac{b^2 p(\phi) - ab}{3(b-a)p(\phi)}P - \frac{3a \cos^2 \phi + 5b \sin^2 \phi}{3p(\phi)}Q - \frac{3b - 3a - ab + ab^2}{3(b-a)}F - \frac{(2b^2 + 5b - 4ab - 3a)(1-b)}{3(b-a)}D + J\right\}$ |

**Figure B1.** The function $\mathcal{M}(s, i, j; a, b, \phi)$ defined in eq. (B1) plotted against ϕ , for $a = 0.1$ and $b = 0.5$, up to order $s = 5$. The curves in the left two panels are for odd values of s corresponding to the odd velocity moments, whereas the curves in the right two panels are for even values of s . The indices of the labels \mathcal{M}_{sij} refer to the first three parameters of the function \mathcal{M} .

Substituting these solutions, we find up to order $N = 5$

$$\begin{aligned} \mathcal{L}_5^{\text{ED}}(v) = \Sigma \frac{e^{-\frac{1}{2}w^2}}{\sqrt{2\pi}\sigma} & \left[1 + \mathcal{H}_3(w) \frac{d_3}{3!} + \mathcal{H}_4(w) \frac{d_4}{4!} \right. \\ & + \mathcal{H}_6(w) \frac{1}{2} \left(\frac{d_3}{3!} \right)^2 + \mathcal{H}_5(w) \frac{d_5}{5!} \\ & \left. + \mathcal{H}_7(w) \frac{d_3}{3!} \frac{d_4}{4!} + \mathcal{H}_9(w) \frac{1}{6} \left(\frac{d_3}{3!} \right)^3 \right]. \end{aligned} \quad (\text{C4})$$

The lower-order moments Σ , V and σ are equivalent to those in eq. (3.41), while the higher-order moments d_i ($i \geq 3$) are cumulants of the true moments

$$d_i = \frac{i!}{\sigma^n} \sum_{\{l_k\}} (-1)^{l-1} (l-1)! \prod_{k=1}^i \frac{1}{l_k!} \left(\frac{\mu_k}{k!} \right)^{l_k}, \quad (\text{C5})$$

so that

$$d_3 = \xi_1, \quad d_4 = \xi_2 - 3, \quad \text{and} \quad d_5 = \xi_3 - 10\xi_1. \quad (\text{C6})$$

The central moments ξ_1 (skewness), ξ_2 (kurtosis) and ξ_3 are related

to the true moments respectively as

$$(\mu_0 \sigma)^3 \xi_1 = \mu_0^2 \mu_3 - 3 \mu_0 \mu_1 \mu_2 + 2 \mu_1^3, \quad (\text{C7})$$

$$(\mu_0 \sigma)^4 \xi_2 = \mu_0^3 \mu_4 - 4 \mu_0^2 \mu_1 \mu_3 + 6 \mu_0 \mu_1^2 \mu_2 - 3 \mu_1^4, \quad (\text{C8})$$

$$\begin{aligned} (\mu_0 \sigma)^5 \xi_3 = & \mu_0^4 \mu_5 - 5 \mu_0^3 \mu_1 \mu_4 + 10 \mu_0^2 \mu_1^2 \mu_3 \\ & - 10 \mu_0 \mu_1^3 \mu_2 + 4 \mu_1^5. \end{aligned} \quad (\text{C9})$$

Substituting the line-of-sight true moments μ_k for $k = 0, \dots, K$, we can compute $\mathcal{L}_K^{\text{ED}}(v)$ at each position on the plane of the sky.

In Fig. C1, we show an example of a LOSVD (black solid line) computed directly via eq. (3.27) for the triaxial Abel model constructed in § 4.3. The Edgeworth LOSVD (red solid line) is constructed from the true line-of-sight velocity moments, based on the intrinsic velocity moments computed via eq. (2.10). The Edgeworth reconstruction approximates (very) well the directly-computed LOSVD, as well as the corresponding best-fit Gauss-Hermite series (blue dashed line). In Fig. C2, we show the Gauss-Hermite moments after fitting at each (aperture) position on the sky-plane the directly-computed LOSVD (top panels) as well as the reconstructed Edgeworth LOSVD (bottom panels). The resulting maps are very similar, except for a suppression of the higher-order Gauss-Hermite moments in case of the Edgeworth reconstruction. This is expected, since intrinsic velocity moments of order higher

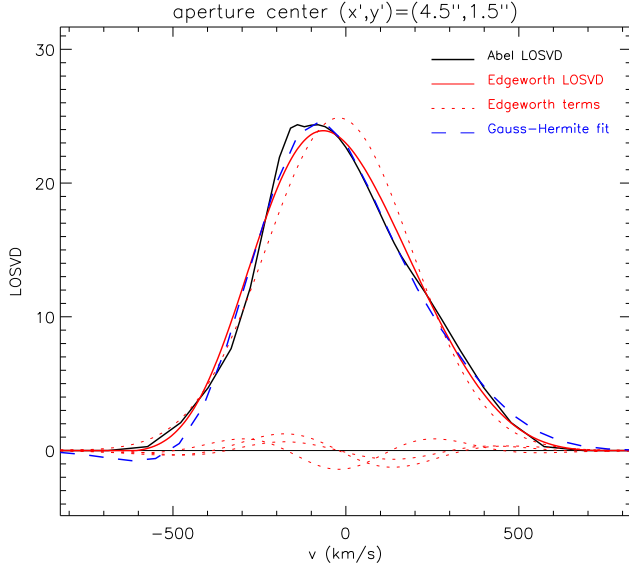


Figure C1. Line-of-sight velocity distribution (LOSVD) of the triaxial Abel model presented in § 4.3, at the (aperture) position on the sky-plane given at the top of the figure. The black solid curve is the LOSVD computed directly via eq. (3.27). The red solid curve show the Edgeworth LOSVD constructed from the true line-of-sight velocity moments, based on the intrinsic velocity moments computed via eq. (2.10). The Gaussian and the higher order terms of the Edgeworth expansion (C1) are shown by the red dotted curves. The blue dashed curve shows the best-fit Gauss-Hermite LOSVD.

than $N = 5$ are needed to accurately determine the wings of the LOSVD. Nevertheless, this comparison is important to show the correctness of both (independent) approaches, and that the Edgeworth expansion provides a reliable and efficient way to reconstruct the LOSVD (and obtain Gauss-Hermite moments) from true moments that are in general (numerically) easier to compute than the full LOSVD.

This paper has been typeset from a $\text{\TeX}/\text{\LaTeX}$ file prepared by the author.

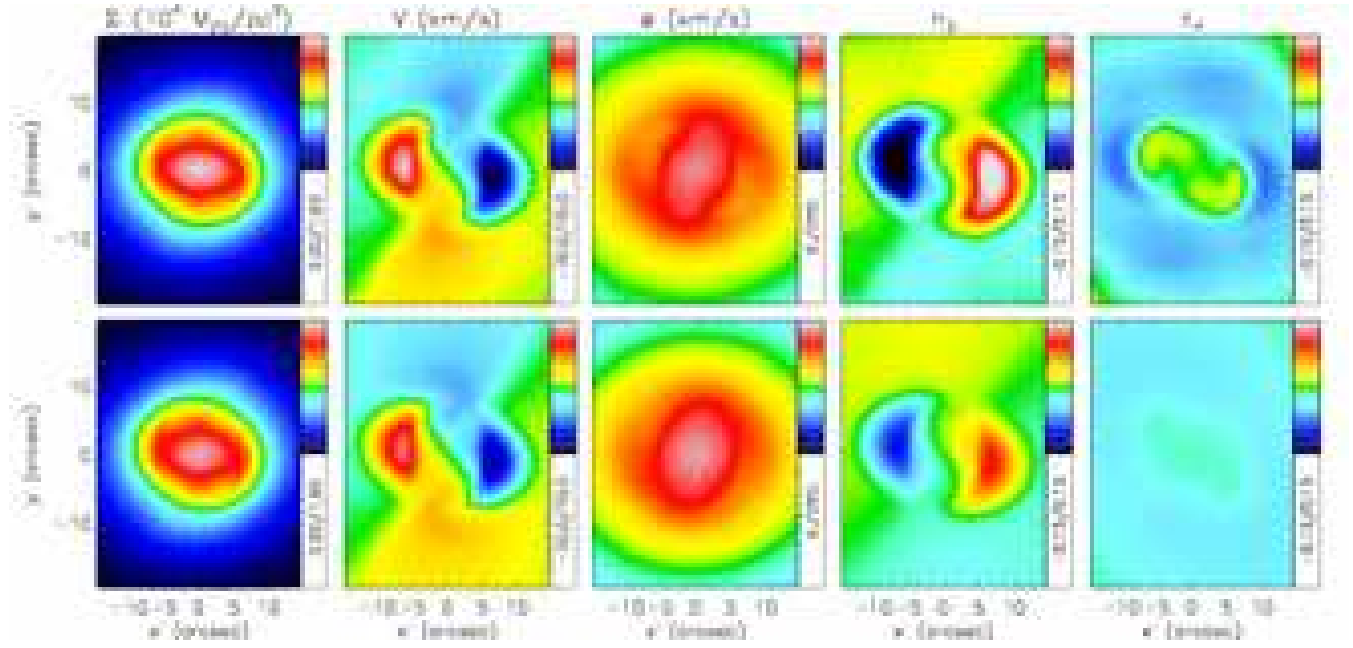


Figure C2. Maps of the surface mass density (Σ ; in $10^4 \text{ M}_\odot \text{ pc}^{-2}$), mean line-of-sight velocity V and dispersion σ (both in km s^{-1}), and higher order Gauss-Hermite moments h_3 and h_4 , of the triaxial Abel model constructed in § 4.3. The top panels follow from fitting, at each (aperture) position on the sky-plane, Gauss-Hermite series to the LOSVD computed directly via eq. (3.27). For the bottom panels the fit is applied to the Edgeworth LOSVD constructed from the true line-of-sight velocity moments, based on the intrinsic velocity moments computed via eq. (2.10).